

ELECTRICAL CONDUCTIVITY IN THE
FeO·Fe₂O₃-Al₂O₃-SiO₂ SYSTEM.

by

CHUNG-AN FELIX YEN

S.B., Massachusetts Institute of Technology
1974

S.M., Massachusetts Institute of Technology
1974

Submitted in partial fulfillment of the requirements
for the degree of
DOCTOR OF PHILOSOPHY
at the

Massachusetts Institute of Technology

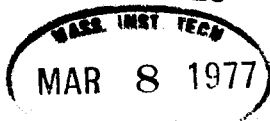
February, 1977

C. A. Yen
Signature of Author.....
Department of Materials Science and
Engineering
January 13, 1977
C. A. Yen

Certified by.....
Thesis Supervisor
[Signature]

Accepted by.....
Chairman, Departmental Committee on
Graduate Students

ARCHIVES



ABSTRACT

ELECTRICAL CONDUCTIVITY IN THE

$\text{FeO}\cdot\text{Fe}_2\text{O}_3\text{-Al}_2\text{O}_3\text{-SiO}_2$ SYSTEM

by

CHUNG-AN FELIX YEN

Submitted to the Department of Materials Science and Engineering on January 13, 1977, in partial fulfillment of the requirements for the degree of Doctor of Philosophy.

The electrical conductivity of the $\text{FeO}\cdot\text{Fe}_2\text{O}_3\text{-Al}_2\text{O}_3\text{-SiO}_2$ system has been studied in the temperature range of 1000° to 1600°C and oxygen partial pressure of $10^{-9} < P_{\text{O}_2} < 10^0$ atm and as a function of composition.

The compositions studied are of 7 or 17 w/o SiO_2 with varying Fe_3O_4 and Al_2O_3 contents. The dc-data and the ac-conductivity up to 10 KHz for compositions with more than 33 w/o Fe_3O_4 are essentially equal, suggesting that the electrical conduction is predominantly electronic.

Several types of conductivity-temperature dependence are observed in air and are directly correlated with the phase chemistry of the system, particularly the crystallization sequences. The compositions studied crystallize to form multiphase composites of spinel, corundum, mullite and/or iron aluminosilicate glasses. The electrical conductivity in the crystallized composites must therefore be interpreted with a multiphase conduction model.

In the first type of conductivity-temperature behavior in air, the electrical conductivity increases with decreasing temperature with no distinct discontinuity upon solidification. The dependence of electrical conduction on temperature is of three stages in all other cases. A sharp discontinuity is observed upon solidification. The activation energies for conduction in these crystallized composites of spinel, mullite and corundum vary from 0.39 to 2.97eV, depending as to whether iron-mullite or corundum is the matrix.

The electrical conductivity of iron aluminosilicate melts at 1550° and 1600°C are also measured as a function of oxygen partial pressure and are found to depend on the total iron concentration and the $\text{Fe}^{3+}/\text{Fe}_{\text{total}}$ ratio. The conductivity decreases with increasing P_{O_2} at $P_{\text{O}_2} > 10^{-1}$ atm. Over a wide intermediate range of P_{O_2} ($10^{-5} < P_{\text{O}_2} < 10^{-1}$ atm), the conductivity remains practically constant. Upon subsequent reduction at still lower P_{O_2} , the electrical conductivity decreases. The electrical conductivity of all the iron aluminosilicate melts studied is of the order of $0.1\text{-}0.2 \text{ ohm}^{-1}\cdot\text{cm}^{-1}$ over the whole oxygen partial pressure range.

The results are analyzed according to the conduction band

model and a thermally activated mechanism. Using the latter model, the fraction of Fe^{3+} ions in octahedral coordination can be calculated.

Thesis supervisor: H. Kent Bowen
Professor of Ceramics

TABLE OF CONTENTS

	Page
Abstract.....	2
Table of Contents.....	4
List of Figures.....	7
List of Tables.....	12
Acknowledgements.....	13
I. Introduction.....	14
II. Theory and Literature Review.....	17
II.1. Theory.....	18
II.1.1. Conduction Models.....	18
II.1.2. Electrical Conductivity in Composite Systems.....	23
II.2. The $\text{FeO}\cdot\text{Fe}_2\text{O}_3\text{-Al}_2\text{O}_3\text{-SiO}_2$ System.....	26
II.2.1. Iron Aluminum Spinel.....	31
II.2.2. Corundum.....	32
II.2.3. Mullite.....	37
II.3. Electrical Conductivity of Glasses and Silicate Melts.....	38
II.3.1. Semiconducting Oxide Glasses Containing Transitional Metal Ions (TMI).....	38
II.3.2. Iron and Vanadium Phosphate Glasses.....	41
II.3.3. Silicate Melts.....	45
III. Ionic Activities in Silicate Melts - A Thermodynamic Approach to the $\text{FeO}\cdot\text{Fe}_2\text{O}_3\text{-Al}_2\text{O}_3\text{-SiO}_2$ System.....	54
III.1. Thermodynamic Activities in the $\text{FeO}\cdot\text{Fe}_2\text{O}_3\text{-}$ $\text{Al}_2\text{O}_3\text{-SiO}_2$ System.....	56

	Page
III.2. Justification for using an Alumina Crucible as the Conductivity Cell.....	71
IV. Research Objectives.....	75
V. Experimental Procedures.....	76
V.1.1. Sample Preparation.....	76
V.1.2. Conductivity Cell: Design and Calibration..	78
V.2.1. Electrical Conductivity Measurement.....	84
V.2.2. Oxygen Partial Pressure Control.....	87
V.2.3. Experimental Error.....	88
V.2.4. Identification and Characterization of Phases.....	89
VI. Experimental Results.....	92
VI.1. Introduction.....	92
VI.2. Conductivities in Air as a Function of Temperature.....	94
VI.2.1. Compositions with a Final Crystallization Product of Spinel Grains in an Inter- Connecting Glassy Matrix.....	94
VI.2.2. Compositions with Mullite as the Matrix Phase of the Multiphase Crystallization Product.....	106
VI.2.3. Conduction via a Corundum Matrix in the Crystalline Composite.....	118
VI.2.4. Electrical Conductivity of Iron Alumino- Silicate Melts.....	125
VI.3. Isothermal Electrical Conductivity of Iron Aluminosilicate Melts as a Function of Oxygen Partial Pressure.....	130

	Page
VII. Discussion.....	136
VIII. Conclusions.....	161
IX. Suggestions for Future Work.....	164
Appendix: Equivalent Circuit for Ionic and Electronic Conductivity.....	165
References.....	167
Biographical Note.....	176

LIST OF FIGURES

	Page
Figure 1. The distribution of Fe^{3+} ions among octahedral and tetrahedral coordinations in the Fe_2O_3 - CaO - Al_2O_3 - SiO_2 system as a function of composition.....	24
Figure 2. The FeO - Fe_2O_3 - Al_2O_3 - SiO_2 system with the 0.21 atmosphere oxygen isobaric liquidus surface included.....	28
Figure 3. Projection of the 0.21 atmosphere oxygen isobaric liquidus surface onto the $FeO \cdot Fe_2O_3$ - Al_2O_3 - SiO_2 plane. (After Muan, ref.25).....	29
Figure 4. Electrical conductivities of iron aluminum spinels and magnetite. (After T.O.Mason)	33
Figure 5. Electrical conductivities of doped and undoped single and polycrystalline Al_2O_3	36
Figure 6. Normalized conductivity for phosphate glasses as a function of the oxidation state of the TMI.....	44
Figure 7. Electrical conductivity of binary silicate systems: FeO - SiO_2 , CaO - SiO_2 and Al_2O_3 - SiO_2 ...	48
Figure 8. Anode current efficiency measured in the electrolysis of iron oxide-containing silicate melts.....	50
Figure 9. Electrical conductivity of iron-oxide-containing melts as a function of oxygen partial pressure.....	53
Figure 10. Application of the regular solution model to liquid iron oxide melt at 1600°C.....	59
Figure 11. The Fe^{3+}/Fe^{2+} ratio in iron silicate melt (at 1550°C, $x'_{SiO_2} = 0.1$) as a function of oxygen partial pressure.....	61
Figure 12. The Fe^{3+}/Fe^{2+} ratio in iron silicate melt (at 1550°C, $x'_{SiO_2} = 0.2$) as a function of oxygen partial pressure.....	62

	Page
Figure 13. The $\text{Fe}^{3+}/\text{Fe}^{2+}$ ratio in iron silicate melt (at 1550°C , $x_{\text{SiO}_2} = 0.3$) as a function of oxygen partial pressure.....	63
Figure 14. Fractionation curves in the $\text{FeO}\cdot\text{Fe}_2\text{O}_3\text{-Al}_2\text{O}_3\text{-SiO}_2$ system, after Muan, ref. 25.....	64
Figure 15. Isothermal activities of Fe_2O_3 in iron aluminosilicate melt.....	68
Figure 16. Isothermal activities of FeO in iron aluminosilicate melt.....	69
Figure 17. Isothermal activities of Al_2O_3 in iron aluminosilicate melt.....	70
Figure 18. Comparison of $\text{Fe}^{3+}/\text{Fe}^{2+}$ ratios in $\text{FeO}\text{-Fe}_2\text{O}_3\text{-SiO}_2$ and $\text{FeO}\cdot\text{Fe}_2\text{O}_3\text{-Al}_2\text{O}_3\text{-SiO}_2$ systems..	73
Figure 19. Schematic of the conductivity cell design....	79
Figure 20. Cell constant as a function of liquid level in the conductivity cell.....	83
Figure 21. I-V characteristic of the conductivity circuit at 1347°C	85
Figure 22. Circuit of the voltage controlled current source.....	86
Figure 23. Location of the compositions investigated (with 7 and 17 wt% SiO_2) with respect to the $\text{FeO}\cdot\text{Fe}_2\text{O}_3\text{-Al}_2\text{O}_3\text{-SiO}_2$ system.....	93
Figure 24. Temperature dependence of the electrical conductivity of composition $73\text{Fe}_3\text{O}_4\text{-}20\text{Al}_2\text{O}_3\text{-}7\text{SiO}_2$	96
Figure 25. Temperature dependence of the electrical conductivity of composition $53\text{Fe}_3\text{O}_4\text{-}30\text{Al}_2\text{O}_3\text{-}17\text{SiO}_2$	97
Figure 26. Temperature dependence of the electrical conductivity of composition $63\text{Fe}_3\text{O}_4\text{-}20\text{Al}_2\text{O}_3\text{-}17\text{SiO}_2$	98
Figure 27. Electrical conductivity as a function of temperature for composition $73\text{Fe}_3\text{O}_4\text{-}20\text{Al}_2\text{O}_3\text{-}7\text{SiO}_2$	100

	Page
Figure 28. Microstructure of a sample of composition $73\text{Fe}_3\text{O}_4-20\text{Al}_2\text{O}_3-7\text{SiO}_2$ quenched from 1526°C . (Magnification 200X)..	102
Figure 29. The microstructure of a sample of composition $73\text{Fe}_3\text{O}_4-20\text{Al}_2\text{O}_3-7\text{SiO}_2$ annealed in air at 1250°C for 24 hours. (Magnification 50x).....	103
Figure 30. Isothermal ac-conductivity as a function of frequency for composition $73\text{Fe}_3\text{O}_4-20\text{Al}_2\text{O}_3-7\text{SiO}_2$	105
Figure 31. Electrical conductivity as a function of temperature for composition $63\text{Fe}_3\text{O}_4-30\text{Al}_2\text{O}_3-7\text{SiO}_2$	108
Figure 32. Electrical conductivity as a function of temperature for composition $58\text{Fe}_3\text{O}_4-35\text{Al}_2\text{O}_3-7\text{SiO}_2$	110
Figure 33. Electrical conductivities of four composition within the $s_1s_2m_2m_1$ quadrilateral.....	111
Figure 34. Microstructure of a sample of $63\text{Fe}_3\text{O}_4-30\text{Al}_2\text{O}_3-7\text{SiO}_2$ annealed in air at 1250°C for 24 hours. (Magnification 200x).....	114
Figure 35. Isothermal ac-conductivity as a function of frequency for composition $63\text{Fe}_3\text{O}_4-30\text{Al}_2\text{O}_3-7\text{SiO}_2$	115
Figure 36. Isothermal ac-conductivity as a function of frequency for composition $48\text{Fe}_3\text{O}_4-45\text{Al}_2\text{O}_3-7\text{SiO}_2$	116
Figure 37. Isothermal ac-conductivity as a function of frequency for composition $33\text{Fe}_3\text{O}_4-50\text{Al}_2\text{O}_3-17\text{SiO}_2$	117
Figure 38. Electrical conductivities as a function of temperature for compositions within the compatible triangle $s_1m_1c_1$	119
Figure 39. Microstructure of a sample of composition $47\text{F}-46\text{A}-7\text{S}$ annealed in air at 1250°C for 24 hours. (Magnification 100x).....	120

	Page
Figure 40. The calculated electrical conductivity of mullite of composition 13.09 w/o Fe ₂ O ₃ 61.4 w/o Al ₂ O ₃ 25.5 w/o SiO ₂	121
Figure 41. Microstructure of a sample of composition 23F-70A-7S annealed in air at 1250°C for 24 hours. (Magnification 200x).....	123
Figure 42. Electrical conductivity as a function of temperature for composition 23Fe ₃ O ₄ -70Al ₂ O ₃ -7SiO ₂	124
Figure 43. Isothermal ac-conductivity as a function of frequency for composition 23Fe ₃ O ₄ -70Al ₂ O ₃ -7SiO ₂	126
Figure 44. The microstructure of a sample of composition 63Fe ₃ O ₄ -30Al ₂ O ₃ -7SiO ₂ quenched from 1495°C in air, showing the segregation of phases...	128
Figure 45. Isothermal electrical conductivity in air at 1550°C as a function of composition.....	129
Figure 46. Plot of $\log \frac{\sigma T}{c(1-c)}$ versus reciprocal temperature for iron aluminosilicate melts.....	131
Figure 47. Isothermal dc-conductivity as a function of oxygen partial pressure for iron aluminosilicate melts.....	132
Figure 48. Isothermal dc-conductivity as a function of oxygen partial pressure for iron aluminosilicate melts above the liquidus temperature.....	134
Figure 49. Isothermal dc-conductivity as a function of Fe ³⁺ /Fe _{total} ratio in iron aluminosilicate melts.....	135
Figure 50. Illustration of several crystallization sequences in the FeO·Fe ₂ O ₃ -Al ₂ O ₃ -SiO ₂ system.....	137
Figure 51. Electrical conductivity of Al ₂ O ₃ as a function of iron content at 1250°C in air...	148

	Page
Figure 52. Free carrier mobility as a function of temperature, based on the conduction band model.....	152
Figure 53. Electrical conductivity in iron aluminosilicate melt as a function of ferrous ion concentration.....	154
Figure 54. Effective mobility as a function of temperature, based on the polaron hopping model (R_{Fe} assumed to be constant).....	155
Figure 55. Fe^{3+} distribution factor, R_{Fe} , as a function of composition in iron aluminosilicate melts.....	157

LIST OF TABLES

	Page
Table I. Analysis of XA-139 high purity Al_2O_3	77
Table II. Wet chemical analysis of $\text{FeO}\cdot\text{Fe}_2\text{O}_3$ - Al_2O_3 - SiO_2 samples.....	81
Table III. Standards used for composition analysis in the M.I.T. Earth and Planetary Electron Microscopy Facility	91
Table IV. X-ray diffraction pattern for $73\text{Fe}_3\text{O}_4$ - $20\text{Al}_2\text{O}_3$ - 7SiO_2 melted and held at 1250°C for 24 hours, with Fe x-ray, MnO filter.....	104
Table V. X-ray diffraction pattern for $63\text{Fe}_3\text{O}_4$ - $30\text{Al}_2\text{O}_3$ - 7SiO_2 melted and held at 1250°C for 24 hours, without filter.....	113

Acknowledgements

I am very thankful to Professor H. Kent Bowen for his guidance, patience and understanding throughout the past years. I also express my gratitude to Professors H. L. Tuller and T. B. King for their valuable suggestions, advice and encouragement. Useful discussions with Professors J. F. Elliot, B. J. Wuensch and R. M. Cannon are also gratefully acknowledged. Dr. D. Reed and Mr. T. O. Mason have helped me enormously with numerous stimulating discussions. I am indebted to Dr. Reed for his help. The technical support of Mr. P. A. Kearney, Mr. A. E. Freker, Mr. J. Centorino, Mr. F. D. Wilson and Mr. R. Stanton is very much appreciated. Special thanks also goes to Ms. B. McDonald for typing this manuscript during this holiday season.

The friendship of my colleagues in the Ceramics group has also made my stay at M.I.T. pleasant and rewarding. I wish to thank Professor R. L. Coble, Drs. U. Chowdhry and K. Uematsu, T. D. Ketcham, I. Lloyd, N. Johnston, P. Lemaire, Mrs. B. L. Baker, Mrs. L. Van Uitert and many others. I am especially grateful to Professor R. L. Coble because he first got me involved in Ceramics through his enthusiasm toward research.

I remember my sister and parents. I thank Walter, Richard, Lucy and many other brother and sisters of the Boston Chinese Bible Study Group for their prayer support.

The financial support of Energy Research & Development Administration, contract #E(49-18)-2215, is gratefully acknowledged.

Chapter I. Introduction

The present study on the electrical conductivity of the $\text{FeO}\cdot\text{Fe}_2\text{O}_3\text{-Al}_2\text{O}_3\text{-SiO}_2$ system is motivated by two underlying factors. First, it is undertaken because of its indirect association with the development of electrode material for coal-fired MHD power generators. Also, very little is known about the conduction mechanisms in the system. Any contribution to the understanding and modelling of the electrical conduction process is important.

The MHD electrodes must be resistive to corrosion and be compatible with the operating conditions in the channel. Hence, critical requirements are imposed on the electrode material in view of the extremely adverse channel environment. It must be of high electronic conductivity with a low temperature dependence and of good electron emissivity. For materials with appreciable ionic conductivity, a redox reaction occurs at the metal current lead-out, reducing the lifetime of the electrode module.

Iron aluminum spinel has been proposed as a candidate material for the electrode. A graded type electrode, with the hot end richer in hercynite (FeAl_2O_4) and the cooled electrode/metal interface magnetite (Fe_3O_4) rich, was proposed.⁽¹⁾ Because of its apparently advantageous features like a high electronic conductivity and low temperature dependence and the absence of a resistive reaction layer, there has been active

research of the chemical and electrical properties of the Fe-Al-O system.

However, it must also be realized that in the MHD channel, there may be a thin layer of slag of the order of 1 mm thick deposited on the electrode surface. The slag is carried over from the combustor and becomes an integral part of the electrode assemblage. Its properties and chemical compatibility with the electrode material are therefore important factors in the overall performance of the electrode. The slag composition and thickness vary according to the type of coal used, the plasma temperature, the temperature at the electrode/slag interface and the viscous drag forces of the moving gas boundary layer. The slag compositions vary: 40-50 w/o SiO_2 , 15-30w/o Al_2O_3 , 5-15w/o ($\text{FeO}+\text{Fe}_2\text{O}_3$), 5-15w/o CaO , 1-5w/o MgO and different amounts of Na, K and Ti.

As a result of the large percentage of the oxides FeO , Fe_2O_3 , Al_2O_3 and SiO_2 in the slag, it is natural that the $\text{FeO}\cdot\text{Fe}_2\text{O}_3\text{-Al}_2\text{O}_3\text{-SiO}_2$ system is chosen as a model for the slag system interacting with the spinel electrode. Besides the engineering applications, an equally important initiative for this work is the study of conduction mechanisms in molten, glassy and crystalline silicates.

The $\text{FeO}\cdot\text{Fe}_2\text{O}_3\text{-Al}_2\text{O}_3\text{-SiO}_2$ system is complicated. The compositions studied are those of low silica content. The electrical conductivity has been measured as a function of composition, temperature and oxygen partial pressure. It is

primarily electronic in nature. The results can be interpreted with a detailed understanding of the phase chemistry. In the next chapter, the phase equilibria of the system is reviewed together with the possible conduction models and literature related to the present work.

The thermodynamic activities of the species FeO , Fe_2O_3 and Al_2O_3 are then discussed with the emphasis that alumina behaves as a neutral oxide in the iron aluminosilicate melt and its addition has negligible effect on the $\text{Fe}^{3+}/\text{Fe}^{2+}$ equilibrium. Interesting insights can be obtained by using a very simple thermodynamic approach to model the system.

Above the solvus, the iron aluminosilicate melt is in equilibrium with a suspension of spinel, corundum and/or mullite particles. Below the solvus, the solid aggregates are composed of mixtures of varying amounts of spinel, corundum, mullite or glassy silicates. Here the data are interpreted in terms of conduction models for multiphase composites. The results are also discussed with respect to two possible conduction mechanisms: the classical conduction band model and the thermally activated hopping model which has been suggested for glasses and melts containing transition metal ions.

Chapter II. Theory and Literature Review

The high temperature electrical conductivity data for iron-containing silicate systems are very limited. Studies of the conductivity of silicate melts and slags have been made by metallurgists and more recently by Russian researchers. Nevertheless, little is known about the conduction mechanism in iron-containing silicate melts. Meanwhile low temperature conductivity results of semiconducting oxide glasses containing transition metal ions (TMI) are readily available and polaron hopping mechanism has been accepted as that responsible for the electronic conduction in these systems. There is only one publication on conduction in crystalline iron ortho-silicate.

This chapter is divided into three main sections. The first one is a brief examination of two models, the band theory and the polaron hopping model, which are possible mechanisms for conduction in the $\text{FeO}\cdot\text{Fe}_2\text{O}_3\text{-Al}_2\text{O}_3\text{-SiO}_2$ system. This theoretical treatise is necessary because it provides the basis for the identification of the conduction mechanism in the system. The same section also includes a short review on multiphase conduction models. Since the crystallization products of the compositions studied are mixtures of spinel, corundum, mullite or glass, the net effect of these phases on the total conductivity of the composite has to be interpreted by these models.

The section following is a review of the phase equilibria in the $\text{FeO}\cdot\text{Fe}_2\text{O}_3\text{-Al}_2\text{O}_3\text{-SiO}_2$ system, in air and as a function of

oxygen partial pressure. Special emphasis is placed on the structure and electrical conductivity of iron aluminum spinel, corundum and mullite.

The last section of the chapter contains a summary of the literature of the conductivity of semiconducting oxide glasses with TMI, of iron and vanadium phosphate glasses and of silicate melts.

II.1. Theory

II.1.1 Conduction Models

The electrical conductivity of a material is defined by the expression,

$$\sigma = \sum_i^{\ell} n_i z_i e \mu_i \quad (1)$$

where ℓ is the number of different kinds of electronic and ionic charge carriers contributing to the conduction, n_i is the concentration of each carrier, $z_i e$ is the charge on each and μ_i its mobility. For an ionic species, the mobility is related to its diffusion coefficient by the Nernst-Einstein equation. As the conductivity in the $\text{FeO}\cdot\text{Fe}_2\text{O}_3\text{-Al}_2\text{O}_3\text{-SiO}_2$ system is predominantly electronic, this section will only be a summary of the electronic conduction models pertaining to the present system.

Electronic conductivity in materials is commonly described in terms of the classical energy band model. However, for systems containing transition metal ions, the possibility of

conduction by polaron hopping cannot be neglected. Both models have been reviewed extensively in the literature⁽²⁻⁹⁾; the purpose of this section is to point out and contrast the fundamental conceptual differences between the two, particularly on the temperature dependence of the terms n_i and μ_i .

For the band theory, a normally filled valence band of a semiconductor or insulator is separated from the empty conduction band by an energy gap, E_g . In the intrinsic region, electronic conduction is possible by the thermal excitation of electrons and holes* across this energy gap. The concentration of the carriers is,

$$n_e = 2 \left(\frac{2\pi m_e^* kT}{h^2} \right)^{3/2} e^{-(E_g/2kT)} \quad (2)$$

where m_e^* is the effective mass of the electron and h is Planck's constant.

If a relatively electronegative impurity center of concentration N_I is present, localized states are extended at an energy level E_I into the band gap. At a certain temperature, part of these donor states are ionized. Here, the concentration of electrons excited into the conduction band is

$$n_e = N_I \exp(-E_I/kT) \quad (3)$$

In the conduction band, the mobility of the electron is limited by scattering due to lattice imperfections. In highly

*For simplicity sake, only n-type conduction is considered in this section.

disordered systems, this scattering by phonons and impurities is significant. Impurity scattering dominates at low temperatures, with $\mu_i \propto T^{3/2}$. At higher temperatures, the major scattering is due to phonons, giving $\mu_i \propto T^{-3/2}$.

As the temperature dependence of the mobility is algebraic rather than exponential, the thermal activation energy obtained from the slope of a $\log \sigma$ versus reciprocal temperature plot reflects the energy required for the excitation of the carriers.

When strong electron-phonon coupling exists, an electron can be trapped in a potential well generated by the lattice distortion due to its coulombic force. The electron in this bound state and the local lattice deformation associated with it is a polaron. Once localized, the polaron can hop to a neighboring unoccupied site, carrying with it the lattice distortion. At temperatures above half the Debye temperature, this motion of the polaron is regarded as a diffusive one and is thermally activated. Holstein³ showed that the thermally activated mobility of the polaron is,

$$\mu = \frac{\nu e a^2}{kT} \exp(-2\alpha a) \exp(-W/kT) \quad (4)$$

where ν is the jump frequency, $\exp(-2\alpha a)$ is a tunneling probability for the non-adiabatic case and a is the distance between centers. The thermal activation energy is made up of two terms,

$$W = W_H + \frac{1}{2} W_D \quad (5)$$

W_H is half the polaron energy and W_D is the energy difference between neighboring sites.

Mott^(5,10,11) has extended this polaron model to the conduction in glasses and melts containing transition metal ions. The conduction mechanism is one of electron transfer between donor (Fe^{2+} , V^{4+}) and acceptor (Fe^{3+} , V^{5+}) centers and is similar to impurity band conduction in doped and compensated semiconductors. The electrical conductivity is expressed as,

$$\sigma = Nc(1-c) \frac{ve^2 a^2}{kT} \exp(-2\alpha a) \exp(-W/kT) \quad (6)$$

where c is the fraction of ions with the higher valency, the $c(1-c)$ term accounts for the probability that neighboring sites are of different oxidation states, N is the concentration of the transitional metal ions and v is the jump frequency. The $\exp(-2\alpha a)$ term is a tunnelling probability for the non-adiabatic case. Sayer and Mansingh⁽¹²⁾ could not observe this term for phosphate glasses with different TMIs. They concluded that small polaron hopping in the adiabatic approximation was appropriate for glasses of different compositions within the same system.

In summary, the principal difference between the band model and the polaron hopping model is in the temperature dependence of the carrier concentration and mobility. In the band model, the charge carriers are tunnelled from site to site with the temperature dependence of the conductivity determined by the change in the carrier concentration. However, for the

polaron hopping model, the number of carriers is considered constant and the mobility is thermally activated. In his model, Mott assumed that all the TMIs participate in the conduction process and that all Fe^{2+} and Fe^{3+} sites are equivalent. This may not be true.

Boon⁽¹³⁾ has studied the coordination number of ferrous ions in a wide variety of silicate glasses and found that less than 0.5% of all ferrous ions occupy tetrahedral sites. Kurkjian⁽¹⁴⁾ measured the Mossbauer, optical and electron paramagnetic spectra of ferric ion in phosphate and silicate glasses. The isomer shifts and ligand field parameters indicated that the Fe^{3+} was predominantly tetrahedrally coordinated in silicates and octahedrally coordinated in phosphates. This was in disagreement with Edward's⁽¹⁵⁾ finding that the position and intensity of the Fe^{3+} d-d absorption bands in $\text{MO}\cdot\text{P}_2\text{O}_5$ glasses were consistent with an octahedral environment.

Taragin⁽¹⁶⁾ also suggested that both ferrous and ferric ions were in octahedral coordination in aluminophosphate glass from room temperature to 450°C. But Loveridge⁽¹⁷⁾ proposed models for the four-fold and six-fold coordination of Fe^{3+} ion in $\text{Na}_2\text{O}\cdot\text{B}_2\text{O}_3$, $\text{Na}_2\text{O}\cdot\text{SiO}_2$ and $\text{K}_2\text{O}\cdot\text{SiO}_2$ glasses.

Pargamin et al.⁽¹⁸⁾ equilibrated $\text{CaO}\text{-Fe}_2\text{O}_3\text{-SiO}_2$ and $\text{Na}_2\text{O}\text{-Fe}_2\text{O}_3\text{-SiO}_2$ melts at 1550°C in air and then rapidly quenched them as glasses. They used Mossbauer spectroscopy to study the repartition of iron between Fe^{2+} and Fe^{3+} and the

distribution of Fe^{3+} ions among octahedral and tetrahedral coordinations. The ferric ions were found to be tetrahedrally coordinated in the alkaline silicate glasses. 45-70% of the Fe^{3+} were octahedrally coordinated in the Fe_2O_3 -CaO-SiO₂ glasses. The effect of alumina addition was found to be dependent on composition. Their results for the Fe_2O_3 -Al₂O₃-CaO-SiO₂ system are summarized in Figure 1.

Should the Fe^{3+} ion prefer tetrahedral coordination in the glass or the melt, it is part of the network former and is covalently bounded to the silicate anion. It would not participate in the conduction process. To account for the fraction of Fe^{3+} ions not in octahedral coordination, the appropriate equation for the hopping model is presently defined as

$$\sigma = N R_{\text{Fe}} c(1-c) \frac{ve^2 a^2}{kT} \exp(-2\alpha a) \exp(-W/kT) \quad (7)$$

with

$$R_{\text{Fe}} = \frac{\text{Fe}_{\text{oct}}^{3+}}{\text{Fe}_{\text{total}}^{3+}}$$

II.1.2. Electrical Conductivity in Composite Systems

The crystallization products of the $\text{FeO} \cdot \text{Fe}_2\text{O}_3$ -Al₂O₃-SiO₂ system in air are mixtures of a number of phases. Thus the measured electrical conductivity would be an effective value and must be analyzed using multiphase conduction models. Numerous theoretical and empirical correlations are found in the literature and have been applied to properties such as electrical and thermal conductivity, dielectric

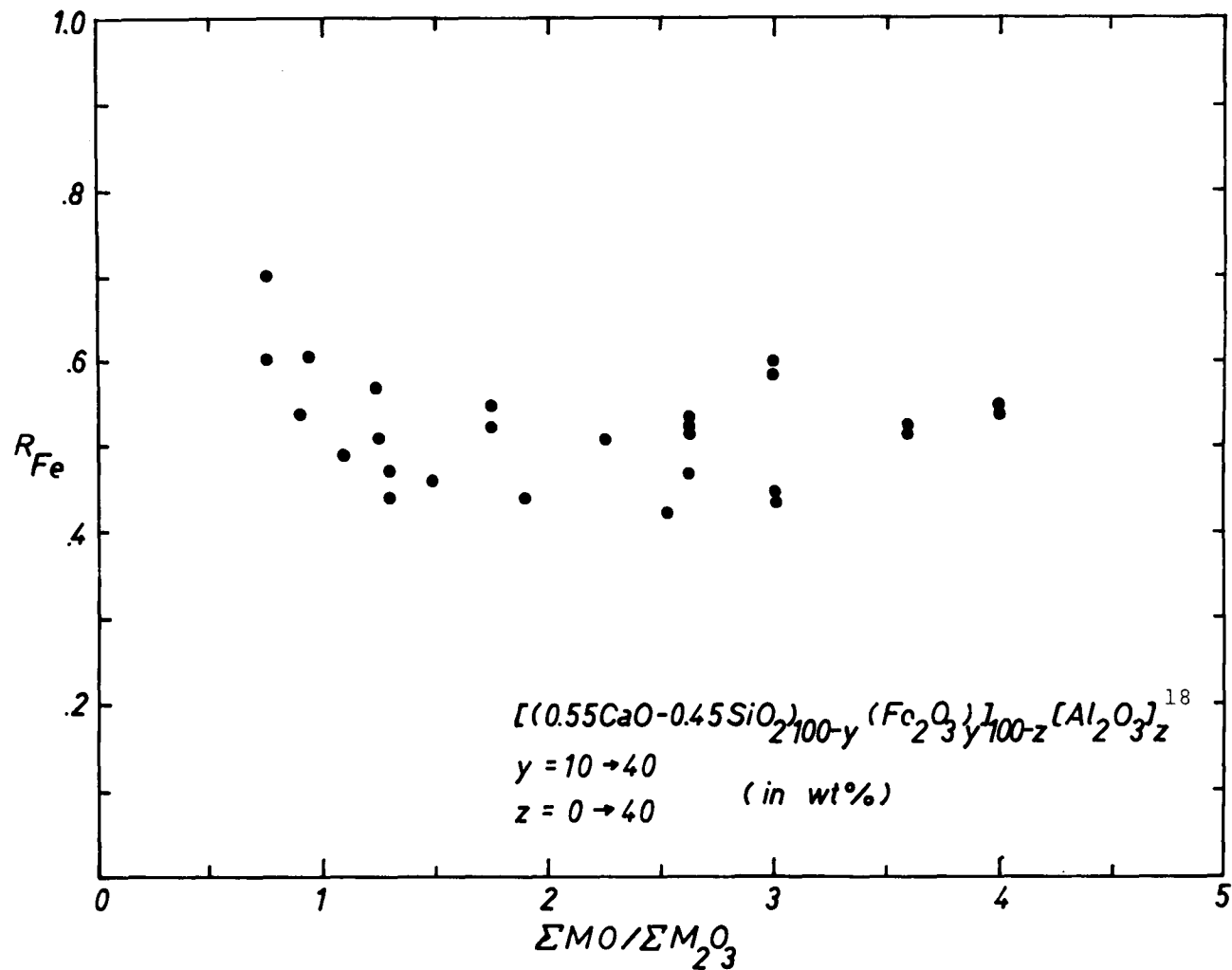


Figure 1. The distribution of Fe^{3+} ions among octahedral and tetrahedral coordinations in the Fe_2O_3 -CaO- Al_2O_3 - SiO_2 system as a function of composition.

constant, magnetic permeability and so forth, of a composite medium. The models are derived for random and ordered arrangements of the dispersed phases. Geometric factors are introduced to account for the shape of the particles and also their orientation and type of packing. The models are tested experimentally with composites made up of materials (conductors and insulators) of known conductivities. The tests indicated that no one model can accurately predict the conductivity of all types of composite. Review papers have been written by Meredith and Tobias,⁽¹⁹⁾ Ondracek⁽²⁰⁾ and Progelfhof et al.⁽²¹⁾. Because of the sheer number of models documented, only the more relevant ones are reviewed here.

Maxwell⁽²²⁾ first considered the effective conductivity of equivalent, spherical particles of conductivity σ_d imbedded in a matrix of conductivity σ_c . The effective conductivity σ_{eff} of the composite is,

$$\sigma_{eff} = \frac{2\sigma_d + \sigma_c + f(\sigma_d - \sigma_c)}{2\sigma_d + \sigma_c - 2f(\sigma_d - \sigma_c)} \cdot \sigma_c \quad (8)$$

where f is the volume fraction of the dispersed phase. His equation was derived by solving the Laplace equation for the potential inside and around the particles. This expression is for the conductivity of randomly distributed non-interacting spheres in a homogeneous continuous medium. It can be applied for f up to 0.1.

For a dispersion of more than 2 phases, the equation was

modified to

$$\left(\frac{\sigma_{\text{eff}}}{\sigma_c} - 1\right) / \left(2 \frac{\sigma_{\text{eff}}}{\sigma_c} + 1\right) = \sum_i \left(\frac{\sigma_{d_i}}{\sigma_c} - 1\right) f_i / \left(2 \frac{\sigma_{d_i}}{\sigma_c} + 1\right) \quad (9)$$

Grekila and Tien⁽²³⁾ used a tetrakaidekahedral model to fit the conductivity data of the ZrO_2 -CaO system with 0.22-0.50 mole fraction of CaO. It was a geometric model of conducting and insulating phases with the microstructure ranging from either or both phases being the continuum. Their model predicted the discontinuity in conductivity at 39 mole % CaO.

Bruggeman⁽²⁴⁾ realized that for concentrated mixtures, the conductivity of the aggregate should be used in the derivation instead of the conductivity of the continuum. He derived the empirical formula,

$$\frac{\left(\frac{\sigma_{\text{eff}}}{\sigma_c} - \frac{\sigma_d}{\sigma_c}\right)^{1/3}}{\left(\frac{\sigma_{\text{eff}}}{\sigma_c}\right) \left(1 - \frac{\sigma_d}{\sigma_c}\right)} = 1 - f. \quad (10)$$

This expression holds well for a large range of particle sizes in the matrix.

II.2. The $\text{FeO}\cdot\text{Fe}_2\text{O}_3$ - Al_2O_3 - SiO_2 System.

The phase equilibria in this system have been studied by Muan.^(25,26) The four component system can be described by a tetrahedron with FeO , Fe_2O_3 , Al_2O_3 and SiO_2 at the corners.

In Figure 2 the plane $\text{FeO}\cdot\text{Fe}_2\text{O}_3\text{-Al}_2\text{O}_3\text{-SiO}_2$ is outlined inside the tetrahedron. Also shown is the 0.21 atmosphere oxygen (air) isobaric liquidus surface represented by the dotted and dashed grid to illustrate its position relative to the $\text{FeO}\cdot\text{Fe}_2\text{O}_3\text{-Al}_2\text{O}_3\text{-SiO}_2$ plane. The dotted and dashed lines such as CB and AD are parallel to the $\text{FeO}\text{-Fe}_2\text{O}_3\text{-Al}_2\text{O}_3$ basal plane and are lines of isosilica content. AB is the locus of points where the surface intersects the $\text{FeO}\cdot\text{Fe}_2\text{O}_3\text{-Al}_2\text{O}_3\text{-SiO}_2$ plane. The dotted lines indicate that the liquidus surface is to the left and Fe_2O_3 side of the plane as the $\text{wt}\%\text{Fe}_2\text{O}_3/\text{wt}\%\text{FeO}$ ratio is greater than 2.22. At higher silica and alumina contents the surface is on the right and FeO side of the plane (dashed lines).

Because of the close proximity of the liquidus surface to the $\text{FeO}\cdot\text{Fe}_2\text{O}_3\text{-Al}_2\text{O}_3\text{-SiO}_2$ plane, Muan has projected it onto the plane and treated it as if it were a true ternary system of $\text{FeO}\cdot\text{Fe}_2\text{O}_3\text{-Al}_2\text{O}_3\text{-SiO}_2$ (Figure 3). Parts of the 1400° , 1500° and 1600°C isotherms are included. The light dashed lines are lines passing through points of equal $\text{wt}\%\text{Fe}_2\text{O}_3/\text{wt}\%\text{FeO}$ ratios along the liquidus surface.

There are four primary phase fields in which a crystalline phase coexists with the melt. They are spinel, corundum, mullite and cristobalite (tridymite at lower temperatures). P is a piercing point at 1460°C where spinel (ss), corundum (ss), mullite (ss), melt (17 w/o FeO, 38w/o Fe_2O_3 , 25w/o Al_2O_3 and 20w/o SiO_2) and a gas phase ($P_{\text{O}_2} = 0.21 \text{ atm}$) are in equilibrium.

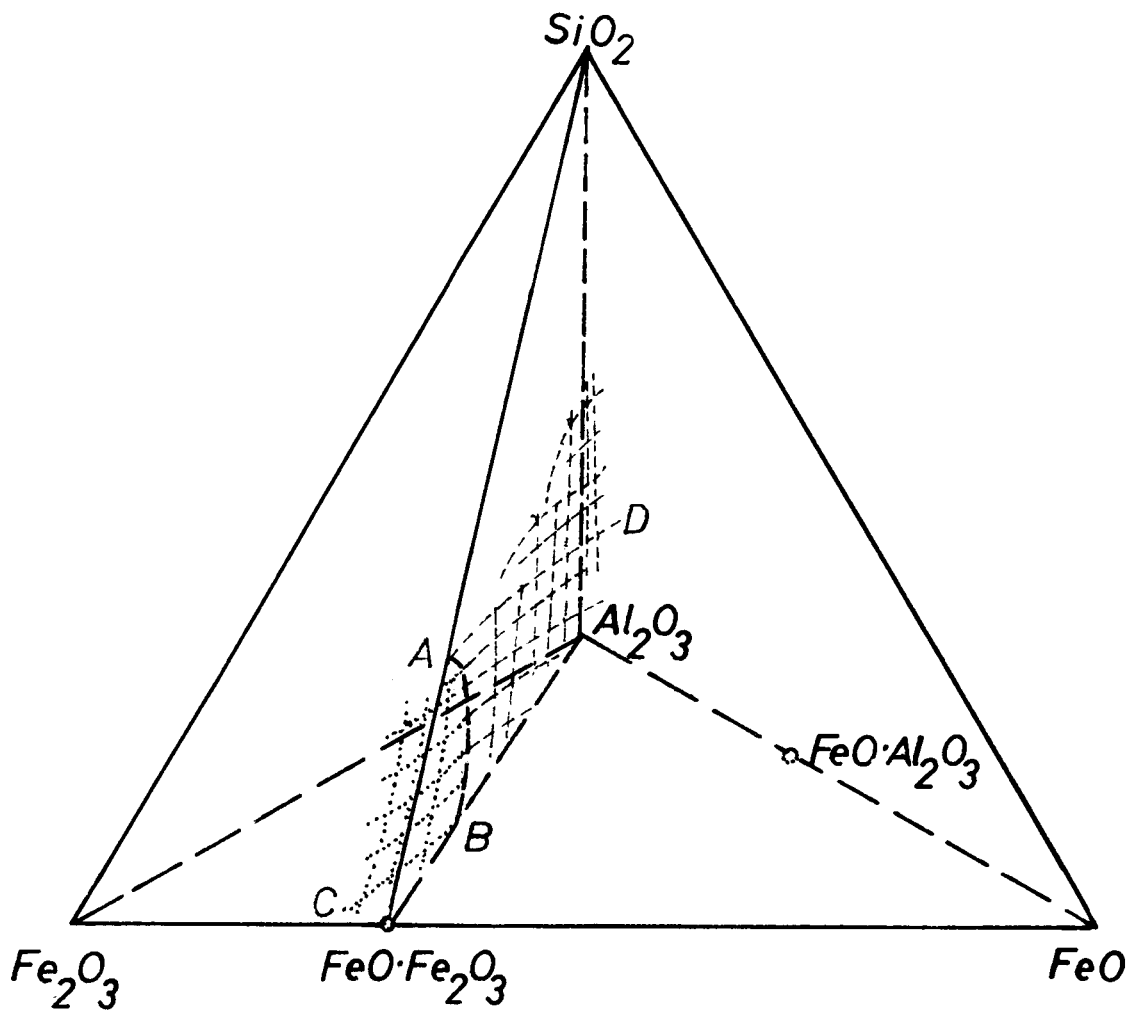


Figure 2. The $\text{FeO}\cdot\text{Fe}_2\text{O}_3\text{-Al}_2\text{O}_3\text{-SiO}_2$ system with the 0.21 atmosphere oxygen isobaric liquidus surface included.

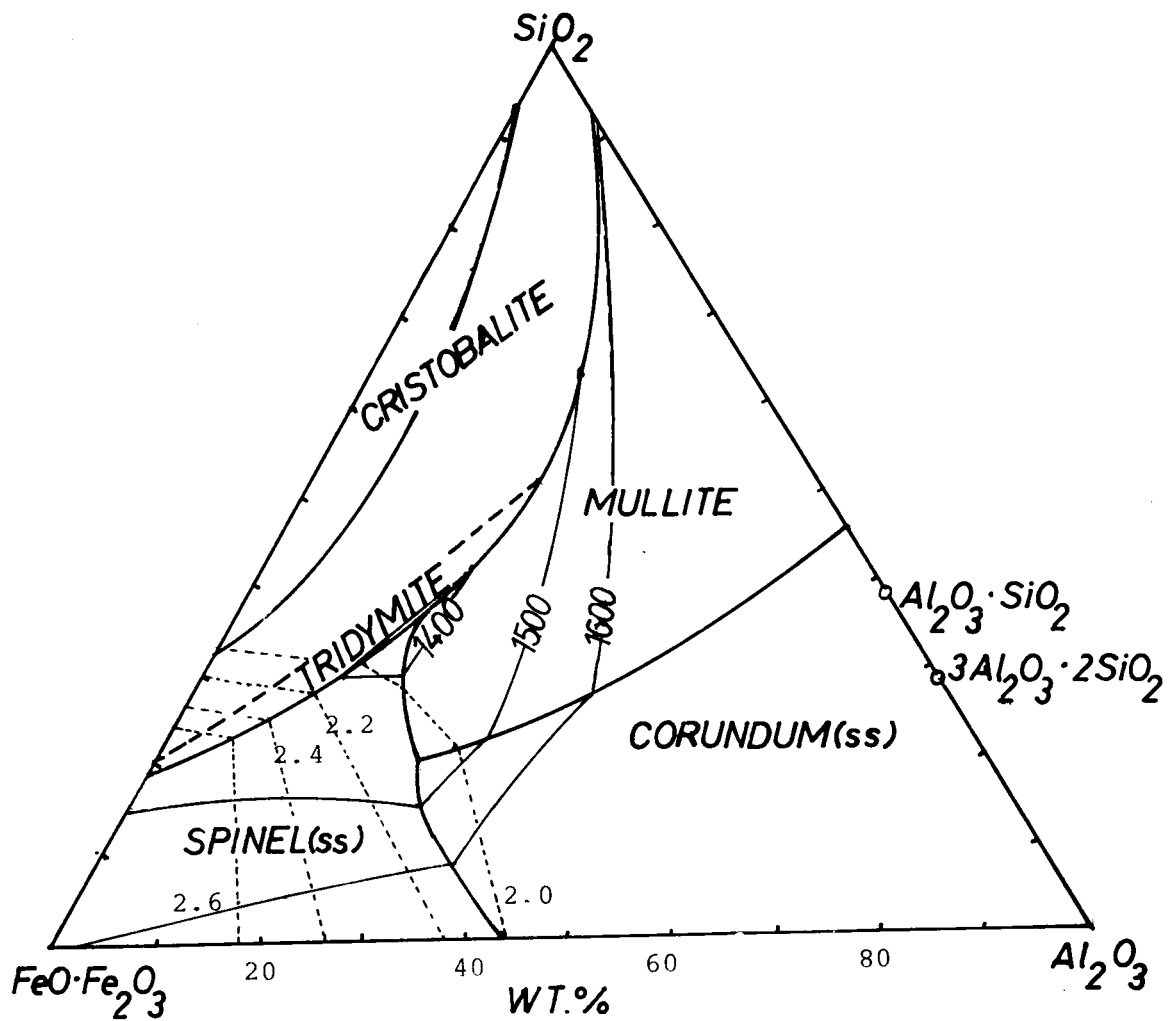


Figure 3. Projection of the 0.21 atmosphere oxygen isobaric liquidus surface onto the $\text{FeO}\cdot\text{Fe}_2\text{O}_3\text{-Al}_2\text{O}_3\text{-SiO}_2$ plane. (After Muan, Ref. 25)

Another piercing point is E. It is the lowest temperature (1380°C) where the melt can exist in air. Here the phases in equilibrium are spinel(ss), tridymite, mullite (ss), melt (16w/o FeO, 25w/o Fe₂O₃, 19w/o Al₂O₃ and 40w/o SiO₂) and the gas phase.

In sharp distinction to the phase equilibria in air, six piercing points are present on the 1 atm oxygen liquidus surface.⁽²⁶⁾ Two new primary phase fields are added, hematite (ss) and Fe₂O₃·Al₂O₃. The highest piercing point is at 1495°C where spinel (ss), corundum (ss), Fe₂O₃·Al₂O₃, melt and oxygen are in equilibrium. The lowest one is at 1390°C, where tridymite, hematite(ss), mullite(ss), melt and the gas phase coexist.

Fewer data are available pertaining to phase relationships at lower P_{O₂}. However, the qualitative effect of lower oxygen partial pressure is to enhance the spinel and corundum phase fields. The temperature of the liquidus surface is also lowered. A wustite phase field appears at about 10⁻¹⁰ P_{O₂} atmosphere.

The spinel, corundum and mullite phases all exhibit varying degrees of solid solution behavior with temperature and P_{O₂}. The iron aluminum spinel is a complete solid solution of the end members magnetite (Fe₃O₄) and hercynite (FeAl₂O₄). The corundum has some Fe₂O₃ in solid solution. Mullite (3Al₂O₃·2SiO₂) is even more complicated. It not only can have variations in the Fe/(Fe+Al) ratio but also in the Si/(Al+Fe)

ratio. All these factors lead to very complicated crystallization sequences, as will be shown in a later chapter.

As the compositions of major concern in this study lie in the spinel and corundum phase fields, the structure, defects and conductivity of iron aluminum spinel, corundum and mullite will be reviewed.

II.2.1. Iron Aluminum Spinel.

The spinel structure has oxygen ions arranged in a face-centered close packed lattice. The cations distribute themselves among the octahedral and tetrahedral sites. Magnetite is an inverse spinel with half of its Fe^{3+} ions in the tetrahedral sites. The rest of the Fe^{3+} and the Fe^{2+} fill half of the existing octahedral sites. Hercynite has a normal spinel structure which means that the Al^{3+} ions prefer the octahedral interstices while the Fe^{2+} ions fill one-eighth of the tetrahedral sites. The thermodynamics of cation distribution in binary spinels has been studied by Navrotsky.⁽²⁷⁾ The molar enthalpy of interchange of cations on the octahedral and tetrahedral sites was calculated with configurational entropy considered as the only consequence of the disordering. Empirical tetrahedral and octahedral site preference energies were obtained for a series of divalent and trivalent cations in spinel.

The conductivity of magnetite has been studied by Miles⁽²⁸⁾ and also by Tannhauser.⁽²⁹⁾ The conductivity at high temperatures was only slightly temperature dependent and was of n-type.

The results were explained by an electron-transfer model between ferrous and ferric ions on octahedral sites. Hence the conductivity was proportional to the product of the concentration of each species. Tannhauser concluded that the normal free electron in a band model was inappropriate for interpreting the conductivity data.

The conductivity of hercynite and iron aluminum spinels of different compositions have been studied recently by Mason⁽³⁰⁾. Some of the results are included in Figure 4 together with Miles's for magnetite. Addition of 70 mole% FeAl_2O_4 still did not affect the contour of the conductivity plot to any large extent.

II.2.2. Corundum

The corundum structure has a hexagonal close-packed oxygen sublattice with two-thirds of the octahedral voids filled by aluminum ions. All the tetrahedral sites are empty. The cations are arranged along the c-axis such that each pair of aluminum ions is separated by an unoccupied octahedral site.

Because Al_2O_3 is such a wide band gap material, the electrical properties are usually controlled by the aliovalent impurities present. This is reflected in the activation enthalpy for conduction in the extrinsic range at low temperature. Due to the enormous number of publications on the subject, only the more significant work on the electrical conductivity is reviewed.

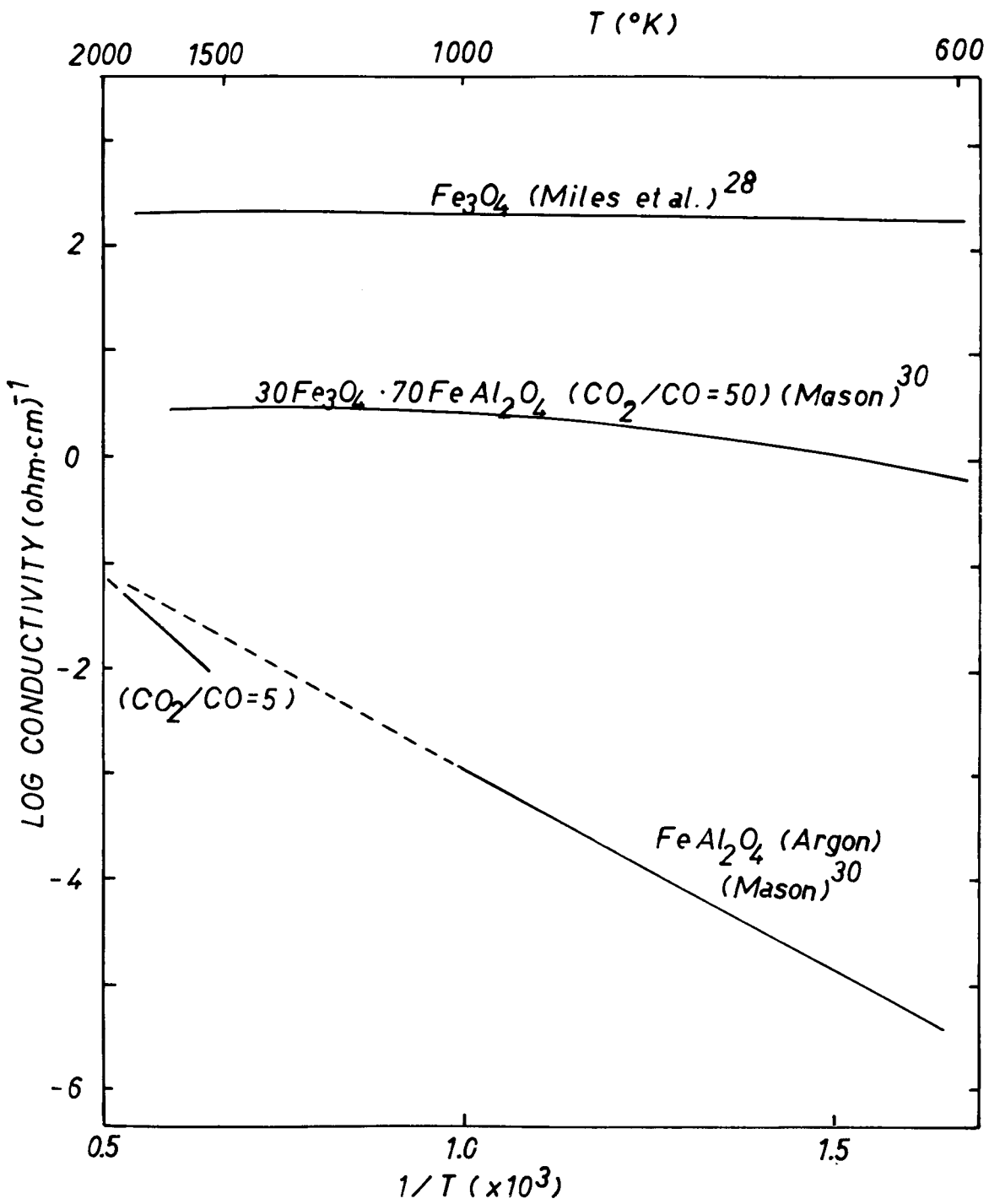


Figure 4. Electrical conductivities of Iron Aluminum Spinels and Magnetite (After T.O. Mason³⁰).

Pappis and Kingery⁽³¹⁾ reported that single crystal alumina was an n-type conductor at low oxygen partial pressure, changing to p type conduction at high partial pressures. The activation energy for conduction was 2.97eV.

Brook et al.⁽³²⁾ identified aluminum interstitials as the principal ionic carriers at high P_{O_2} , with a calculated mobility of about $6 \times 10^{-4} \text{cm}^2/\text{v}\cdot\text{sec}$ at 1600°C. The dc-conductivity below 1600°C has an activation energy of 2.9eV for both doped (Ti, Mg, Co, and Si) and undoped crystals.

Kitazawa⁽³³⁾ observed a thermal activation energy of 3.47eV above 1400°C and attributed it to the electronic conductivity in the intrinsic region. Below 1400°C, the activation energy became 2.47eV and was due to extrinsic conduction (total impurity content, 100 ppm, mainly Si). The observed oxygen partial pressure dependence was similar to Pappis and Kingery's. However, below 1400°C there existed a wide intermediate P_{O_2} range where the conductivity showed no dependence on the oxygen pressure. Emf measurements showed predominantly ionic conduction in this non- P_{O_2} dependent region. Undoped, hot-pressed and MgO-doped polycrystalline samples exhibited conductivities of about two orders of magnitude larger. This was attributed to enhanced electronic conduction in the grain boundaries.

All the above works have suggested that electrical conduction is dominated by extrinsic (impurity) effects at low temperatures, that is, the presence of impurities control the

concentrations of point defects. Pollak⁽³⁴⁾ has systematically doped alumina with Fe (0.08, 0.5 and 4.4 mole%). For low iron-dopant level, the conductivity was p-type at high P_{O_2} and n-type at low P_{O_2} , similar to earlier findings. However, for high iron concentration, the effect of P_{O_2} was reversed. This peculiar response to the change in oxygen partial pressure was linked to the precipitation of a spinel phase at low P_{O_2} for the 4.4 mole% Fe- Al_2O_3 sample. The solubility limit of iron in Al_2O_3 decreased with decreasing P_{O_2} . The appearance of the spinel second phase was equivalent to reducing the Fe dopant level in the corundum matrix.

The magnitude of the conductivity measured varied from 10^{-2} to 10^{-5} (ohm·cm)⁻¹ between 1600° and 1400°C as compared to 10^{-5} to 10^{-7} (ohm·cm)⁻¹ for nominally "pure" samples. The activation energy obtained was 3.9eV of which 3.5eV was assigned to energy for defect formation. Figure 5 summarizes the results of these workers.

Dutt and Kroger⁽³⁵⁾ speculated that most Fe ions were present in corundum in the trivalent state. They derived a defect model with Fe_{Al}^{\cdot} compensating for $Al_i^{\cdot\cdot\cdot}$, suggesting that the conduction would be p-type at high P_{O_2} . They also obtained equilibrium constants for the defect reactions. However, the accuracy of their enthalpies for defect reactions remains questionable.

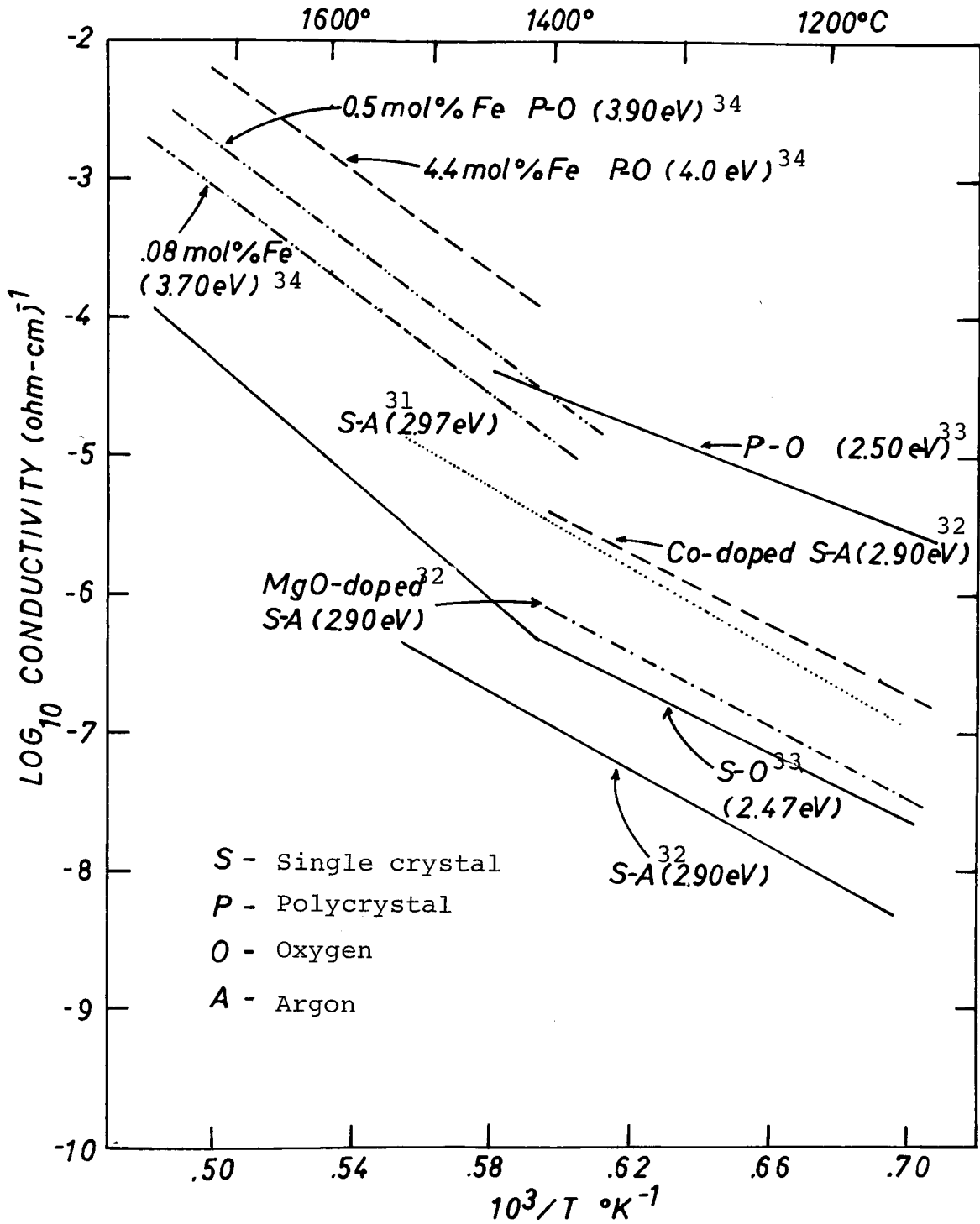


Figure 5. Electrical conductivities of doped and undoped single and polycrystalline Al₂O₃.

II.2.3. Mullite

Mullite, $3\text{Al}_2\text{O}_3 \cdot 2\text{SiO}_2$, is a crystalline silicate which belongs to the orthorhombic system. ^(36,37) The unit cell dimensions are: $a_0 = 7.583 \pm .002 \text{Å}$, $b_0 = 7.681 \pm .002 \text{Å}$ and $c_0 = 2.8854 \pm .0005 \text{Å}$. Mullite shows a wide variation in composition and is regarded as an intermediate disordered phase between sillimanite ($\text{Al}_2\text{O}_3 \cdot \text{SiO}_2$) and andalusite ($2\text{Al}_2\text{O}_3 \cdot \text{SiO}_2$).

Mullite has an open structure. It consists of chains of Al octahedra running parallel to the c-axis at the center and the four corners of the unit cell. These octahedra are cross-linked by tetrahedra containing both Al and Si ions. The Si and Al in the tetrahedra in mullite are randomly mixed, thereby making it a disordered structure. To arrive at the formula unit of 60 mole% Al_2O_3 , some of the tetrahedrally coordinated Si ions in sillimanite are replaced by Al, accompanied by a shift of some tetrahedral cations into new positions. Oxygen must also be removed to maintain electrical neutrality.

Other cations have appreciable solubility in mullite. ⁽³⁶⁾ The most notable examples are Fe and Ti. Natural iron-mullites can contain up to 6% Fe_2O_3 . The Fe cation is present mostly in the trivalent state, replacing the Al ions.

Two publications ^(38,39) discussed the coordination of the Fe^{3+} ion in mullite. Iron-doped kaolinite glasses were re-crystallized to form a mullite phase with the Mossbauer spectra indicating that the Fe^{3+} ions were in octahedral coordination. An earlier study on the change in Mossbauer spectrum during

the phase transformation from kaolinite to mullite suggested that Fe^{3+} was distributed between the tetrahedral and octahedral sites. However, other workers have indicated that the same spectrum resembled a quadrupole doublet for Fe^{3+} ions in octahedral coordination alone.

Electrical conductivity and gravimetric measurements were carried out by Sockel⁽⁴⁰⁾ in iron orthosilicate, $2\text{Fe}_{1-y}\text{O}\cdot\text{SiO}_2$ in CO/CO_2 atmospheres between 1000°C and 1150°C . The electrical conductivity was of the order of $10^{-2} - 10^{-3} \text{ ohm}^{-1}\cdot\text{cm}^{-1}$. The possible defects were discussed on the basis of the crystal structure. The dependence of both sets of measurements on $\text{P}_{\text{O}_2}^{1/6}$ was consistent with a defect model with doubly ionized iron vacancies and an equal concentration of electron holes. The difference between the enthalpies in conductivity and gravimetric results was 0.252eV and was assumed to be the activation enthalpy for motion of electron holes. The calculated mobility for electron holes was $6 \times 10^{-3} \text{ cm}^2/\text{v}\cdot\text{sec}$. All these strongly indicate a small polaron conduction mechanism.

II.3. Electrical Conductivity of Glasses and Silicate Melts

II.3.1. Semiconducting oxide glasses containing transition metal ions (TMI).

In the early 60's, a lot of enthusiasm was centered around the then "newly" discovered semi-conducting oxide glasses containing TMI (such as V, Fe, Co, Cu and Mn).

Verwey⁽⁴¹⁾ had earlier recognized the importance of the oxidation states of the TMI to the overall conductivity of semiconducting glasses. He introduced the notion of a controlled valence scheme, by adding TMI in different valence states, to fix the conductivity of semiconductors. Mackenzie⁽⁴²⁾ suggested that the electrical conductivity would also be governed by the concentration and the interatomic separation of the TMI centers.

The fact that these glasses exhibited electronic conduction was supported by the time independent dc-conductivities, by the absence of any induced emf due to ionic conduction, by the low thermal activation energies for conduction and also by the high magnitudes of the conductivities.

The activation energies for the electrical conductivity of 20BaO-60GeO₂-20V₂O₅, 31CaO-61B₂O₃-8Fe₃O₄ and 30CaO-60B₂O₃-10CoO glasses were about half those when the TMI were absent.⁽⁴³⁾ The addition of 30 mole% CoO to a CaO·B₂O₃ glass lowered the resistivity at 350°C by five orders of magnitude, to about 10⁷ ohm·cm. Also, with glass compositions of 50.8-87.5 mole% V₂O₅, 10-30 mole% P₂O₅, 2.3-20 mole% BaO and 6.5-10.8 mole% Na₂O in the V₂O₅-P₂O₅-BaO and V₂O₅-P₂O₅-BaO-Na₂O systems⁽⁴⁴⁾, the activation energies were as low as between 0.34-0.39eV.

Trap and Stevels⁽⁴⁵⁾ successfully prepared semiconducting glasses from Na₂O-CaO-SrO-Al₂O₃-SiO₂ and Na₂O-MnO-MgO-Al₂O₃-Co₃O₄-SiO₂ systems with various amounts of Fe₃O₄. The conductivity below 500°C could be as high as 10⁻²-10⁻³ ohm⁻¹·cm⁻¹

with about 15 mole% of Fe_3O_4 added. The activation energies had a distinct dependence on the $\text{Fe}^{3+}/\text{Fe}^{2+}$ ratios.

Ferric oxide is a nucleating agent to glasses in the $\text{CaO-MgO-Al}_2\text{O}_3\text{-SiO}_2$ system. (46-48) O'Horo (49) heat treated an alumino-borosilicate glass with 12 mole% Fe_2O_3 at 650°C to 800°C resulting in the precipitation of a spinel phase. Upon progressive treatment at higher temperature and for longer time periods, the conductivity underwent dramatic changes. For anneals between 650°C and 800°C the conductivity dropped with increasing annealing temperature, caused by the removal of Fe ions from the glass matrix. At the same time the activation energy increased from 0.68eV to 1.2eV. However, on further anneal at 800°C or higher, the conductivity suddenly increased by several orders of magnitude and the activation energy dropped to 0.02eV. This was attributed to the formation of a continuous spinel network in the glassy matrix.

$\text{GeO}_2\text{-P}_4\text{O}_{10}\text{-V}_2\text{O}_5$ glasses (50,51) have conductivities ranging from 2×10^{-3} to 10^{-9} $\text{ohm}^{-1}\cdot\text{cm}^{-1}$ at 25°C . Measurements up to 200°C revealed that the conductivity depended on the V_2O_5 content, and it decreased with increasing concentrations of V^{4+} ions ($\text{V}^{5+}/\text{V}^{4+} = 0.5\text{-}23.5$). For the compositions less than 10 mole% V_2O_5 , the glasses no longer exhibited any electronic conduction, probably because the VO_6 octahedra were isolated and this prohibited charge transfer between adjacent sites.

V_2O_5 -CaO- B_2O_3 and V_2O_5 -CaO- P_2O_5 glasses⁽⁵²⁾ have activation energies from 0.47 to 1.11eV. Both the enthalpy and the magnitude of the conductivity were functions of composition, V^{5+}/V^{4+} and also the network former. With the same V^{5+}/V^{4+} ratio and composition, the conductivity for the B_2O_3 glass was lower than that for the P_2O_5 system.

II.3.2. Iron and Vanadium Phosphate Glasses

Hansen⁽⁵³⁾ reported the only instance where a conductivity maximum occurred at $c = 0.5$ as predicted by Mott's model (Eq. 5) for $55(FeO+Fe_2O_3) \cdot 45P_2O_5$ glass (in mole%) at 200°C. A resistivity versus c plot went through a broad minimum between $c = 0.4$ and 0.6 . Unfortunately the variation in resistivity was 10 times higher than if it were to be controlled by the factor $c(1-c)$ alone. This suggested variations in other factors in the model. The thermal activation energies obtained from 300°-700°K ranged from 0.7eV for $55(FeO+Fe_2O_3) \cdot 45P_2O_5$ to 1.6eV for $55MgO-45P_2O_5$ composition.

The thermoelectric power for $55(FeO+Fe_2O_3) \cdot 45P_2O_5$ glass was virtually temperature independent but very sensitive to c . The conductivity changed from p-type to n-type at $c = 0.38$, in contradiction to the conductivity maximum occurring at $c = 0.5$.

The difficulty encountered in fitting the data with Mott's model was well demonstrated by Vaughan and Kinser.⁽⁵⁴⁾ The conductivity maxima for $x(FeO+Fe_2O_3) \cdot (100-x)P_2O_5$ samples of x up to 75 mole% did not in general occur at $c = 0.5$,

except for the special case where $x = 55$. The maximum shifted to higher c with increasing iron content. Phase separation was discovered for glasses containing more than 60 mole% $(\text{FeO} + \text{Fe}_2\text{O}_3)$. Magnetic coupling between Fe^{2+} ions and the segregation of Fe^{2+} in the second phase were suggested as possible causes for the difficulty in the data analysis.

The mechanical loss,⁽⁵⁵⁾ modulus relaxation and the ac dispersion⁽⁵⁶⁾ between 10^2 and 10^5 cps for the $55(\text{FeO} + \text{Fe}_2\text{O}_3) \cdot 45\text{P}_2\text{O}_5$ glass were attributed to the induced resonance of electron hopping between the Fe^{2+} and Fe^{3+} sites because the temperature dependence of these processes was equivalent to the activation enthalpy for the dc conduction process. However, Kinser⁽⁵⁷⁾ disagreed and noted a change in conductivity upon thermal treatment and the concomitant appearances of dielectric losses with observed devitrification under electron microscopy. He suggested that the dispersions were of the Maxwell-Wagner type from a highly conducting dispersed phase.

Dozier et al.⁽⁵⁸⁾ saw similar changes of conductivity on annealing. Whether the conductivity increased or decreased depended on both the original $\text{Fe}^{3+}/\text{Fe}_{\text{tot}}$ value and the time of anneal. This reflected the effect of the removal of Fe^{3+} and Fe^{2+} ions from the matrix, due to devitrification, on conductivity.

Schmid⁽⁵⁹⁾ extended Holstein's⁽³⁾ treatment of small polarons and discussed the validity of small polarons as the carriers in TMI glasses. In particular, he chose to study phosphate glasses containing various amounts of V_2O_5 . The activation energies ranged from 0.4-1.0eV for high temperature (below 300°K) and 0-0.2eV for below 100°K. The conductivity did not show a clear-cut dependence on the amount of V_2O_5 , but on the importance of the V^{5+}/V^{4+} ratio.

Contrary to the iron phosphate glasses, the Seebeck coefficient in $V_2O_5-P_2O_5$, $V_2O_5-CaO-P_2O_5$ and $V_2O_5-CaO-B_2O_3$ glasses⁽⁶⁰⁾ changed sign at $c = 0.5$. On the other hand, Linsley's⁽⁶¹⁾ work on a series of $V_2O_5-P_2O_5$ glasses indicated that the conductivity maxima occurred at c values of 0.8-0.9. Munakata⁽⁶²⁾ also reported similar results for 60 V_2O_5 -5BaO-35 P_2O_5 and 60 V_2O_5 -20BaO-20 P_2O_5 glasses where the conductivity maxima occurred between c values of 0.8-0.85. Linsley also observed a linear relationship between the $(1-c)$ term at the conductivity maximum and the P_2O_5 content. The results of these studies are presented in Figure 6. Also included are Hansen and Vaghan et al's data for iron phosphate glass.

So, in vanadium phosphate glasses the conductivity results are inconsistent with Mott's model. While Linsley was unable to rationalize the conductivity results with the hopping model, he attributed this to the complexity in the glass structure. A fraction, θ , of the V^{5+} sites were assumed to be rendered inactive such that the $c(1-c)$ term became

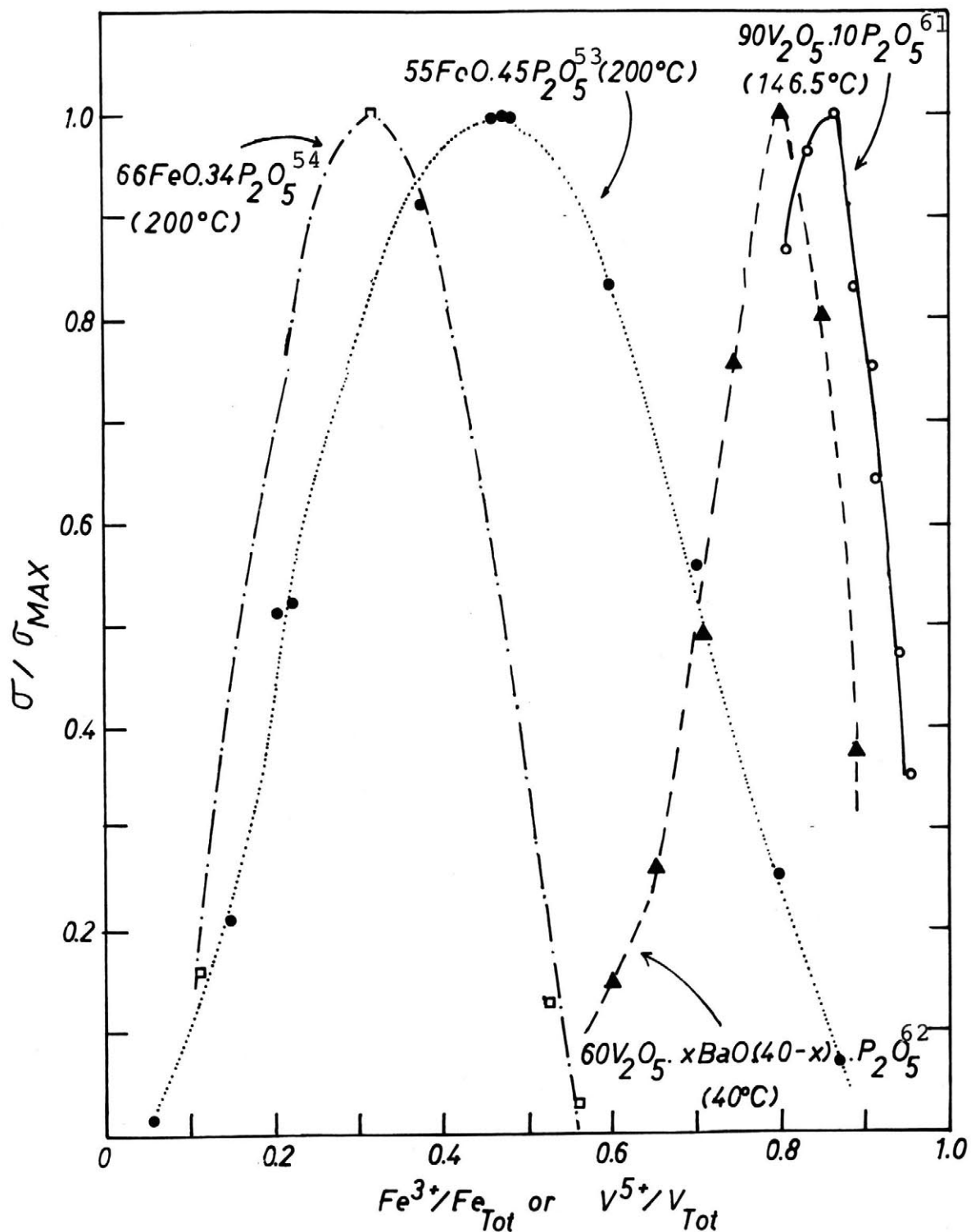


Figure 6. Normalized conductivity for phosphate glasses as a function of the oxidation state of the TMI.

$(c-\theta)(1-c)$. This was unreasonable for the values of θ calculated (0.63-0.78) because the conductivity would become negative at sufficiently low values of c . Another plausible explanation was the active participation of a fraction of V^{5+} ions in the formation of polymeric network and thus, were screened from any V^{4+} ions.

II.3.3. Silicate Melts.

Very few experimental data have been compiled for silicate melts containing FeO , Fe_2O_3 or Al_2O_3 . Most of the early work has been concentrated on the conductivities of binary systems. These were ionic in nature. It was later observed that the electrolysis of melts containing iron oxide provided evidence of electronic contribution to the conductivity. Recently research on the conductivity of ferrous slags has been related to MHD activities.

Bockris^(63,64) measured the conductivity of silicate melts containing CaO , MnO or Al_2O_3 over the temperature range of $1000^\circ-1800^\circ C$. The Arrhenius relationship, $\sigma = A \exp(-E/kT)$, was obeyed for all three oxides. In the $Al_2O_3-SiO_2$ system with 0.03-0.12 mole fraction alumina, the conductivity was of the order $10^{-3}-10^{-4} \text{ ohm}^{-1} \cdot \text{cm}^{-1}$ at $1600^\circ-1700^\circ C$ (as compared to $10-10^{-1} \text{ ohm}^{-1} \cdot \text{cm}^{-1}$ for $CaO-SiO_2$ and $MnO-SiO_2$ systems) and was independent of the oxygen partial pressure. Under isothermal conditions, a conductivity maximum occurred at 0.05 mole fraction Al_2O_3 . The terms E and A were dependent

on the composition and varied from 0.559-1.07eV and 0.1-0.2 respectively. The low conductivity of the $\text{Al}_2\text{O}_3\text{-SiO}_2$ system and the increased viscosity of the melt were evidence that the aluminum and silicon ions were associated with network tetrahedra.

In a 38 w/o CaO 20w/o Al_2O_3 42w/o SiO_2 melt,⁽⁶⁵⁾ the Al tracer diffusivity was $1.6 \times 10^{-6} \text{ cm}^2/\text{sec}$ at 1450°C . Those for Ca and Si were $4 \times 10^{-6} \text{ cm}^2/\text{sec}$ and $2 \times 10^{-6} \text{ cm}^2/\text{sec}$ respectively. Since the density of a slag of composition 10.04w/o CaO 15.06w/o Al_2O_3 1.2w/o CrO_2 4.8w/o Nb_2O_5 9.7w/o V_2O_5 13.5w/o TiO_2 20.7w/o CaF_2 25w/o SiO_2 is 2.88 gm/cm^3 at 1650°C ,⁽⁶⁶⁾ the density of the above CaO- $\text{Al}_2\text{O}_3\text{-SiO}_2$ melt is assumed to be 3.0 gm/cm^3 . Using the Nernst-Einstein equation, the ionic conductivities calculated for the Ca, Al, and Si ions are $2.11 \times 10^{-1} \text{ ohm}^{-1} \cdot \text{cm}^{-1}$, $1.01 \times 10^{-1} \text{ ohm}^{-1} \cdot \text{cm}^{-1}$ and $4.35 \times 10^{-1} \text{ ohm}^{-1} \cdot \text{cm}^{-1}$ respectively. Comparing the calculated value for Ca ions with the measured conductivity of $1 \cdot 10^{-1} \text{ ohm}^{-1} \cdot \text{cm}^{-1}$ for the CaO- SiO_2 system shows that most of Ca ions contribute to the conduction process. However, the low conductivity ($10^{-3} - 10^{-4} \text{ ohm}^{-1} \cdot \text{cm}^{-1}$) of the $\text{Al}_2\text{O}_3\text{-SiO}_2$ system suggests that a large fraction of Al ions are covalently bonded to anion complexes in the melt and are not available as free charge carriers.

The ternary system CaO- $\text{Al}_2\text{O}_3\text{-SiO}_2$ was studied by Martin and Derge.⁽⁶⁷⁾ The conductivity was measured under a nitrogen atmosphere for compositions 35.1-50.1% SiO_2 , 35.1-50.05%CaO

and 5.0-19.7% Al_2O_3 between 1400-1620°C. The conductivity at 1600°C was of the order of $0.25\text{-}0.8 \text{ ohm}^{-1}\cdot\text{cm}^{-1}$, close to the values for CaO-SiO_2 .

In a short note, Tomlinson and Inouye⁽⁶⁸⁾ asserted that the conductivity of liquid iron oxide contained in an iron crucible was above $150 \text{ ohm}^{-1}\cdot\text{cm}^{-1}$ above 1400°C. In later work⁽⁶⁹⁾ they measured the p-type conduction in wustite melts with iron electrodes in a nitrogen atmosphere. Addition of 5 mole% of Al_2O_3 reduced the conductivity from $324 \text{ ohm}^{-1}\cdot\text{cm}^{-1}$ to $227 \text{ ohm}^{-1}\cdot\text{cm}^{-1}$ at 1500°C. SiO_2 had a still larger effect, dropping the conductivity to $164 \text{ ohm}^{-1}\cdot\text{cm}^{-1}$ with a 5.4 mole% addition. Their data on iron oxide melts were over an order of magnitude higher than those of Fisher and Vom Ende⁽⁷⁰⁾. The conductivities of FeO-SiO_2 are plotted in Figure 7 together with those of $\text{Al}_2\text{O}_3\text{-SiO}_2$ and CaO-SiO_2 .

The weight loss by an iron anode during the electrolysis of iron-silicate melt gave a measurement of the anode current efficiency, $C_+(\%)$, based on a two-electron charge in the oxidation of metallic iron anode.

$$C_+(\%) = \frac{100\Delta w}{27.93 n} \quad (11)$$

where Δw is the loss in anode mass, n is the number of Faradays passed and 27.93 is the gram-equivalent of iron. Simnad et al⁽⁷¹⁾ reported that the current efficiency stayed between 8-12% for compositions below 10wt% SiO_2 , then it increased

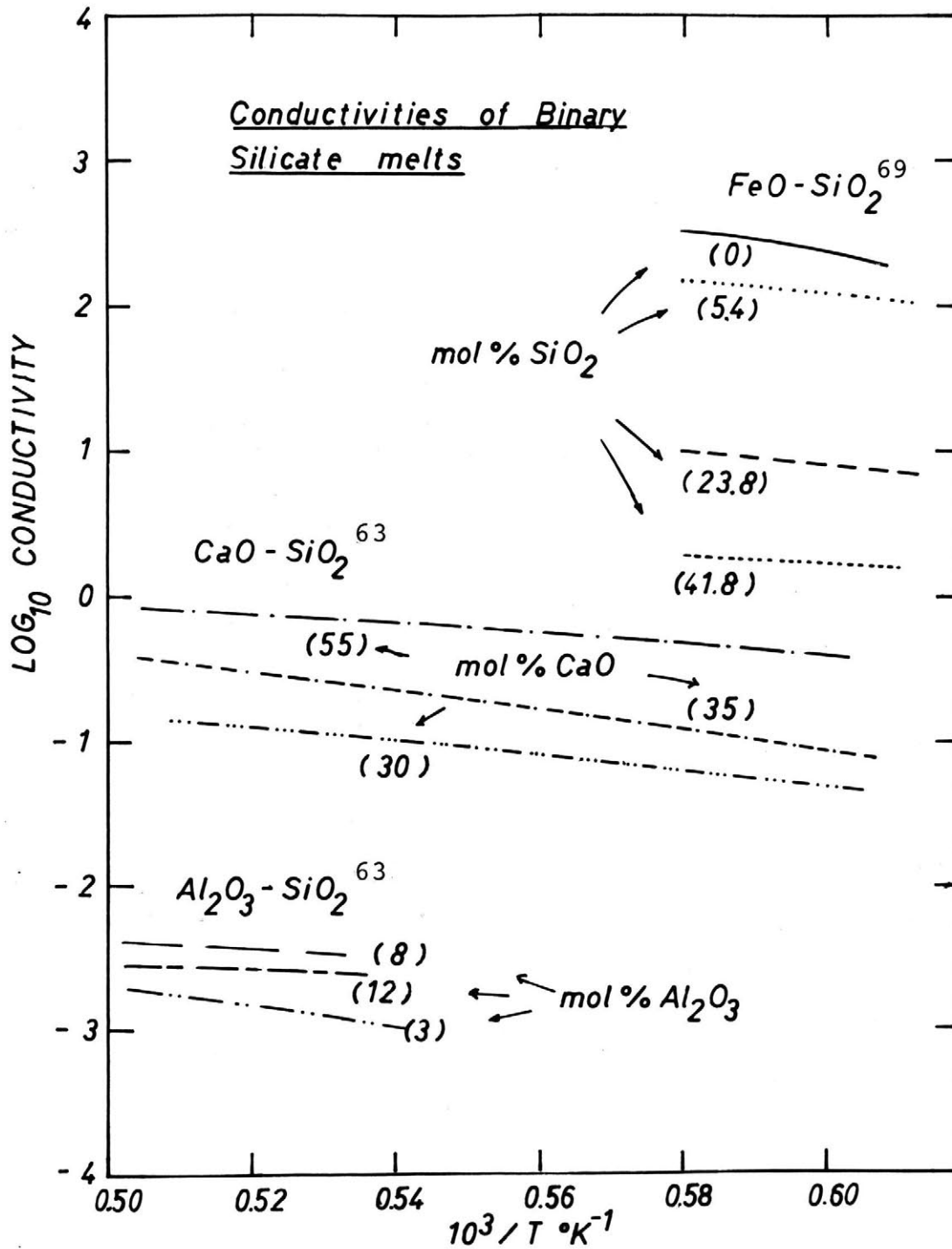


Figure 7. Electrical conductivity of binary silicate systems: FeO-SiO₂, CaO-SiO₂ and Al₂O₃-SiO₂.

linearly with the addition of SiO_2 to about 90% for 34wt% SiO_2 . The temperature effect was negligible from 1200°-1400°C. Gaseous oxygen was evolved at the anode, an indication that the anodic oxidation of silicate ions occurred. Otherwise the bulk of the ionic current was carried by ferrous ions.

P-type conduction was observed for the FeO-MnO-SiO_2 system⁽⁷²⁾ in argon. The behavior was more complex; the addition of MnO might or might not affect the current efficiency, depending on the amount of SiO_2 . On the other hand, addition of SiO_2 naturally increased it. The interpretation was further obscured by the fact that not only charge transfer between Fe^{2+} and Fe^{3+} but also between Mn^{2+} and Mn^{3+} contributed to electronic conductivity.

Both calcium and iron ions were ionic carriers in FeO-CaO-SiO_2 melts^(73,74) under argon. The transference number calculated for calcium ion showed that an unusually high fraction of the ionic current was carried by this ion. This supported the prevailing view that the ferrous ions were associated with the silicate anion complexes, giving low activities of FeO in iron silicate melts. The anode current efficiencies of FeO-SiO_2 , FeO-CaO-SiO_2 and FeO-MnO-SiO_2 are included in Figure 8 for comparison.

Recently there have been numerous publications in the Russian literature on the electrical conductivity of silicate melts as a function of oxygen partial pressure. Both $\text{FeO-Fe}_2\text{O}_3\text{-SiO}_2$ ⁽⁷⁵⁾ and $\text{FeO-Fe}_2\text{O}_3\text{-CaO-Al}_2\text{O}_3\text{-SiO}_2$ ⁽⁷⁶⁾ exhibited

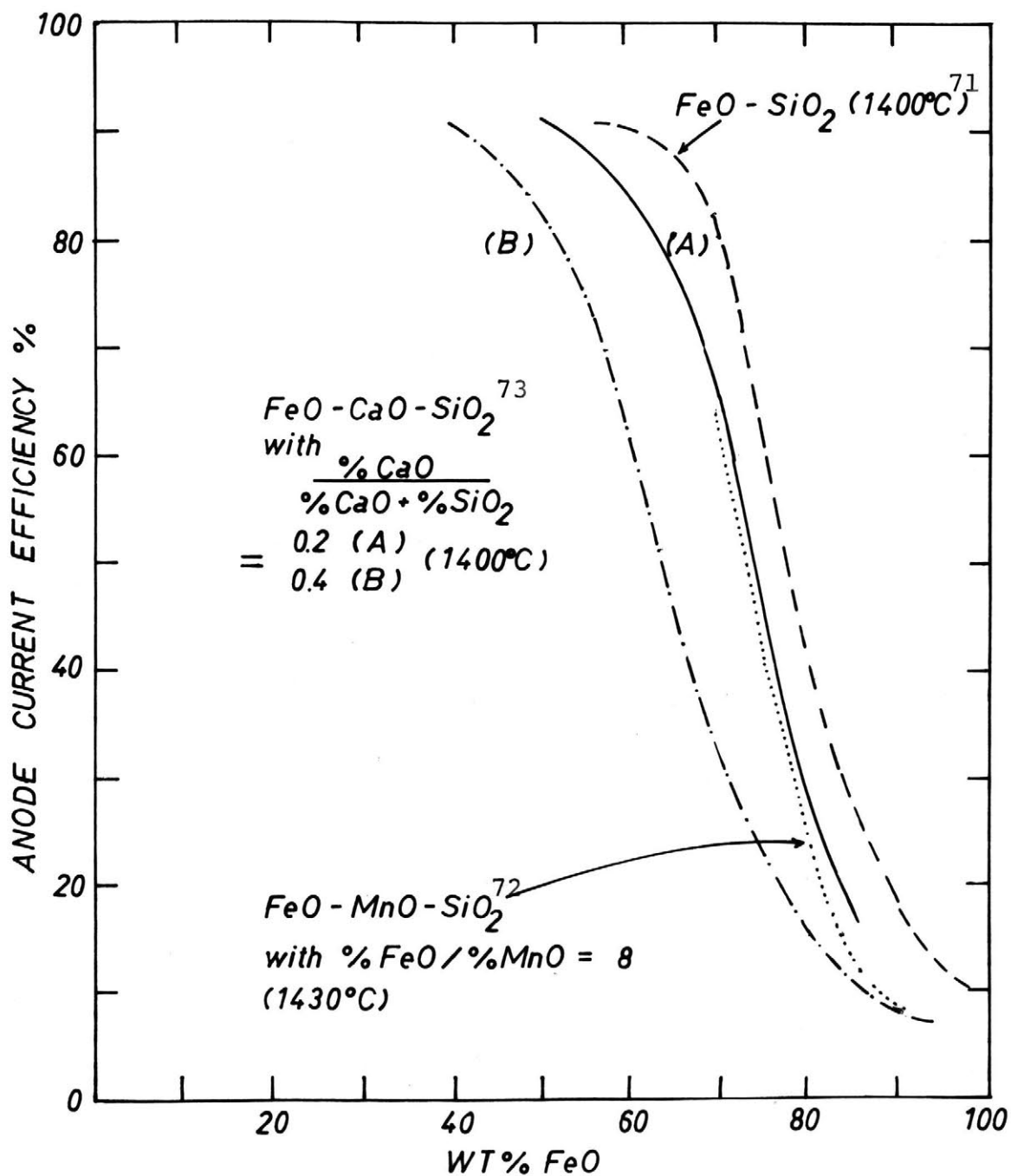


Figure 8. Anode current efficiency measured in the electrolysis of iron oxide-containing silicate melts.

limited dependence of conductivity on the oxygen partial pressure. For the FeO-Fe₂O₃-SiO₂ melts with greater than 34% SiO₂, the conductivities were virtually independent of oxygen pressure (10⁻¹-10⁻¹² atm). For compositions with above 66% (FeO+Fe₂O₃), the conductivities decreased with decreasing P_{O2} at 10⁻⁸-10⁻¹¹ atmospheres. For CaO-Al₂O₃ containing melts, the conductivity was 1-2 orders of magnitude lower. In all cases, the conductivity was independent of frequency (10²-10⁴ Hz). Their data interpretation was based on the erroneous assumption that only the electronic conductivity was a function of P_{O2}. This could not be true in the iron-silicates. The oxygen partial pressure controls the Fe³⁺/Fe²⁺ ratio and affected their respective contribution to ionic conduction.

Engell and Vygen⁽⁷⁷⁾ studied the conductivity of FeO-Fe₂O₃-CaO-SiO₂ melts. They chose compositions with a n_{CaO}/n_{SiO₂} ratio of 0.79 because the Fe³⁺/Fe²⁺ was a function only of P_{O2} and not the overall composition. Ac-conductivity was measured at 30KHz. The conductivity results were modelled for contributions from ionic and electronic carriers.

$$\sigma_{\text{total}} = \sigma_o - a'c + b'c(1-c) \quad (12)$$

$$c = \text{Fe}^{3+} / \text{Fe}_{\text{total}}$$

where σ_o was the ionic conductivity due to Ca²⁺ and Fe²⁺ ions in a FeO-CaO-SiO₂ melts when c = 0. The term a'c was the ionic part that was subtracted from the conductivity to account for

the difference in the mobilities of Fe^{2+} and Fe^{3+} and the increased concentration of Fe^{3+} ions.

The $b'(1-c)$ term was discussed in two limiting cases. The first was electron hopping by Mott's model. Engell and Vygen also considered a collision-dependent, bimolecular reaction which allowed for diffusional relaxation after charge transfer. In this context, an activated complex of Fe^{2+} and Fe^{3+} ions was necessary for charge transfer.

Figure 9 shows the dependence of the electrical conductivity on the oxygen partial pressure for a number of silicate melts. N_{Fe} is defined as

$$N_{\text{Fe}} = \frac{n_{\text{FeO}} + 2n_{\text{Fe}_2\text{O}_3}}{N_{\text{FeO}} + 2n_{\text{Fe}_2\text{O}_3} + n_{\text{CaO}} + n_{\text{SiO}_2}} \quad (13)$$

All of the melts exhibit only very limited response to the change in the oxygen partial pressure.

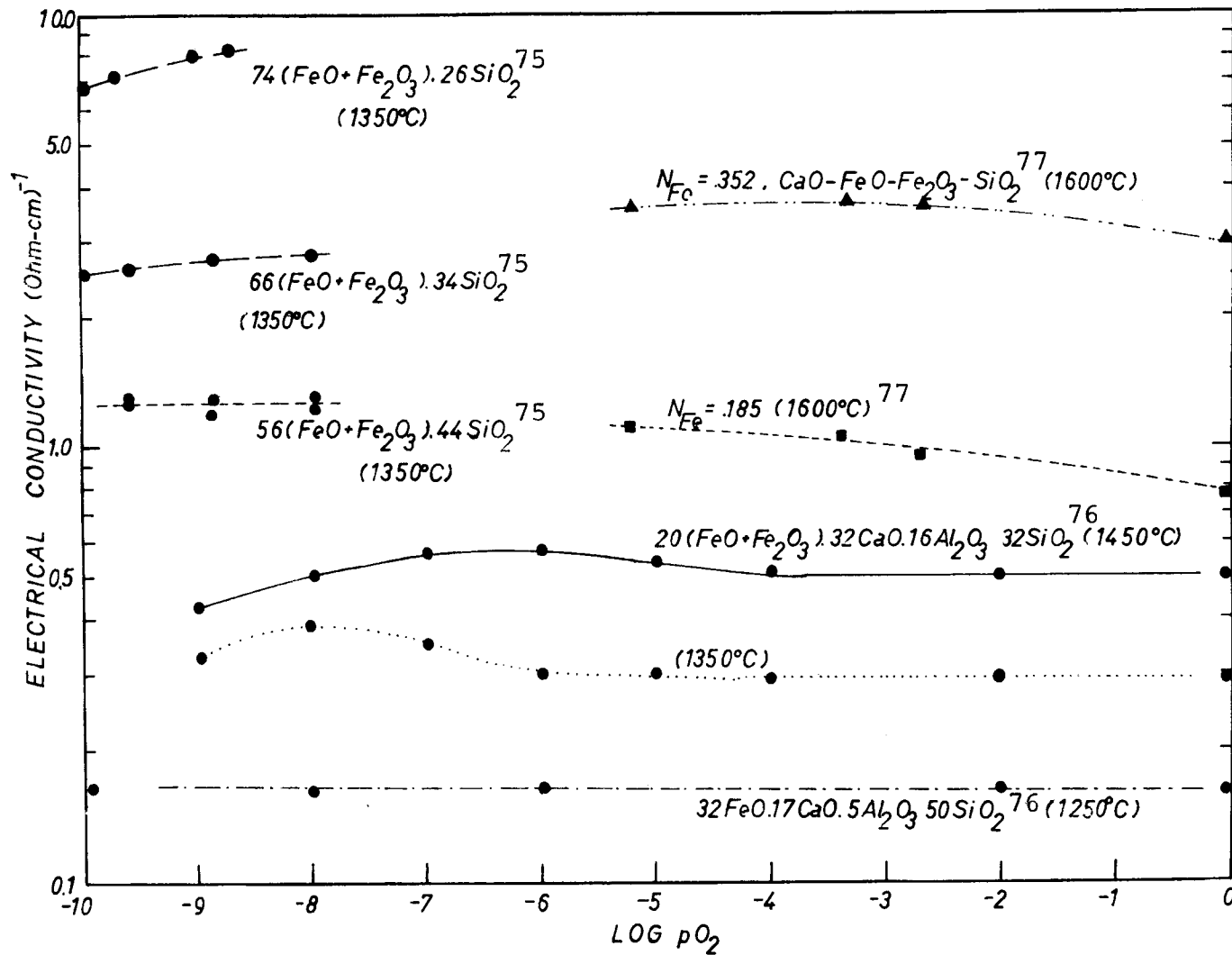


Figure 9. Electrical conductivity of iron-oxide-containing melts as a function of oxygen partial pressure.

Chapter III. Ionic Activities in Silicate Melts-A

Thermodynamic Approach to the $\text{FeO}\cdot\text{Fe}_2\text{O}_3\text{-Al}_2\text{O}_3\text{-SiO}_2$ System.

The ionic constitution of liquid silicates has been the subject of recent research studies. To the metallurgist, an understanding of the silicate systems is crucial and provides important data for controlling slag reactions. This is, in itself, of obvious value in industrial applications. To others, the complex silicate melts pose an attractive yet puzzling class of systems that demands theoretical modelling.

There are very few experiments that can provide direct confirmation about the structure of silicate melts. It used to be common practice to study the density, viscosity, diffusivity and thermodynamic activities so that inference could be made on the ionic arrangement. But these only give indirect information about ionic distributions and interactions. Only recently⁽⁷⁸⁻⁸⁰⁾ have experimental techniques been developed, for example, the trimethylsilyl derivatives of the silicate anions have been isolated, identified and their ionic distributions determined.

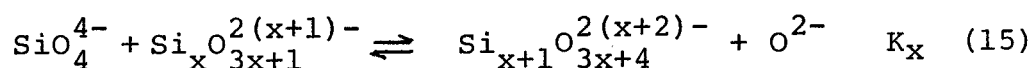
Parallel to these developments, there have also been significant advances in the modelling of these complex systems. Common basic oxides in slags such as FeO, MnO, CaO, MgO and PbO are expected to ionize and give free cations and oxygen anions which may or may not be bonded to the silicon ion. Silicate anions exist as the monomer SiO_4^{4-} , the dimer

$\text{Si}_2\text{O}_7^{6-}$, the trimer $\text{Si}_3\text{O}_{10}^{8-}$, and so on.

Flood⁽⁸¹⁾ and Richardson⁽⁸²⁾ were the first ones to describe the silicate melt by an equilibrium distribution of silicate ions. Toop and Samis^(83,84) chose to represent the polymerization in slags by a simple equilibrium reaction (equilibrium constant K) between oxygen ions doubly bonded (O°), singly bonded (O^-) to silicon ions and other free oxygen ions, (O^{2-})



Masson⁽⁸⁵⁻⁸⁷⁾ decided that it was inadequate to consider the equilibrium reaction without considering the silicate anions. Hence he selected polycondensation reactions of the following type,



He assumed that ring structures were non-existent in the melt so that all silicate anions were in linear chain configuration with K_x being the same for all x. This was because, in the polymerization reaction, the free energy of breaking a double oxygen bond in a linear chain would be the same no matter how large the anion was. The value of K_x would be characteristic of each MO-SiO_2 system. K_x for FeO-SiO_2 was 1.0 at 1600°C and 0.7 at 1300°C. These were computed by fitting the measured thermodynamic activities with the

model, which also predicted that the SiO_4^{4-} monomer was the most abundant species in FeO-SiO_2 melts at all compositions.

Unfortunately this model has only been successfully applied to binary systems of the type MO-SiO_2 . So it should be noted that while the FeO-SiO_2 system has been well documented, little is known about the ionic structure in $\text{FeO-Fe}_2\text{O}_3\text{-SiO}_2$, let alone that in the $\text{FeO}\cdot\text{Fe}_2\text{O}_3\text{-Al}_2\text{O}_3\text{-SiO}_2$ system.

The sections following present a simple thermodynamic approach in calculating the activities of the $\text{FeO}\cdot\text{Fe}_2\text{O}_3\text{-Al}_2\text{O}_3\text{-SiO}_2$ system, leading to the justification of the choice of the alumina crucible as the conductivity cell.

III.1. Thermodynamic Activities in the $\text{FeO}\cdot\text{Fe}_2\text{O}_3\text{-Al}_2\text{O}_3\text{-SiO}_2$ System.

The thermodynamic activities of FeO , Fe_2O_3 and SiO_2 in the $\text{FeO-Fe}_2\text{O}_3\text{-SiO}_2$ system have been experimentally determined by Schuhmann and Ensio⁽⁸⁸⁾ and Schuhmann and Michal.⁽⁸⁹⁾ A premixed CO/CO_2 gas was bubbled through the melt contained in either a silica or γ -iron crucible. When equilibrium was reached between the gas and the melt, the melt was chemically analyzed.

The Gibbs-Duhem integration of the activity terms was simplified as the activity of one component was fixed (SiO_2 or Fe). The activity of another component could be expressed in terms of the oxygen potential. For a silica saturated melt, the Gibbs-Duhem integration became

$$\log a_{\text{FeO}} = -\frac{1}{2} \int \frac{N_{\text{Fe}^{3+}}}{N_{\text{Fe}_{\text{total}}}} d \log (P_{\text{CO}_2}/P_{\text{CO}}) \quad (16)$$

Similar equations were obtained for melts under different equilibrium conditions. Turkdogan⁽⁹⁰⁾ gathered the data available and calculated the iso-activity curves for FeO, Fe₂O₃ and SiO₂ in the melt at 1550°C.

Lumsden⁽⁹¹⁾ claimed that the activities of the system could be represented with a simple regular solution model. The ionic species he chose were FeO, FeO_{1.5} and SiO₂.

The following is a simple regular solution approach to see if it can successfully fit the experimentally measured activities of the FeO-Fe₂O₃-SiO₂ system.

For the reaction,



$$K = \frac{\gamma_3 N_3}{\gamma_2^2 N_2^2 P_{\text{O}_2}^{1/2}}$$

N₂, N₃ are mole fractions for FeO and Fe₂O₃, γ₂, γ₃ are activity coefficients. For a regular solution model with interaction parameter, α,

$$RT \ln \gamma_2 = \alpha N_3^2 \quad (18a)$$

$$RT \ln \gamma_3 = \alpha N_2^2 \quad (18b)$$

substituting

$$\ln K = \ln \frac{N_3}{N_2^2 P_{O_2}^{1/2}} - \frac{\alpha}{RT} (2N_3^2 - N_2^2) \quad (19)$$

A plot of $\ln (N_3/N_2^2 P_{O_2}^{1/2})$ versus $(2N_3^2 - N_2^2)$ at constant temperature should give $\ln K$ as the intercept and α/RT as the slope. The data of Darken and Gurry⁽⁹²⁾ for liquid iron oxide at different partial pressure oxygen at 1600°C were used. Figure 10 shows that the regular solution model is indeed applicable over the range for $(2N_3^2 - N_2^2)$ below -0.5. Above this range, the increased concentration of Fe^{3+} ions causes a deviation from linearity. The failure at high Fe^{3+} concentration is understandable because Fe^{3+} can have either octahedral or tetrahedral coordination. Fe^{2+} ions have octahedral coordination only. This contradicts the basic assumption in the regular solution model that the coordination number be the same. The interaction parameter calculated from the slope is -1082 as compared to -4460 for $FeO-Fe_{1.5}$.

Application of the regular solution model to a ternary system gives,

$$RT \ln \gamma_1 = -\alpha_3 N_2 N_3 + (N_2 + N_3) (\alpha_1 N_2 + \alpha_2 N_3) \quad (20)$$

where the α 's are the interaction parameters for the binaries.

So for the $FeO-Fe_2O_3-SiO_2$ system,

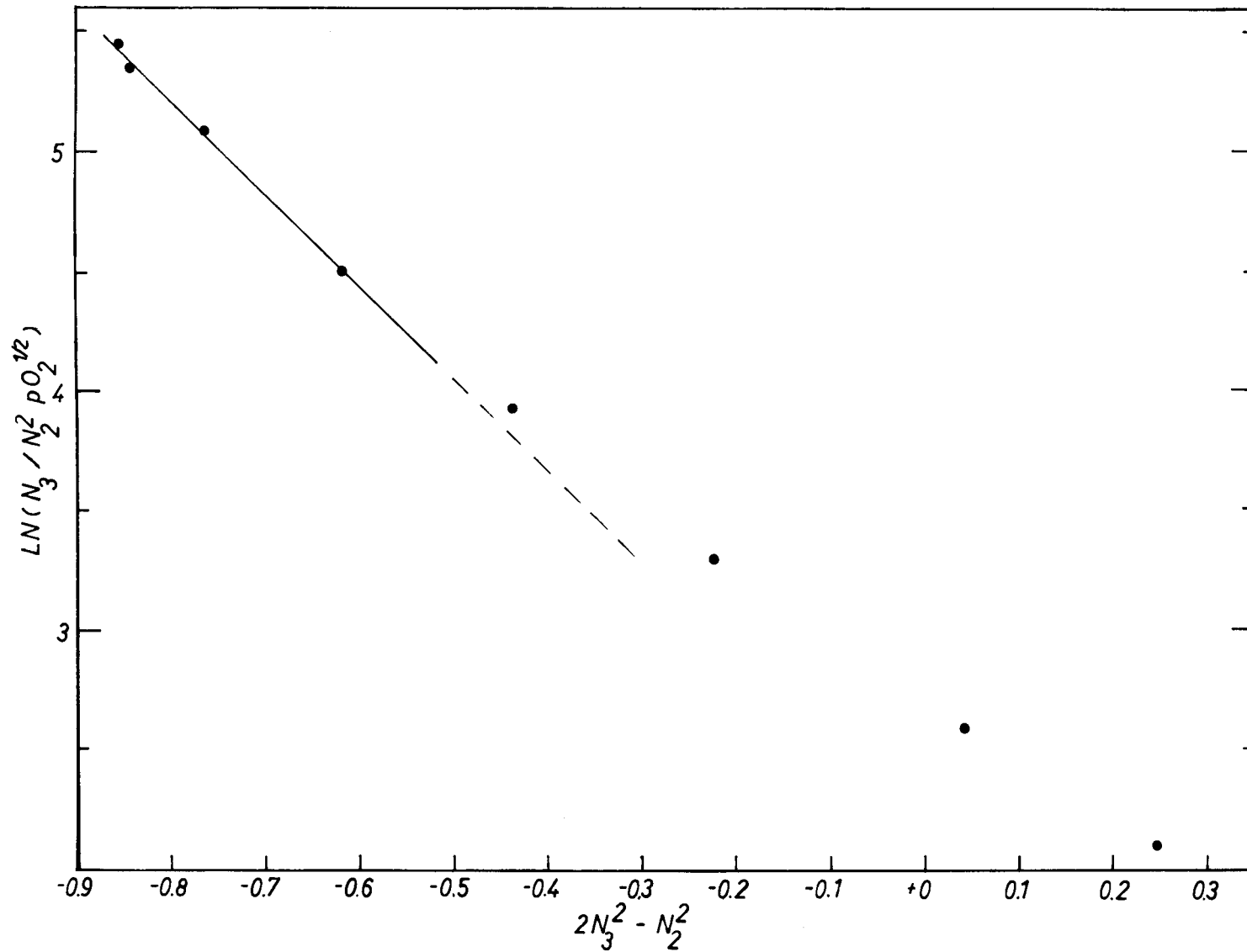


Figure 10. Application of the regular solution model to liquid iron oxide melt at 1600°C.

$$\begin{aligned}
RT(\ln\gamma_3 - 2\ln\gamma_2) &= RT\ln K + 2RT\ln N_2 + 1/2 RT\ln P_{O_2} \\
&\quad - RT\ln N_3 \\
&= -\alpha_2 (N_2 N_{SiO_2} + 2N_{SiO_2} N_3 + 2N_{SiO_2}^2) \\
&\quad + \alpha_3 (N_2 N_{SiO_2} + 2N_{SiO_2} N_3 + N_{SiO_2}^2) \\
&\quad + \alpha_1 (N_2^2 + N_{SiO_2} N_2 - 2N_{SiO_2} N_3 - 2N_3^2) \quad (21)
\end{aligned}$$

Using Turkdogan and Bills's^(93,94) equilibrium compositions, the unknowns in the above equation, K , α_2 and α_3 (with α_1 being -1082), can be calculated by taking sets of equilibrium composition data and solving three simultaneous linear equations. The compositions chosen were those at low P_{O_2} , with low Fe^{3+} concentration. Still α_2 and α_3 do not converge to any reasonable and consistent values.

Turkdogan and Bills^(93,94) had also compiled the equilibrium compositions of the $FeO-Fe_2O_3-SiO_2$ system at 1550°C at different P_{O_2} . Their data are recalculated and presented as the Fe^{3+}/Fe^{2+} ratio as a function of P_{O_2} at constant silica content (Figures 11, 12 and 13).

Figure 14 gives the approximate location in air of the fractionation curves in the spinel and corundum phase fields of the $FeO \cdot Fe_2O_3-Al_2O_3-SiO_2$ system, as given by Muan.⁽²⁵⁾ These curves were constructed from the conjugation lines.*

* A conjugation line joins the composition of the melt with the equilibrium composition of the coexisting crystalline phase. It is a tangent to the fractionation curve.

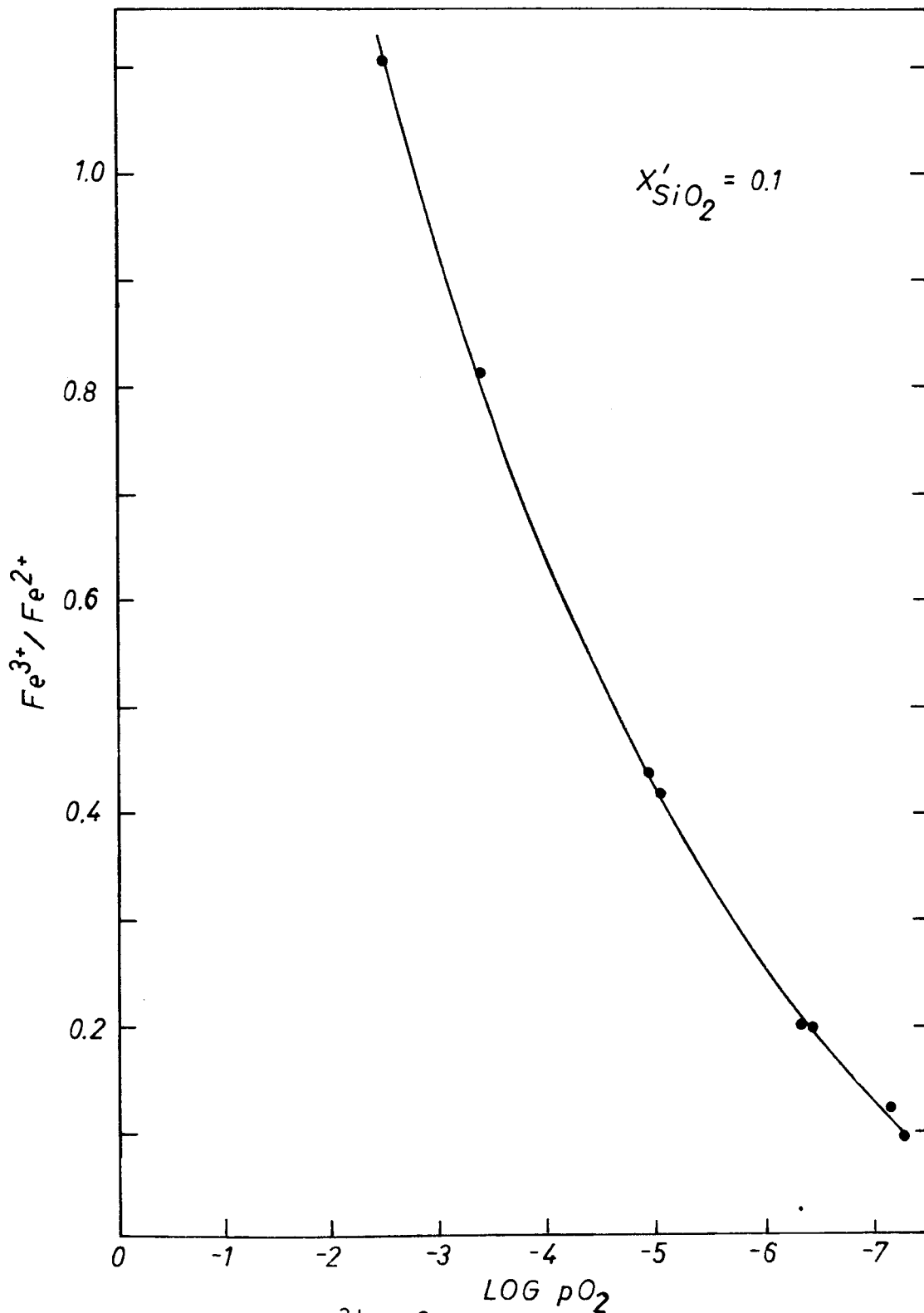


Figure 11. The Fe^{3+}/Fe^{2+} ratio in iron silicate melt (at $1550^{\circ}C$, $x_{SiO_2} = 0.1$) as a function of oxygen partial pressure.

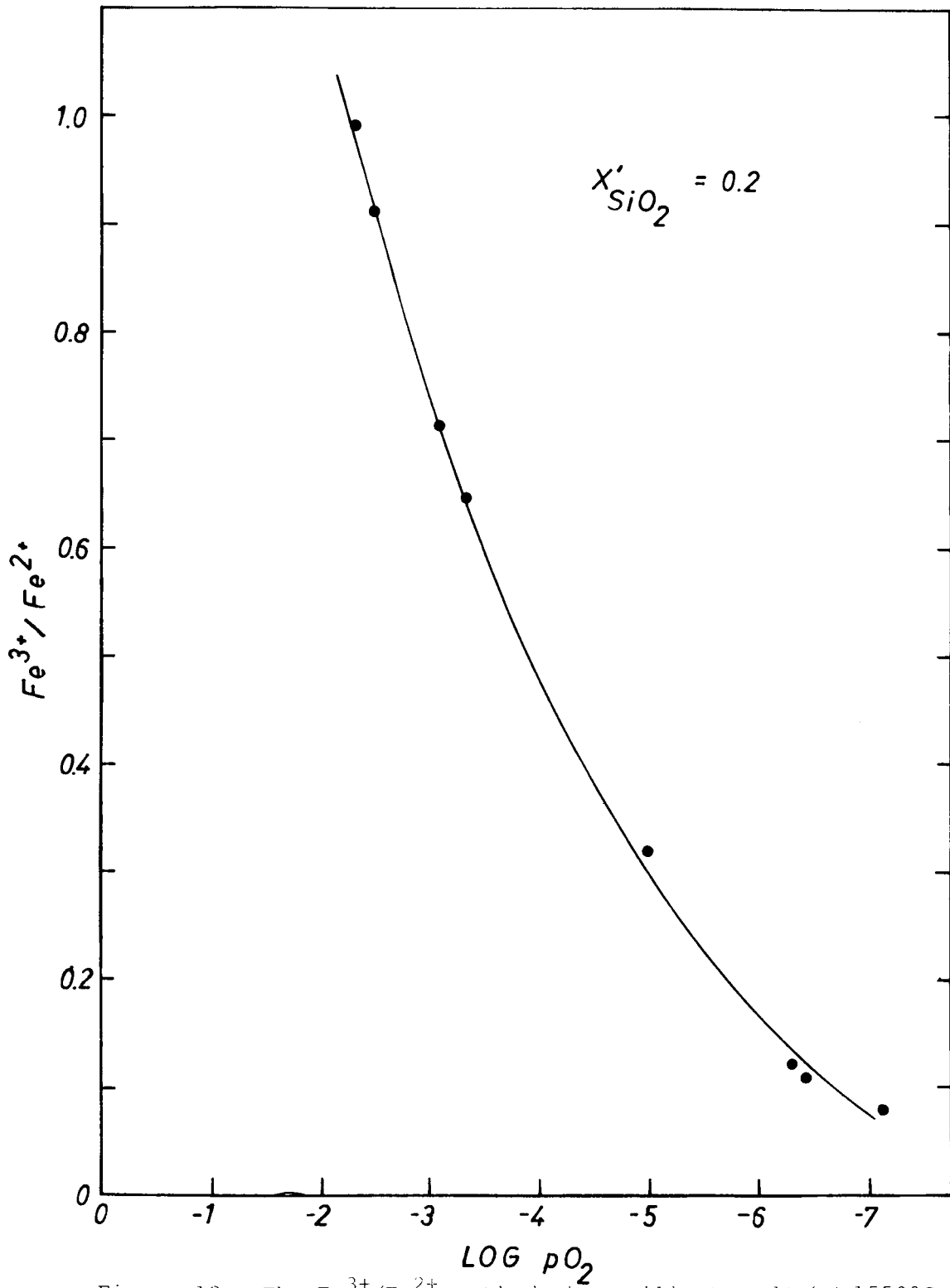


Figure 12. The Fe^{3+}/Fe^{2+} ratio in iron silicate melt (at 1550°C, $x_{SiO_2} = 0.2$) as a function of oxygen partial pressure.

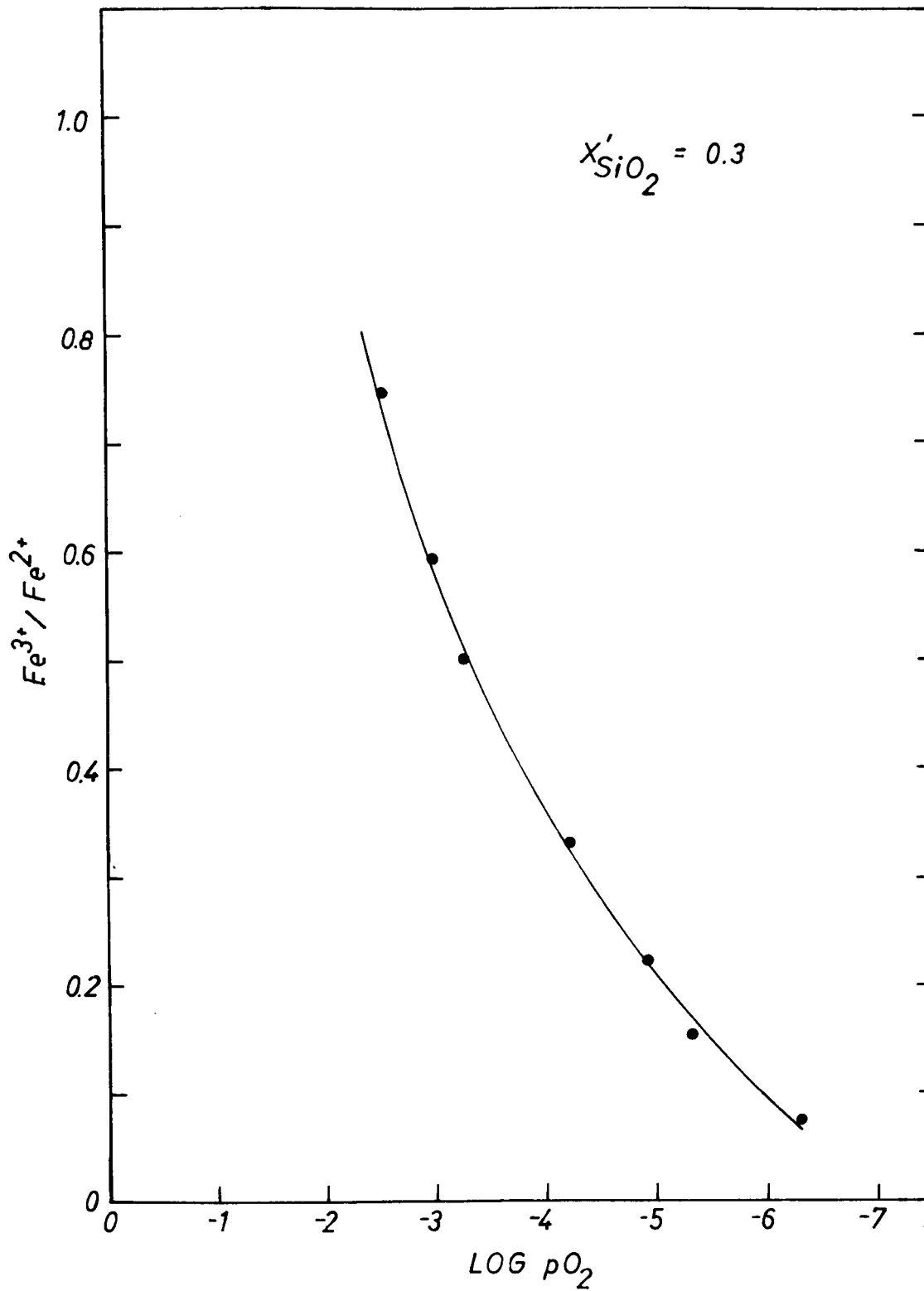


Figure 13. The Fe^{3+}/Fe^{2+} ratio in iron silicate melt (at 1550°C, $x'_{SiO_2} = 0.3$) as a function of oxygen partial pressure.

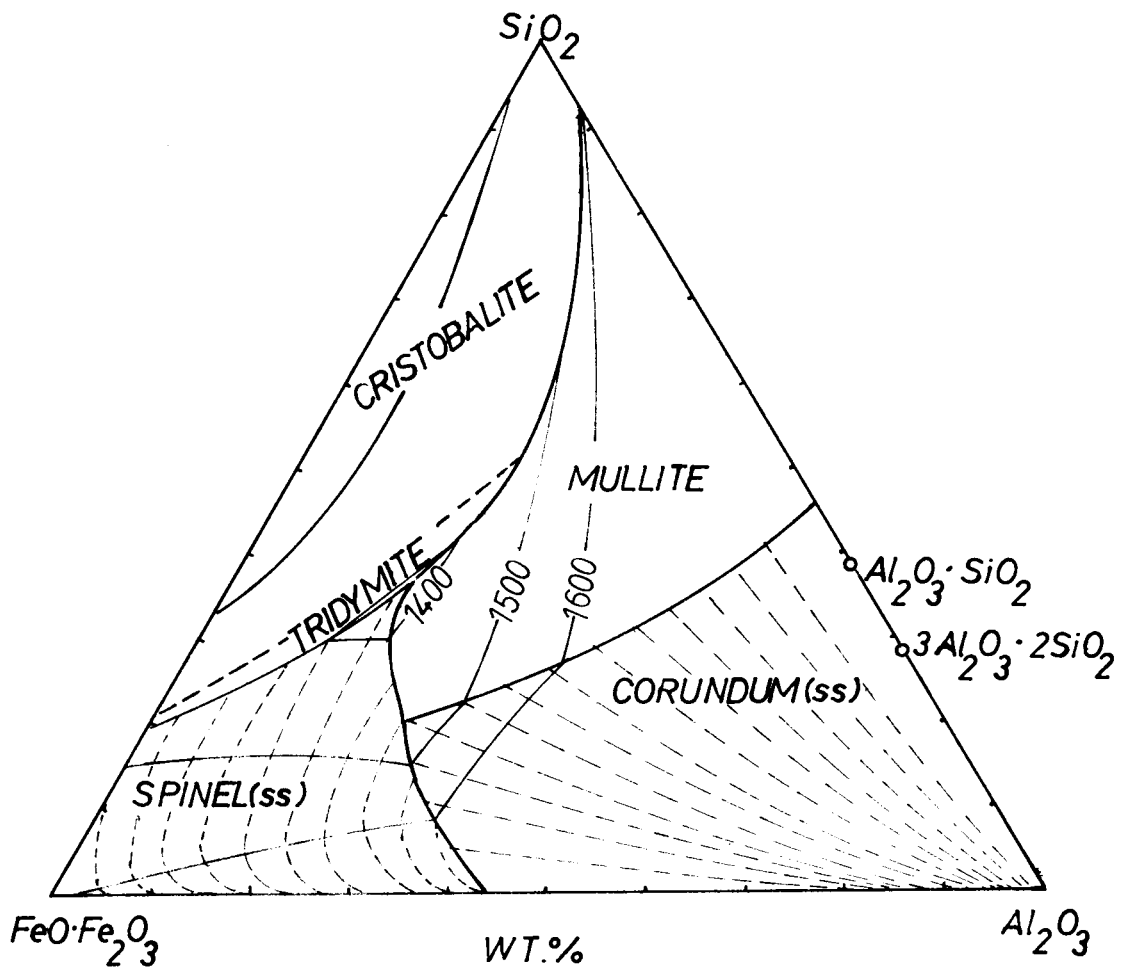


Figure 14. Fractionation curves in the $\text{FeO}\cdot\text{Fe}_2\text{O}_3\text{-Al}_2\text{O}_3\text{-SiO}_2$ system, after Muan. (25)

They are instrumental in the calculation of the thermodynamic activities of the system. It is acknowledged that it is difficult to specify the ionic species in the melt. But certain assumptions must be made to express the melt constitution in some convenient form. As short range order is expected to be retained in the melt, the activities of the system are expressed in terms of the FeO , Fe_2O_3 , Al_2O_3 and SiO_2 species.

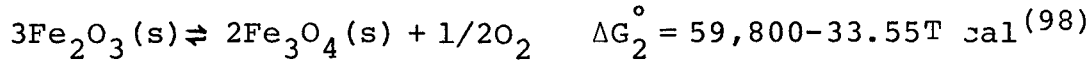
The standard states referenced are the forms which are stable at the equilibrium temperature and P_{O_2} conditions. They are liquid wustite, hematite(s), magnetite(s), alumina(s) and silica(s) for the calculations here.

The activities of the end members Fe_3O_4 and FeAl_2O_4 in iron aluminum spinel have been calculated from the solvus at 700°C .⁽⁹⁵⁾ Alcock's⁽⁹⁶⁾ experimental results suggest an ideal behavior of the end members at 1300°C . Mason⁽⁹⁷⁾ has used the generalized Clasius -Clapeyron equation to develop a cation (Fe^{2+} , Fe^{3+} and Al^{3+}) mixing scheme on octahedral and tetrahedral sites for an iron aluminum spinel $x\text{Fe}_3\text{O}_4 \cdot (1-x)\text{FeAl}_2\text{O}_4$. He showed that the Fe_3O_4 and FeAl_2O_4 activities were complicated, yet very close to composition linearity ($a = x$). Thus the activities FeO , Fe_2O_3 and Al_2O_3 in a $x\text{Fe}_3\text{O}_4 \cdot (1-x)\text{FeAl}_2\text{O}_4$ spinel can be calculated as follows.

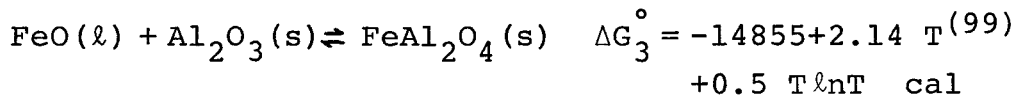
From the reactions,



$$K_1 = a_{\text{Fe}_3\text{O}_4} / a_{\text{FeO}}^3 P_{\text{O}_2}^{1/2} \quad (22)$$



$$K_2 = a_{\text{Fe}_3\text{O}_4}^2 P_{\text{O}_2}^{1/2} / a_{\text{Fe}_2\text{O}_3}^3 \quad (23)$$



$$K_3 = a_{\text{FeAl}_2\text{O}_4} / a_{\text{FeO}} a_{\text{Al}_2\text{O}_3} \quad (24)$$

one obtains,

$$a_{\text{FeO}} = 3 \sqrt{K_1 P_{\text{O}_2}^{-1/2} x_{\text{Fe}_3\text{O}_4}}$$

$$a_{\text{Fe}_2\text{O}_3} = 3 \sqrt{P_{\text{O}_2}^{1/2} K_2^{-1} x_{\text{Fe}_3\text{O}_4}^2}$$

$$a_{\text{Al}_2\text{O}_3} = \frac{(1 - x_{\text{Fe}_3\text{O}_4})}{K_3 a_{\text{FeO}}}$$

In the spinel primary phase field where the iron aluminum spinel is in equilibrium with the melt,

$$\begin{array}{ccc} \text{melt} & & \text{spinel} \\ \mu_{\text{FeO}} & = & \mu_{\text{FeO}} \end{array}$$

$$\begin{array}{ccc} \text{melt} & & \text{spinel} \\ \mu_{\text{Fe}_2\text{O}_3} & = & \mu_{\text{Fe}_2\text{O}_3} \end{array}$$

$$\begin{array}{ccc} \text{melt} & & \text{spinel} \\ \mu_{\text{Al}_2\text{O}_3} & = & \mu_{\text{Al}_2\text{O}_3} \end{array}$$

Figures 15, 16 and 17 are the isothermal activities versus mole fraction plots for Fe_2O_3 , FeO and Al_2O_3 . Several observations can be made. FeO deviates negatively whereas Fe_2O_3 positively from Raoultian behavior, just as in the case of $\text{FeO-Fe}_2\text{O}_3\text{-SiO}_2$. They both tend towards ideal behavior at higher temperatures according to the sign of the partial molar heat of solution. The silica content also decreases towards higher temperature, x_{SiO_2} varies from 0.245 to 0.261 at 1500°C and from 0.09 to 0.162 at 1575°C . Also included in Figures 15 and 16 are the curves A and B. Curve A corresponds to the activities in iron silicates at 1550°C and $x_{\text{SiO}_2} = 0.4$. Curve B is for the $\text{FeO-Fe}_2\text{O}_3\text{-CaO}$ system also at 1550°C and $x_{\text{CaO}} = 0.4$. The FeO activities suggest that the interactions of divalent iron cations and silicate anions are less in the iron aluminosilicates than in the iron silicates.

Along each isothermal activity curve, the amount of Al_2O_3 in the melt varies from $x_{\text{Al}_2\text{O}_3} = 0.05$ to as high as 0.3. The silica content decreases only slightly towards higher x_{FeO} and $x_{\text{Fe}_2\text{O}_3}$. The large variations of Al_2O_3 content seem to have minimal effect on the activities of FeO and Fe_2O_3 . It is interesting to note that, as illustrated in Figure 17, Al_2O_3 obeys Henry's law for dilute solutions. The isothermal activity coefficients are 3.048 (at 1600°C), 3.431 (at 1550°C) and 4.109 (at 1500°C). In the following section, the effect of additions of Al_2O_3 on the $\text{Fe}^{3+}/\text{Fe}^{2+}$

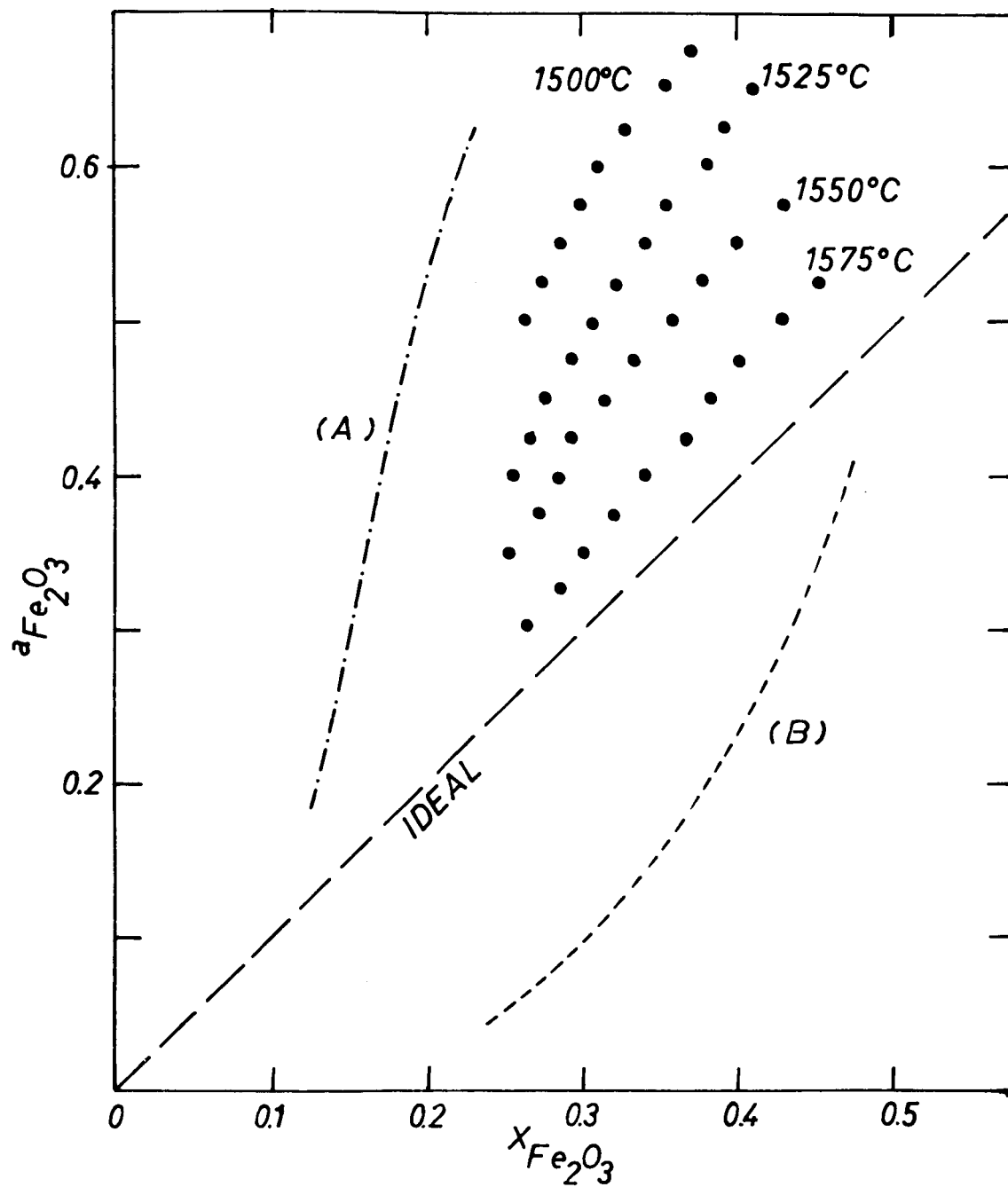


Figure 15. Isothermal activities of Fe_2O_3 in iron aluminosilicate melt.

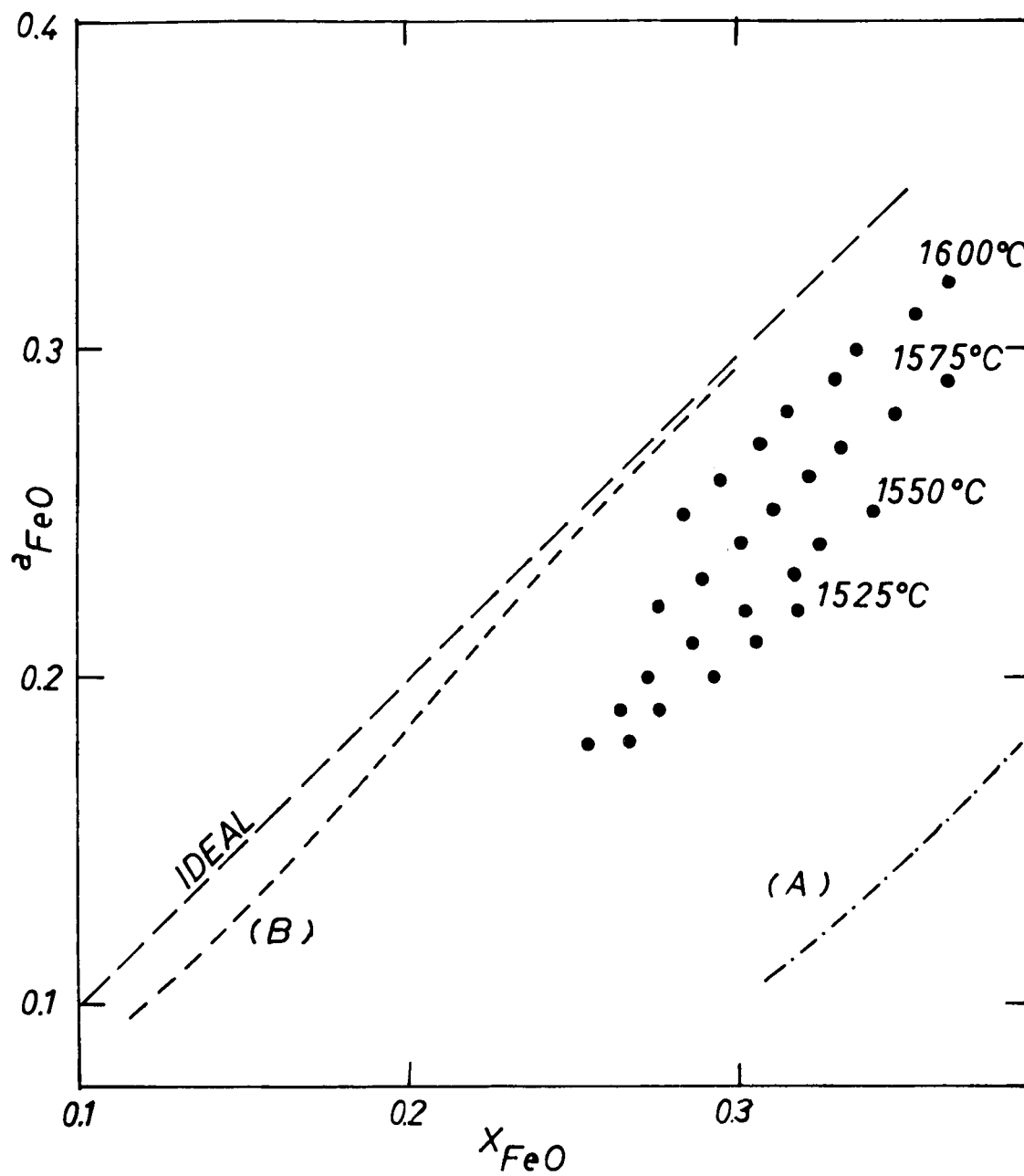


Figure 16. Isothermal activities of FeO in iron aluminosilicate melt.

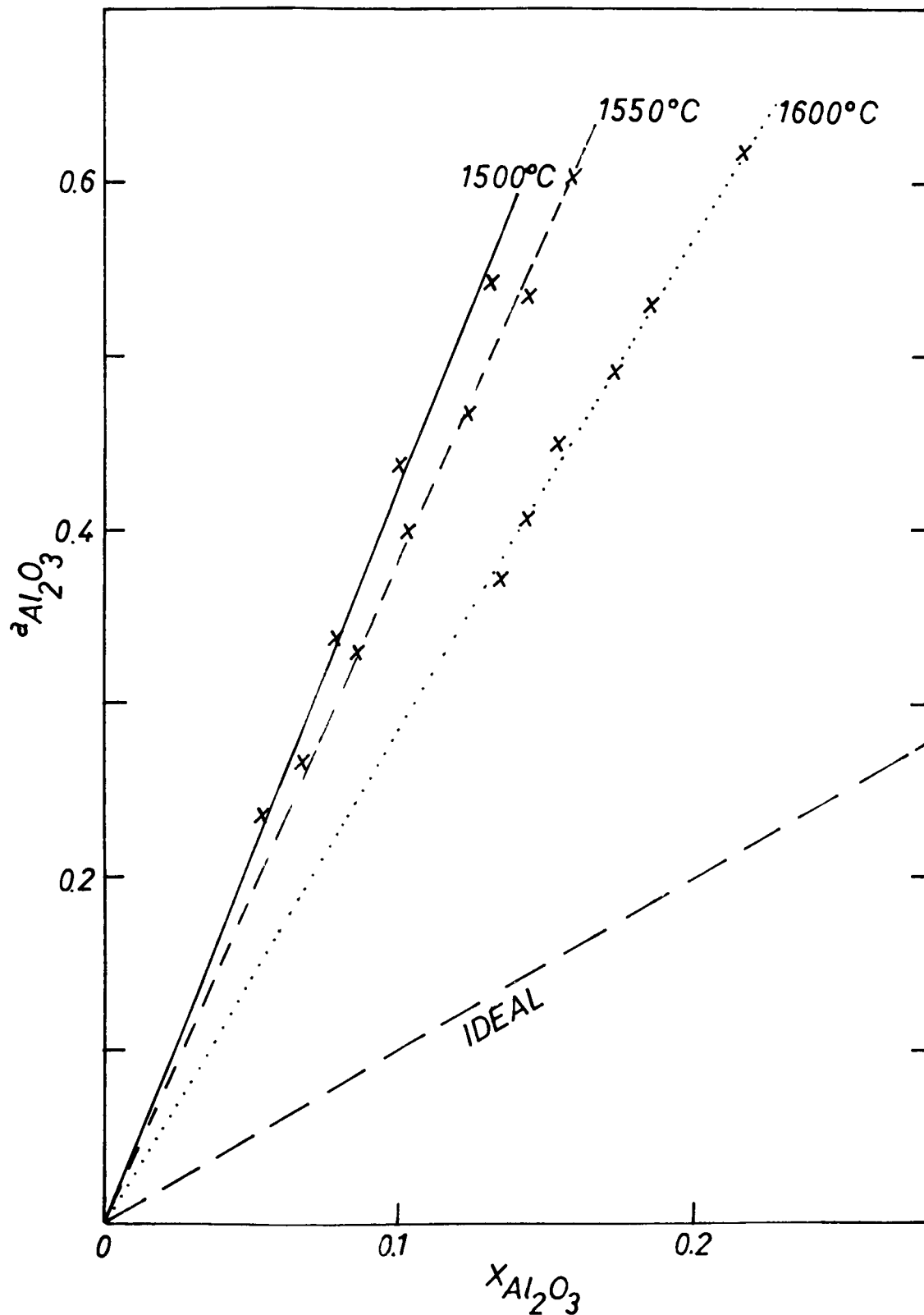


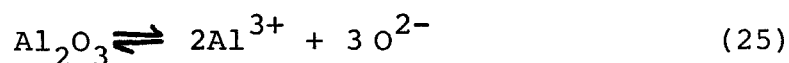
Figure 17. Isothermal activities of Al₂O₃ in iron aluminosilicate melt.

equilibrium in iron aluminosilicate is discussed.

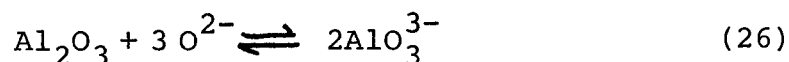
III.2. Justification for Using an Alumina Crucible as the Conductivity Cell.

At first glance the use of an alumina container for the silica melt at high temperatures seem to be a poor choice, especially for compositions with high iron content. In the spinel primary phase field, the melt is unsaturated with Al_2O_3 leading to the dissolution of the crucible and changing the overall composition of the melt. However, the following facts help affirm that the choice is legitimate.

Al_2O_3 acts as an amphoteric oxide and can be ionized as either



or



Larson and Chipman⁽¹⁰⁰⁾ discovered that Al_2O_3 was neutral to an iron oxide melt and addition of up to 8 mole% Al_2O_3 at 1550°C and $P_{\text{O}_2} = 9.968 \times 10^{-6}$ atm did not affect the $\text{Fe}^{3+}/\text{Fe}^{2+}$ ratio in the melt. Muan⁽²⁵⁾ in his phase equilibria study also noted that Al_2O_3 has very little effect on the $\text{Fe}^{3+}/\text{Fe}^{2+}$ ratio in $\text{FeO}\cdot\text{Fe}_2\text{O}_3\text{-Al}_2\text{O}_3\text{-SiO}_2$ melts. In addition a number of workers^(101,102) have studied the oxidation state of iron in $\text{Na}_2\text{O}\cdot\text{SiO}_2$ melts with very low iron content. Johnston⁽¹⁰¹⁾ used an alumina crucible to hold the glassy

melt. He reported the excessive dissolution of the crucible induced a contamination of 30 wt% Al_2O_3 in the melt composition at 1450°C . Even this, he said, did not affect the nature of the $\text{Fe}^{3+}/\text{Fe}^{2+}$ oxidation-reduction equilibrium. The slope of $\log (\text{Fe}^{3+}/\text{Fe}^{2+})$ versus $\log P_{\text{O}_2}$ remained constant.

Because of the Henrian behavior of Al_2O_3 in the melt and the interesting phenomena stated above, the $\text{Fe}^{3+}/\text{Fe}^{2+}$ ratios in iron aluminosilicates obtained by Muan⁽²⁵⁾ are re-analyzed. A new parameter x'_{SiO_2} is defined,

$$x'_{\text{SiO}_2} = \frac{x_{\text{SiO}_2}}{x_{\text{FeO}} + x_{\text{Fe}_2\text{O}_3} + x_{\text{SiO}_2}} \quad (27)$$

For iron silicates,

$$x'_{\text{SiO}_2} = x_{\text{SiO}_2}$$

Figure 18 is a plot of $\text{Fe}^{3+}/\text{Fe}^{2+}$ as a function of x'_{SiO_2} for both iron aluminosilicate and iron silicate at different temperatures and P_{O_2} . The solid symbols represent the independent data for iron silicates from White⁽¹⁰³⁾, Turkdogan and Bills⁽⁹³⁾ and Larson and Chipman⁽¹⁰⁰⁾. The open symbols are the reanalyzed data in the spinel primary phase field of $\text{FeO}\cdot\text{Fe}_2\text{O}_3\text{-Al}_2\text{O}_3\text{-SiO}_2$.

From the agreement between the different sets of data, the $\text{Fe}^{3+}/\text{Fe}^{2+}$ ratio in $\text{FeO}\cdot\text{Fe}_2\text{O}_3\text{-Al}_2\text{O}_3\text{-SiO}_2$ melt can be represented by that in iron silicate under the same equilibrium

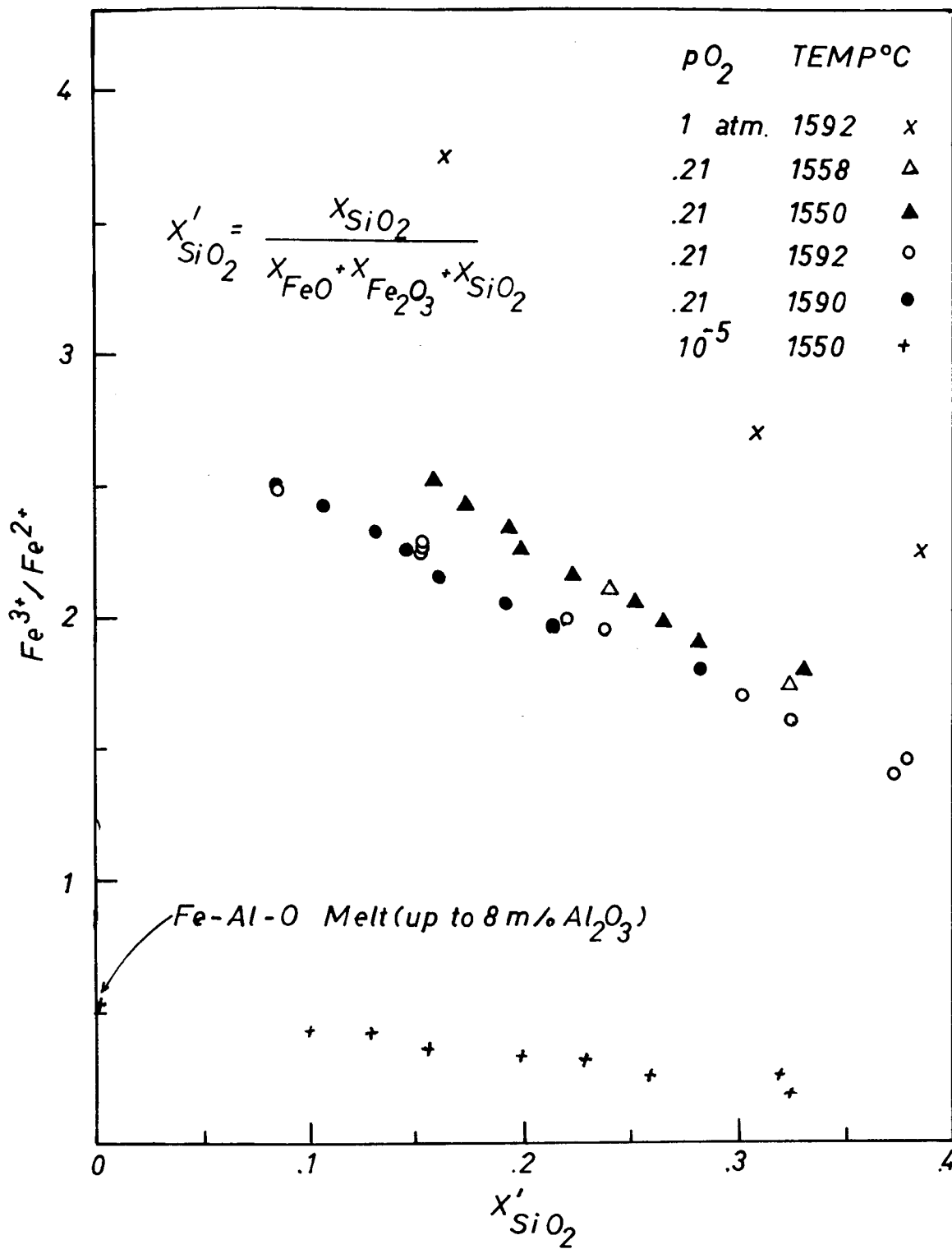


Figure 18. Comparison of Fe^{3+}/Fe^{2+} ratios in $FeO-Fe_2O_3-SiO_2$ and $FeO-Fe_2O_3-Al_2O_3-SiO_2$ systems.

conditions. The typical $\text{Fe}^{3+}/\text{Fe}^{2+}$ versus P_{O_2} at constant x_{SiO_2} curves (Figures 11-13) are useful in predicting the $\text{Fe}^{3+}/\text{Fe}^{2+}$ equilibrium.

Unfortunately, the Al_2O_3 behavior is fortuitous, it is yet to be associated with its solution thermodynamics in the melt. Nevertheless, despite the complexity of the system, it is shown that the thermodynamic activities of the oxide species can be determined from the phase equilibria data.

To make sure that the dissolution of the alumina crucible did not affect the overall composition of the melt drastically, a sample composition of $73\text{Fe}_3\text{O}_4-20\text{Al}_2\text{O}_3-7\text{SiO}_2$ (a sample with the highest iron content in this study) was melted and held at 1600°C for 15 hours. Chemical analysis* showed that the $\text{Fe}/(\text{Fe}+\text{Al})$ ratio changed from 0.689 to 0.640, an increase in about 5.2 wt% Al_2O_3 in the composition.

* Analysis done by Arnold Greene Testing Lab., Inc.
Natick, Mass. 01760.

Chapter IV. Research Objectives

The aim of this study was to determine the electrical conductivities in the $\text{FeO}\cdot\text{Fe}_2\text{O}_3\text{-Al}_2\text{O}_3\text{-SiO}_2$ system, with low silica content, in the solid and molten states. To achieve this goal, the following tasks were proposed:

1. To characterize the electrical conductivity in air as a function of composition and of temperature.
2. To measure the ac- and dc-conductivities to identify the electronic and ionic contribution to total conductivity.
3. To measure the dependence of electrical conductivity on oxygen partial pressure and compare the results with those of other silicate systems.
4. To determine the correlation between the conductivity and the phase equilibria of the system.
5. To identify the conduction mechanism in iron alumino-silicate melt and to interpret the conductivity results in the solid state in terms of multiphase conduction.

Chapter V. Experimental Procedures

This chapter deals with the different facets involved in the collection of experimental data. First, the method of sample preparation is discussed. Following is the description of the conductivity cell design and the actual experimental setup for measurement. A precise control of the oxygen partial pressure is also crucial to the accuracy of the work. Towards the end of this chapter, the techniques used to gather supportive evidence for the interpretation of the results is documented.

V.1.1. Sample Preparation

The objective was to prepare homogeneous batches of powder compositions in a convenient way without introducing excessive contamination. Originally, homogeneity was achieved by melting and remelting weighed portions of $\text{FeO}\cdot\text{Fe}_2\text{O}_3$, Al_2O_3 and SiO_2 powders in a platinum crucible. Unfortunately, this method was tedious and expensive. The following method proved to be much superior.

150-200 gm batches of powder mixtures were processed at one time. The starting materials used were $\text{FeO}\cdot\text{Fe}_2\text{O}_3$ (Fisher Scientific Company, purified grade), Al_2O_3 (Alcoa XA-139, super ground, 99.95% purity, Table I) and SiO_2 (Research Organic/Inorganic Chemical Corp, 0325 mesh, 99.89% purity). Exact proportions of these powders were weighed out

TABLE I

XA-139 high purity Al_2O_3 is a fine crystalline (less than $1\ \mu\text{m}$) Al_2O_3 . The following are typical values for lots that have been analyzed.

	<u>wt%</u>
SiO_2	.015
Fe_2O_3	.007-.011
TiO_2	.001
Na_2O	.005-.01
CaO	.006
Ga_2O_3	.003
B_2O_3	.001
MnO	.0006
Cr_2O_3	.0002
MgO	.002
ZnO	.0005
CuO	.0005
V_2O_5	.0001
Al_2O_3	99.95+

on a Mettler balance, put into a 32 oz. plastic bottle and tumbled overnight. The powder mixture was then pressed into pellets $1-1\frac{1}{2}$ " long using a $\frac{7}{8}$ " diameter steel die. They were sintered in a bottom loading type furnace with silicon carbide heating elements, built specifically for this purpose. The sintering temperature was usually 1200°C. The sintered pellets were then pulverized on a steel plate and ball-milled with $\frac{3}{4}$ "-5/16" diameter steel balls. The resulting fine powder was sieved and repressed into pellets. The above process was repeated two to three times to assure homogeneity.

Eight of the mixtures were analyzed wet chemically. The chemical analysis results were in wt% Fe, Al and Si. The corresponding wt% Fe_3O_4 , Al_2O_3 and SiO_2 were calculated and compared with the original composition in Table II. The generally lower silica content in the final powder was because, in the tumbling of the original mixture, the silica powder tends to adhere to the bottle. The pick up of iron during the ball-milling seemed to be negligible. These results showed that the method could produce fine homogenized powders with final compositions close to the original, as-mixed values.

V.1.2. Conductivity Cell:-Design and Calibration

The conductivity cell consisted of a 5 c.c. alumina crucible, a tube, a crucible cover and two platinum electrodes. A typical sample cell design is shown in Figure 19. A platinum crucible could not be used because the melt was

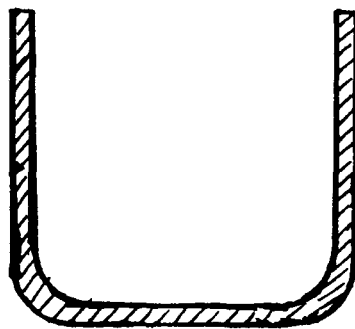
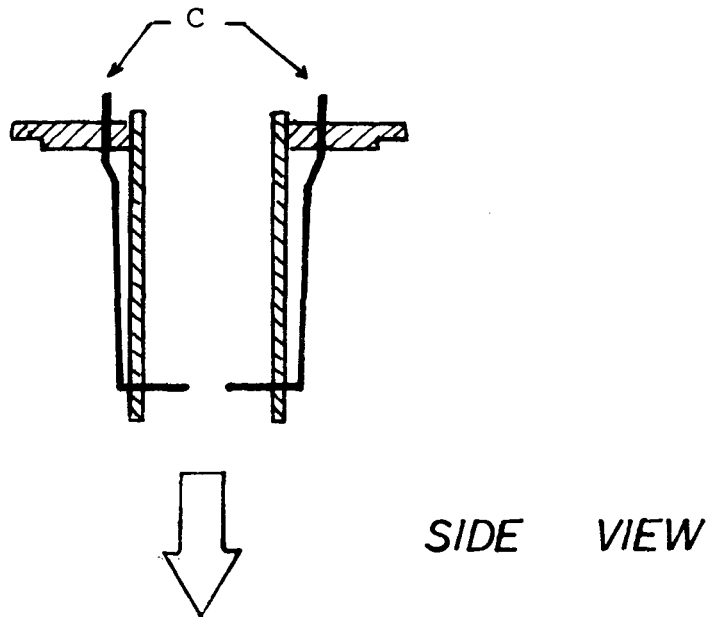
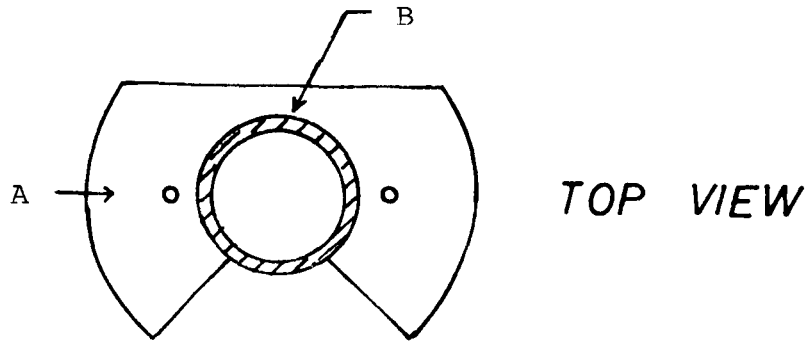


Figure 19. Schematic of the conductivity cell design.

drawn over its sides. Also, in a reducing atmosphere, iron alloyed with platinum.

In Figure 19, A is the alumina crucible cover with its center cored so that the 1" long alumina tube B (1/4" I.D., 3/8" O.D.) can fit through. The particular shape of A is to facilitate filling the cell with powder and to allow for ample gaseous exchange between the melt and the furnace atmosphere. Two 40 mil clearance holes were machined on A and B for the positioning of the platinum electrodes, (27 mil diameter wire), C. The cover, tube and the electrodes were secured using high temperature curing alundum cement with polyvinyl acetate binder. The electrodes were maintained at a distance of ~3mm apart. As a result, the conductivity chamber was limited to the enclosure of the Al_2O_3 tube. This two-point probe arrangement was used instead of the four-point technique in view of the relatively high conductivity of the system ($0.1 \text{ ohm}^{-1}\text{cm}^{-1}$). Preliminary results also indicated that the difference between the two methods was insignificant.

The cell constant of each conductivity cell was obtained by calibrating with two KCl solutions of different normality (0.04922N, 0.0216N, 0.0108N or 0.024N). Chiu⁽¹⁰⁴⁾ has reported the ac-conductivity of KCl in the range of .005-1.0N. The ac-conductance $C(d)$ of the cell with KCl solution filled to a distance, d , from the top was measured at 95KHz at room

TABLE II

Wet Chemical Analysis of $\text{FeO}\cdot\text{Fe}_2\text{O}_3\text{-Al}_2\text{O}_3\text{-SiO}_2$ Samples.

	Original Composition (wt%)			Analyzed Composition (wt%)		
	Fe_3O_4	Al_2O_3	SiO_2	Fe_3O_4	Al_2O_3	SiO_2
1	23.0	70.0	7.0	24.06	68.82	7.11
2	33.0	60.0	7.0	32.62	60.34	7.05
3	43.0	50.0	7.0	44.23	48.92	6.86
4	63.0	30.0	7.0	63.58	29.65	6.773
5	73.0	20.0	7.0	72.05	21.52	6.44
6	33.0	50.0	17.0	32.07	52.42	15.51
7	43.0	40.0	17.0	42.00	41.52	16.48
8	53.0	30.0	17.0	51.13	32.98	15.89

temperature. The cell constant $K'(d)$ was calculated with the equation,

$$K'(d) = \sigma/C(d) \quad (27)$$

The distance, d , was measured by studying the water mark left on the alumina tube by the KCl solution. A typical plot of the cell constant as a function of d is shown in Figure 20. It shows excellent agreement in the cell constant values obtained by using two different solutions. The cell constants obtained for all the conductivity cells were consistently in the same range of values.

The conductivity cell was filled with the powder composition and the whole assemblage cemented to the end of a cell holder consisting of two 30" long four-bore alumina thermocouple rods fixed to a brass end-cap. 14 mil platinum wires were used as leads. A platinum-platinum-10% Rodium thermocouple was positioned right next to the cell for temperature measurements.

In some instances, specimens in the form of rectangular bars (typically 2x 2 x 15 mm) were cut out of melted samples. The conductivity of these specimens was measured using 8 mil platinum wires as electrodes in a four-point method. Platinum paste was added to ensure good contact. The cross-sectional area, A , of the specimen was measured by a micrometer and the distance, Δl , between the voltage probes was measured with a cathetometer. The conductivity was,

$$\sigma = \frac{A}{\Delta l} \cdot \frac{1}{R} \quad (28)$$

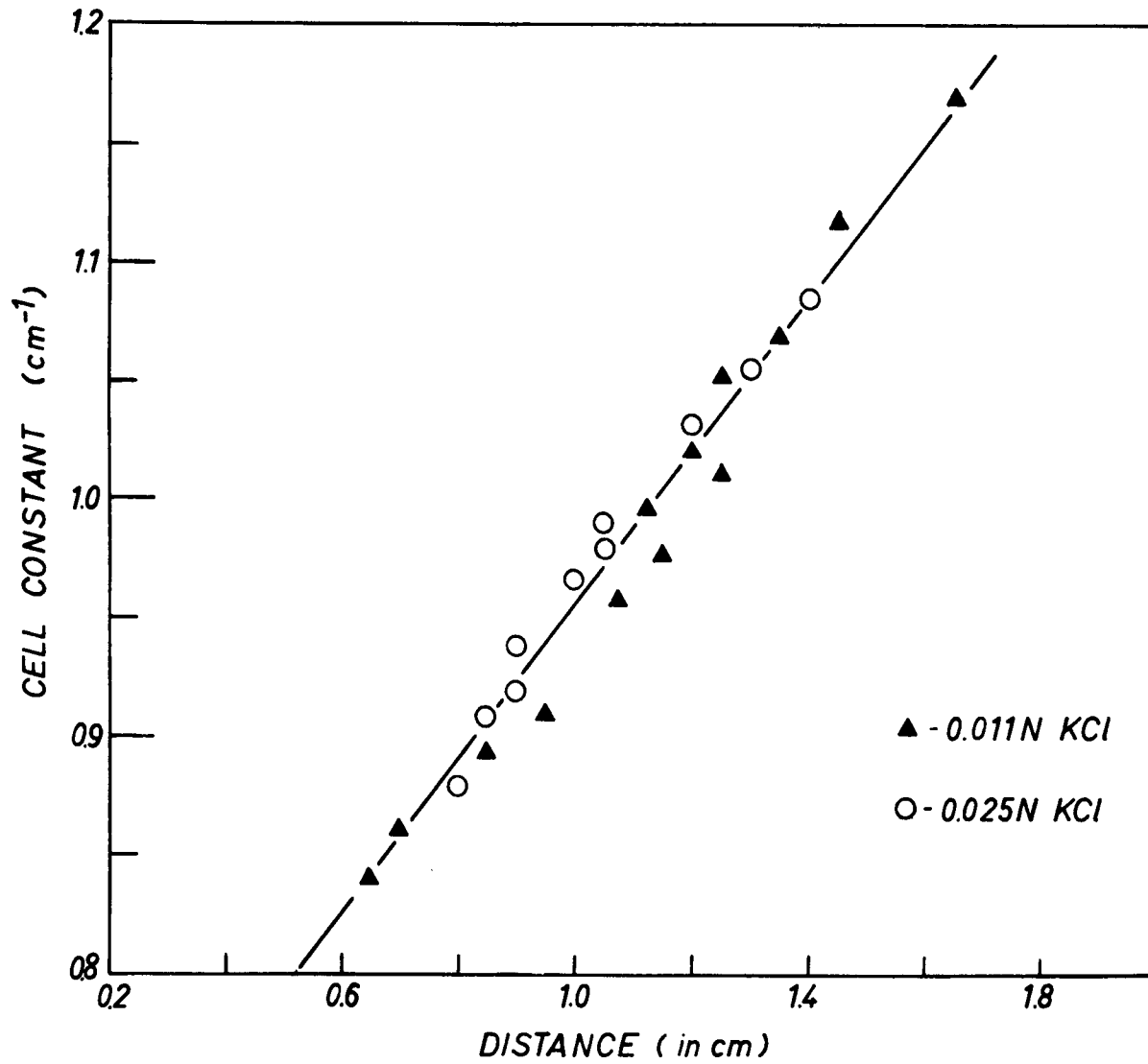


Figure 20. Cell constant as a function of liquid level in the conductivity cell.

V.2.1. Electrical Conductivity Measurement

In the dc-conductivity measurements, a 1 1/2 volt battery was used to apply the current through the conductivity cell. The current was measured by a Keithley model 160 multimeter in series. The voltage drop between the electrodes was recorded by a Keithley model 160B multimeter with input impedance of 10 mega ohm. A variable resistor was inserted to increase the total load.

The ohmic I-V characteristic of the conductivity cell is shown in Figure 21.

A Princeton Applied Science model 124A Lock-in-amplifier (LIA) was used for the ac measurement. The frequency range studied was from 1 to 10KHz. A constant current source was generated from the reference signal from the LIA (Figure 22) and passed through the sample. The voltage drop between the electrodes was first attenuated and measured by the LIA. To alleviate the noise and interference from the furnace current and the other electrical instruments, the power to the LIA was supplied through a Sola type CVS constant voltage transformer.

An instrument panel was constructed with the capability to measure four samples simultaneously. This switching panel was designed such that while the conductivity was taken of one sample, the other three were isolated from the circuit.

The conductivity cell was placed in a molybdenum wire wound hydrogen furnace with an alumina muffle. The conduct-

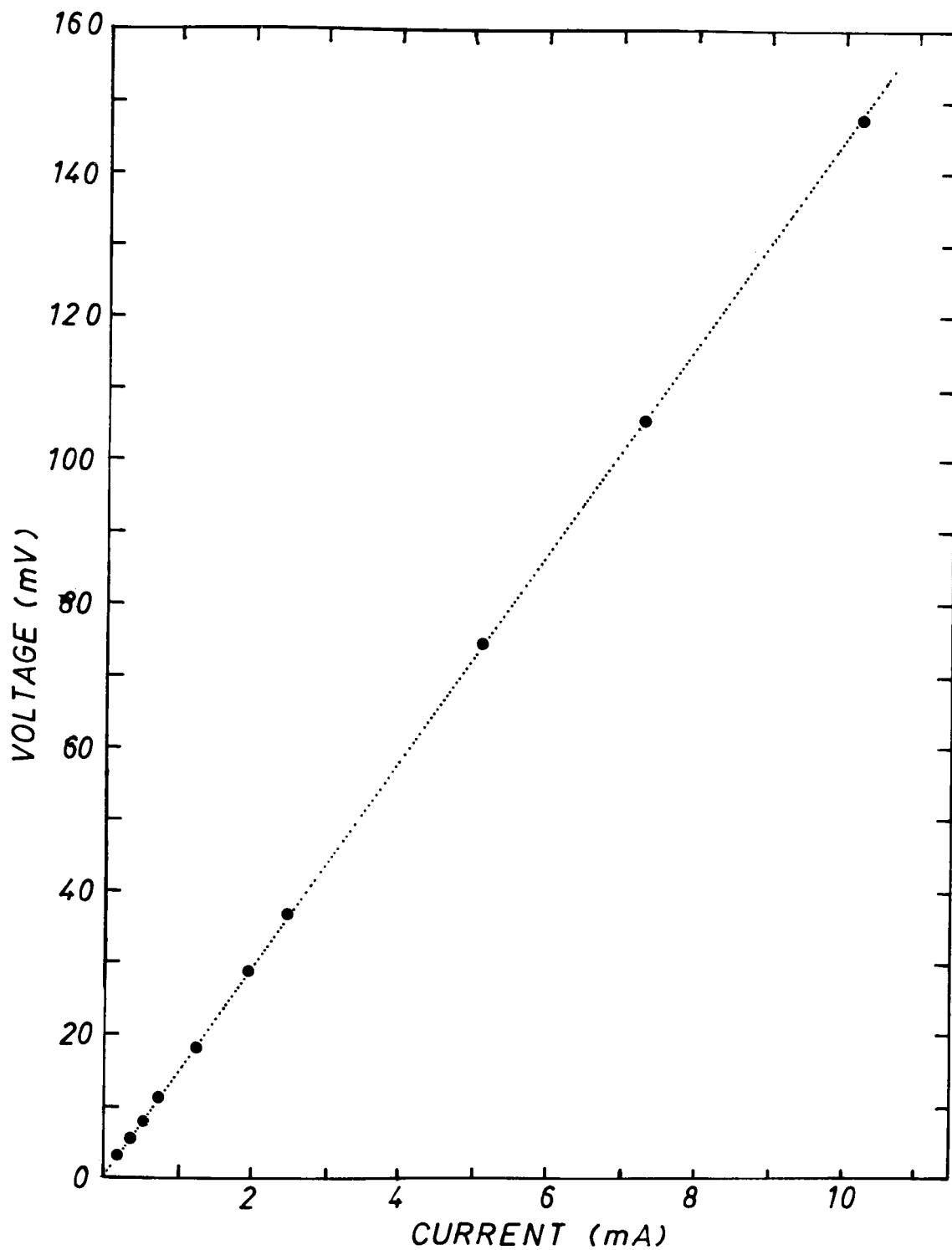


Figure 21. I-V characteristic of the conductivity circuit at 1347°C.

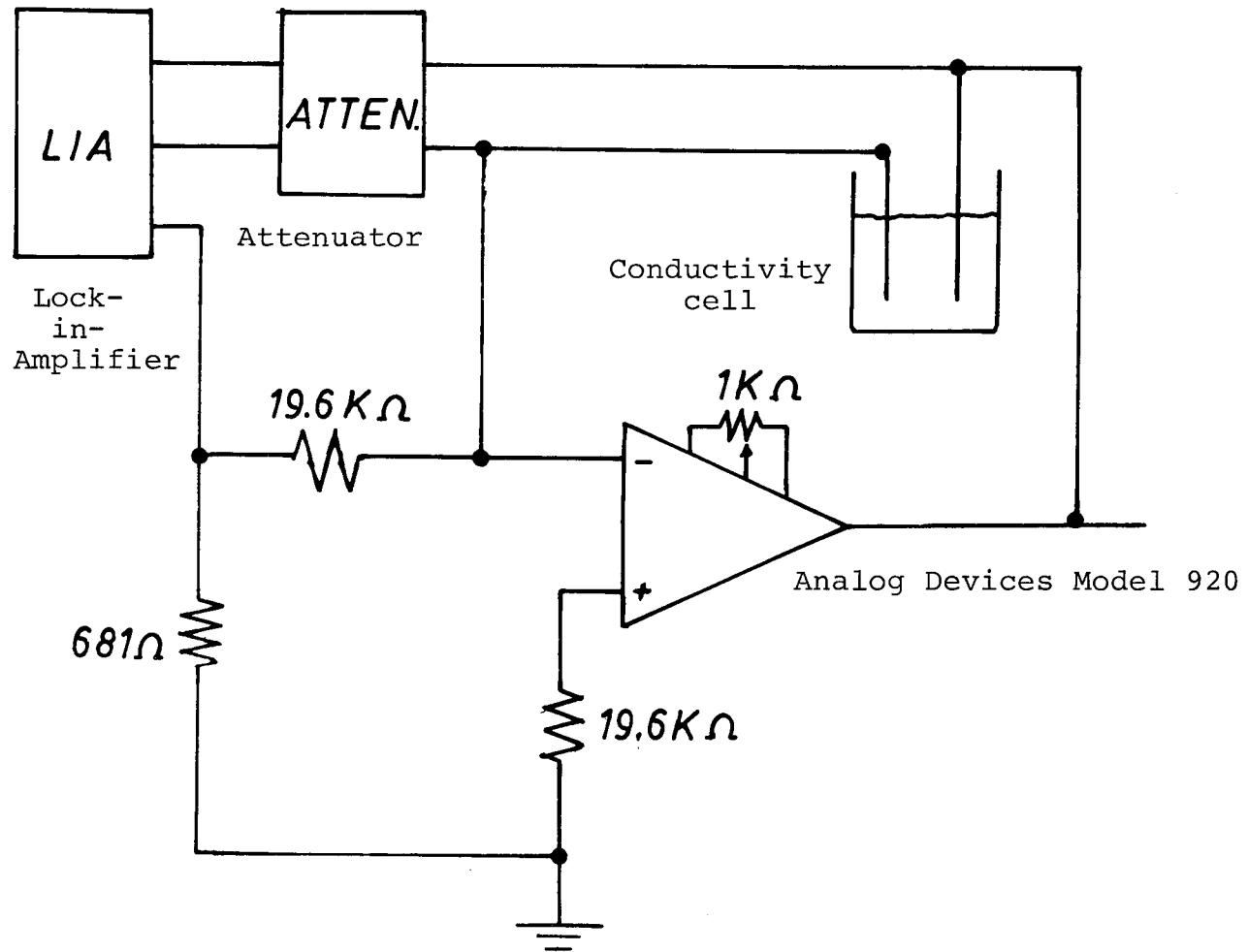


Figure 22. Circuit of the voltage controlled current source.

ivity was measured after the sample was equilibrated at different temperatures. The time of equilibration depended on the temperature. It varied from a minimum of three hours for samples with high iron content to over 10 hours for those with less iron.

The temperature range for this conductivity study was between 1000° and 1600°C. The sample was either a melt, melt plus solid or multiphase solid.

The conductivity dependence of samples with compositions in the spinel primary region as a function of furnace oxygen partial pressure was studied at 1550°C and 1600°C. The atmosphere control of the furnace is described in the following section.

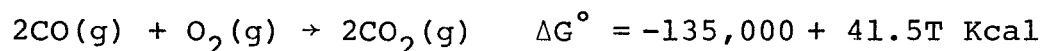
V.2.2. Oxygen Partial Pressure Control

The variation of equilibrium oxygen partial pressure in the furnace atmosphere was achieved via pre-determined flow ratios of Ar/O₂ and CO/CO₂ gaseous mixtures. Ar/O₂ mixtures were used for the oxygen partial pressure range of 1-10⁻³ atmosphere. The highest oxygen partial pressure attained with the CO/CO₂ mixture in the flow system was on the order of 10⁻⁵ atmosphere. The lowest partial pressure used was of the order of 10⁻⁹ atmosphere.

Before they entered the furnace, the gases were scrubbed of their water content by passing through columns of drierite and anhydrone. Ascarite was installed in the CO gas train

to absorb any trace of CO₂. Copper wire screens maintained at 450°C served as oxygen scrubbers for the Ar, CO and CO₂ gases. The flow volume of each gas was controlled by calibrated flowmeters to achieve a linear flow rate of about 1 cm/sec in the furnace.

The oxygen partial pressure in the furnace was determined by a calcia-stabilized zirconia cell located at the outlet of the furnace. The cell was maintained at 832°C. For the Ar/O₂ mixture, the induced emf of the cell gave the precise oxygen partial pressure. For CO/CO₂ mixtures the equilibrium oxygen partial pressure was controlled by the reaction,



The induced emf then gave the precise CO/CO₂ ratio from which the oxygen partial pressure at the furnace temperature could be calculated using the thermodynamic data for the above equation.

V.2.3. Experimental Error

The maximum error limit obtained in the conductivity results was less than 10%. The confidence in the accuracy of the measurement in the present study was established on the following grounds.

Repetitive measurement on different samples with the same batch composition produced conductivity data that were consistently within 10% of each other. Secondly, the ac-

conductivity which was measured in a different circuit was equivalent to the dc value. Also, the repeated melting, solidification, remelting and resolidification of the same sample gave reproducible results in both the solid and molten state. Finally, the reproducibility of the results was demonstrated by the agreement in the results obtained from a solid conductivity cell sample and a rectangular specimen.

While no error bars were drawn together with the presentation of results in Chapter VI, this error limit should be noted.

V.2.4. Identification and Characterization of Phases

This is a very important part of the present study. As the iron aluminosilicate melt solidified to form a multiphased agglomerate of either spinel, corundum, mullite and/or glass, the ability to identify the phases, and to characterize their compositions and volume fractions aided the analysis of the conductivity results.

Powders of each composition were melted and equilibrated in air at a specific temperature. The sample was then quenched in liquid nitrogen. Identification of the phases present in the quenched samples was done by the Debye-Scherrer x-ray diffraction method with an iron target. However, the lack of sufficient high angle peaks for the spinel structure led to the conclusion that this technique alone was unsuitable for a precision lattice parameter determination.

A powder x-ray diffraction pattern was obtained on a Norelco diffractometer with a Cu tube and a LiF monochromator. The precise 2θ values of the (333) and (440) diffractions of iron aluminum spinel were determined, using the internal standard silicon (311) peak ($2\theta = 56.122^\circ$) as a reference. The 2θ values for the same diffraction peaks of the end members, magnetite and hercynite, and of the iron aluminum spinel were determined experimentally.

A linear relationship was assumed to exist between the 2θ values and the spinel composition. To calculate the wt% of FeAl_2O_4 in the spinel, the following expressions⁽¹⁰⁵⁾ were used.

$$\text{wt\% FeAl}_2\text{O}_4 = \frac{2\theta^\circ - 56.84^\circ}{0.0206^\circ} \quad \text{for (333) peaks (29a)}$$

$$\text{wt\% FeAl}_2\text{O}_4 = \frac{2\theta^\circ - 62.42^\circ}{0.0232^\circ} \quad \text{for (440) peaks (29b)}$$

The compositions of the corundum, mullite, spinel and glassy regions were also measured by an electron probe micro-analyzer. The results on the spinel phase provided a good check for the above x-ray diffraction method. The compositions of the standards used were listed in Table III.

Volume fractions of different phases were obtained by point-counting on micrographs taken of representative areas. The different phases were readily recognizable without any etchant.

TABLE III

Standards Used for Composition Analysis in the
M.I.T. Earth and Planetary Electron Microscopy
Facility.*

Cossyrite - standard for Si

Element	Standard Oxide Composition (wt%)
Na	6.928
Si	40.922
Ti	8.706
Fe	40.971

Mn Ilmenite - standard for Fe

Element	Standard Oxide Composition (wt%)
Mg	0.2486
Ti	51.611
Mn	1.496
Fe	45.413

Enstatite Al 20 - standard for Al

Element	Standard Oxide Composition (wt%)
Mg	32.12
Al	19.98
Si	47.87

* Materials Analysis Corporation Model 5
Automated electron microprobe.

Chapter VI. Experimental Results

VI.1. Introduction

The results of the present study are presented in two main sections. The first part consists of the dc- and ac-conductivities in air as a function of temperature for different compositions (with 7 or 17 w/o SiO₂). The second half of this chapter deals with the isothermal dc-conductivity of silicate melts at 1550°C and 1600°C as a function of oxygen partial pressure.

The results in air are again divided into categories according to the original sample composition and the phase chemistry. Figure 23 shows the locations of the compositions that are investigated. The compatibility triangle $s_1c_1m_1$ corresponds to the compositions of the spinel, corundum and mullite phases in equilibrium with a silicate melt of composition P at 1460°C. A second compatibility triangle is SiO₂-s₂-m₂. It is composed of spinel, mullite and tridymite compositions co-existing with the melt of composition E at 1380°C.

Then the data in the first section is organized into the following four categories. The first includes samples which form crystallization products with a glassy matrix. They are the compositions within the compatibility triangle SiO₂-s₂-m₂. The second group consists of samples which have mullite as the matrix of the final crystalline composite. The majority of the compositions studied fit this description.

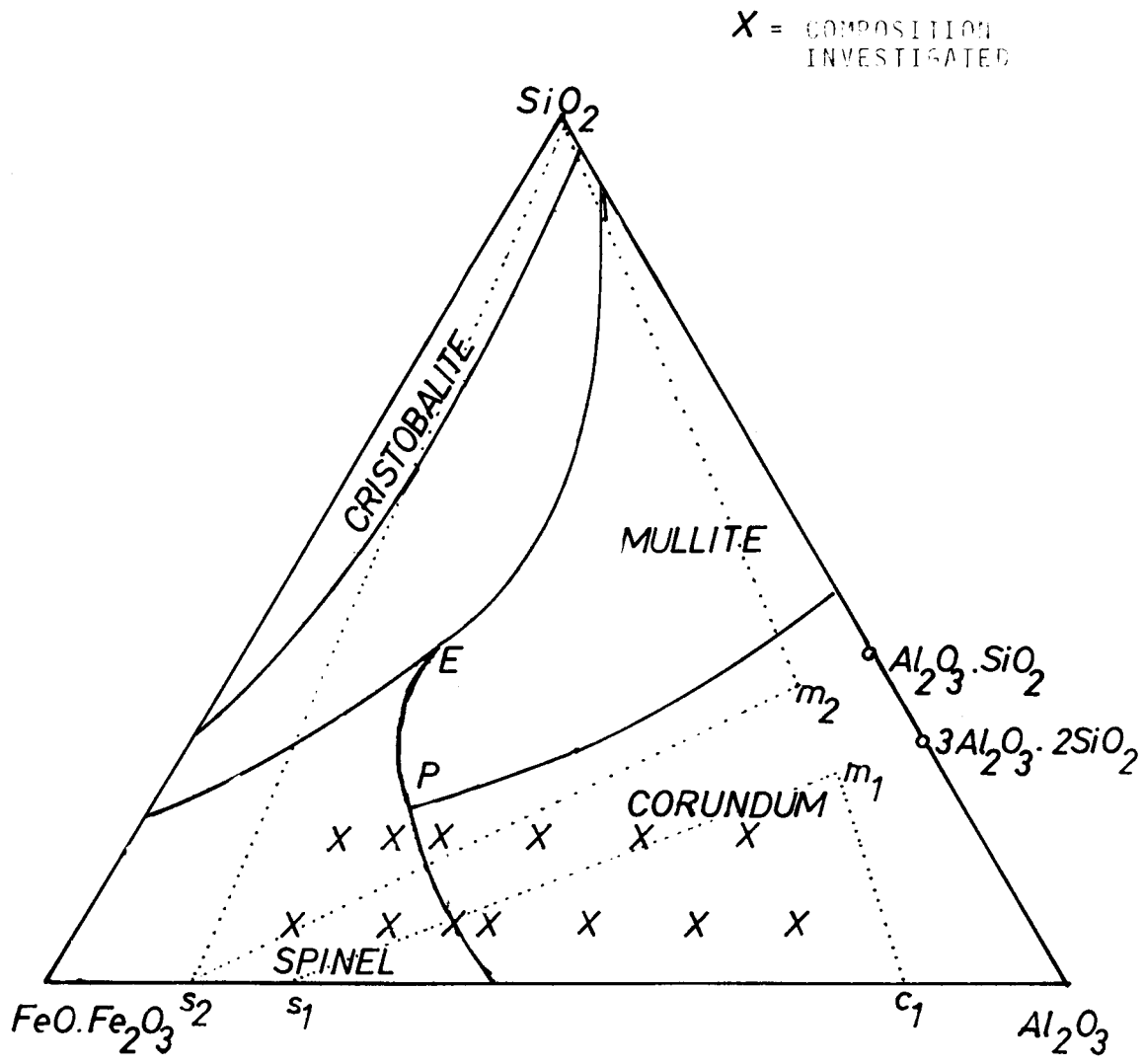


Figure 23. Location of the compositions investigated (with 7 and 17 wt% SiO_2) with respect to the $FeO \cdot Fe_2O_3$ - Al_2O_3 - SiO_2 system.

They are further separated into two sub-divisions; those that are within the quadrilateral $s_1 s_2 m_2 m_1$ and the ones inside the compatible triangle $s_1-c_1-m_1$. One other composition inside $s_1-c_1-m_1$ produced a solid assemblage with a corundum matrix. Its conductivity-temperature relationship is recorded individually. The last category of the results in air is the conductivity of iron aluminosilicate melts. The graphical presentation is then by means of a plot of

$\sigma T/c(1-c)$ versus reciprocal temperature, where c is the Fe^{3+}/Fe_{total} ratio.

Any results available from electron microanalysis and x-ray diffraction studies are also introduced in conjunction with the conductivity data. The ac-conductivity for compositions containing more than 33 wt% Fe_3O_4 is essentially equivalent to the dc values, indicating the predominantly electronic nature of the conduction process.

The chapter ends with the consideration of the isothermal dc-conductivity of silicate melts as a function of oxygen partial pressure and of Fe^{3+}/Fe_{total} .

VI.2. Conductivities in Air as a Function of Temperature

VI.2.1. Compositions with a Final Crystallization Product of Spinel Grains in an Interconnecting Glassy Matrix.

Three compositions that were studied fell into this category. They were $73Fe_3O_4-20Al_2O_3-7SiO_2$, $63Fe_3O_4-20Al_2O_3-17SiO_2$, and $33Fe_3O_4-30Al_2O_3-17SiO_2$ (in wt%). Their iso-

silica-alumina lines intersect the $\text{FeO}\cdot\text{Fe}_2\text{O}_3\text{-Al}_2\text{O}_3\text{-SiO}_2$ plane within the composition triangle $\text{SiO}_2\text{-s}_2\text{-m}_2$ (Figure 23). Of these three, the main research effort was concentrated on the composition 73F-20A-7S.*

Figure 24 gives the conductivity data in air versus reciprocal temperature for a sample of 73F-20A-7S. The temperature ranged from 1550°C to 1024°C. The conductivity value at 1550°C was $0.237 \text{ ohm}^{-1} \cdot \text{cm}^{-1}$ which was obtained by averaging the results of four different runs. Figure 24 shows that the conductivity, while being somewhat insensitive to temperature, increased with decreasing temperature. It also did not show any discontinuity upon complete solidification of the sample. From such a plot, no simple relationship between conductivity and temperature could be derived. The equilibration time permitted between data points was 5-6 hours. At o_1 and o_2 , the sample was held overnight (16 hours). o_1 was at 1365°C. For the phase diagram, it was apparent that the last liquid of this sample composition disappeared near 1390°C.

Similar behavior was exhibited by samples of 63F-20A-17S and 53F-30A-17S (Figures 25 and 26). Likewise, the curves could not be fitted by a simple linear relationship versus reciprocal temperature.

* The following abbreviations are used: F = Fe_3O_4 , A = Al_2O_3 , and S = SiO_2 . Numbers are expressed in weight %.

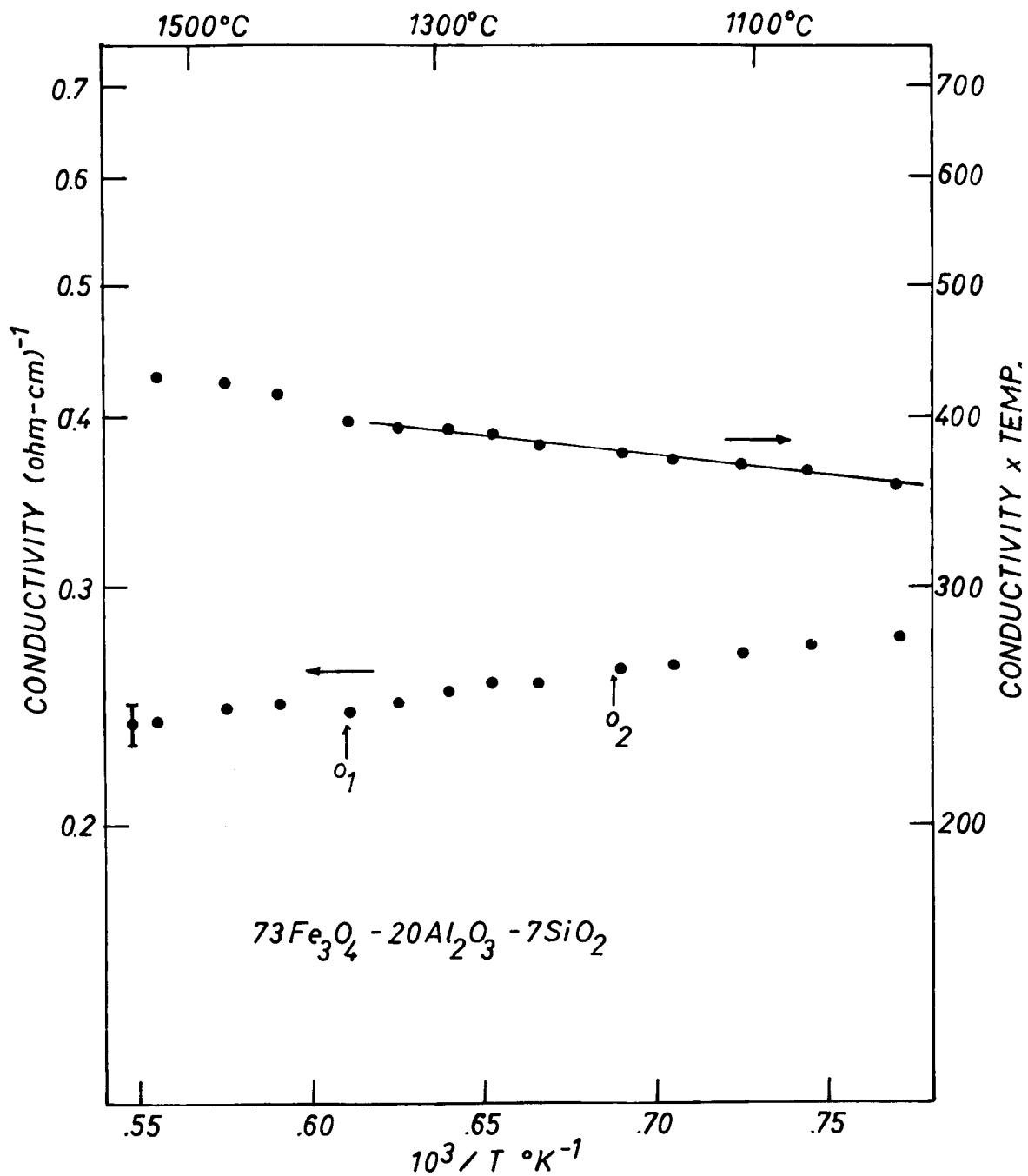


Figure 24 . Temperature dependence of the electrical conductivity of composition $73\text{Fe}_3\text{O}_4 - 20\text{Al}_2\text{O}_3 - 7\text{SiO}_2$.

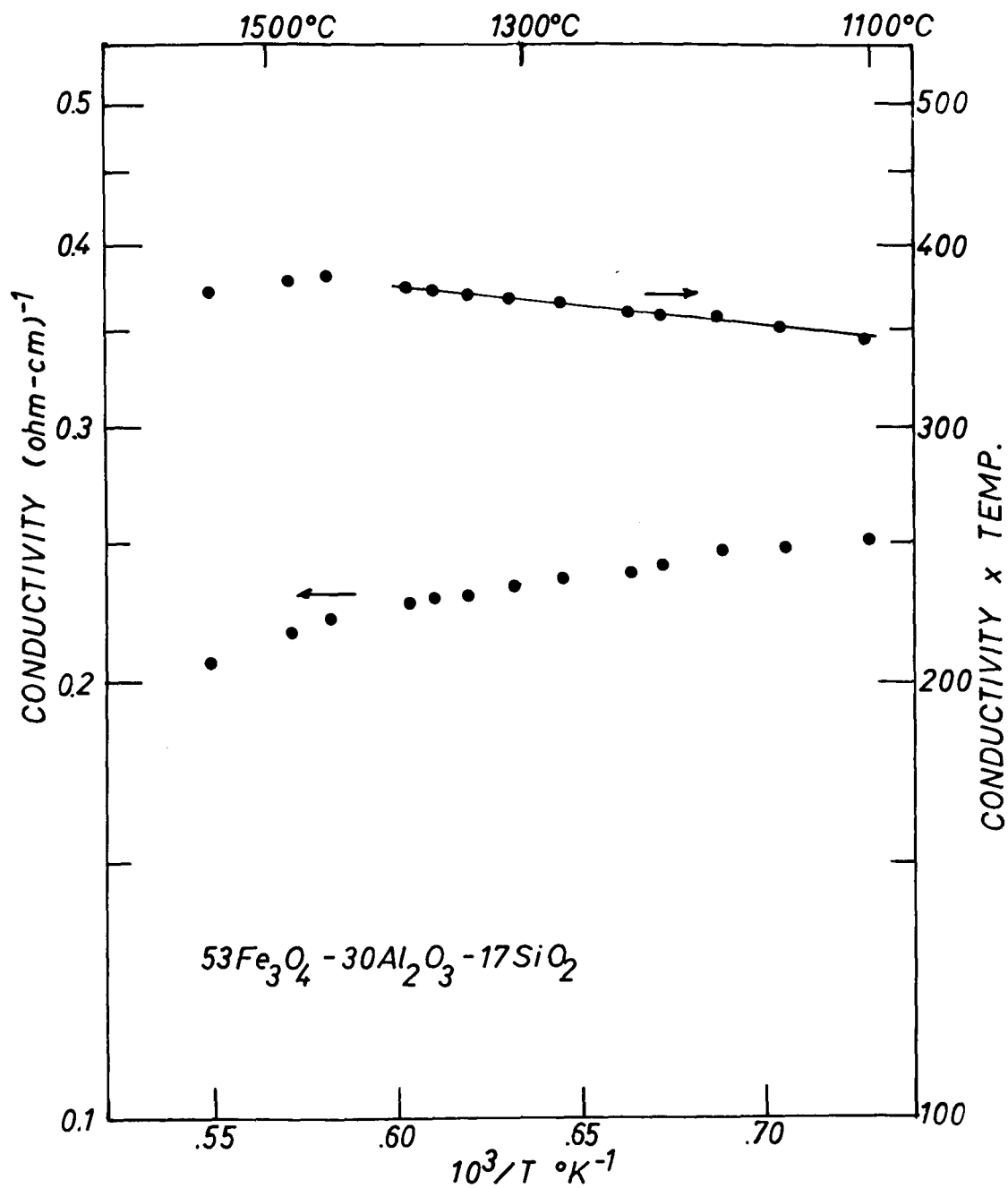


Figure 25. Temperature dependence of the electrical conductivity of composition $53\text{Fe}_3\text{O}_4-30\text{Al}_2\text{O}_3-17\text{SiO}_2$.

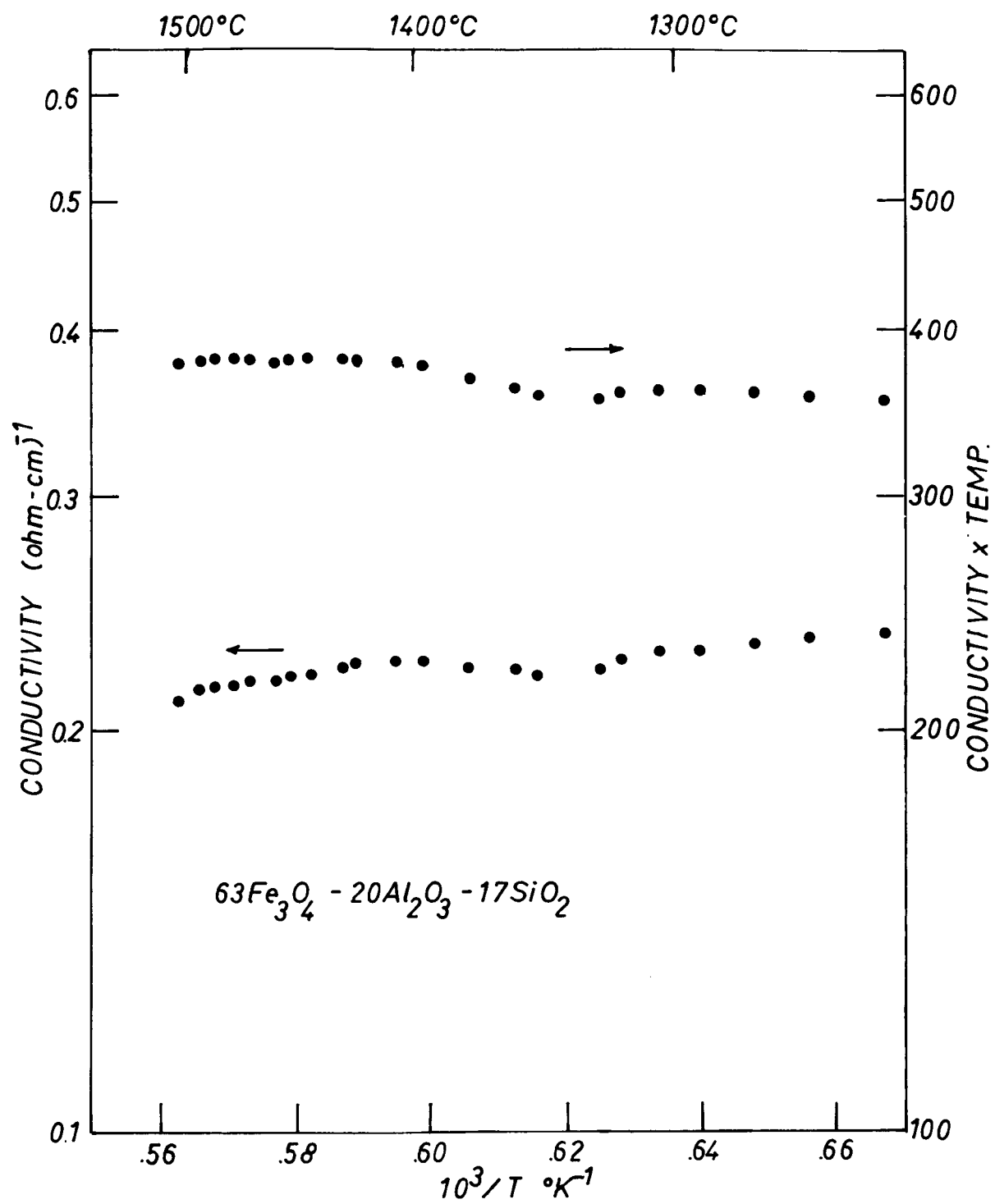


Figure 26 . Temperature dependence of the electrical conductivity of composition $63\text{Fe}_3\text{O}_4-20\text{Al}_2\text{O}_3-17\text{SiO}_2$.

The same data are, in Figure 24, plotted as the product (conductivity x temperature) versus reciprocal temperature. The data below 1390°C were fitted with a linear relationship and an apparent activation energy of 0.0584eV was obtained.

The following experiments were carried out to affirm that this behavior which was observed for all the samples of this composition was not spurious. One sample was held at 1360°C for over 80 hours. The conductivity remained constant throughout the whole period. In another case, a sample was first quenched from 1540°C to 1200°C in 15 minutes. It was then re-annealed at 1355°C for 20 hours and then cooled. The data were reproduced.

The conductivity remained between 0.2-0.3 $\text{ohm}^{-1}\cdot\text{cm}^{-1}$ over a wide temperature range. To look at the effect of temperature on the conductivity, a sample was melted and the data taken from 1550°C down to 210°C. The results are plotted in Figure 27. The difference in conductivity between 270°C and 1550°C, where the sample was a melt with one-third volume fraction of spinel ($62\text{Fe}_3\text{O}_4-38\text{FeAl}_2\text{O}_4$), was merely a factor of 3.42. Above 600°C, the conductivity increased with decreasing temperature. The opposite effect was observed for temperatures below 600°C. Also superimposed on the same plot, but on a different scale, was the product of (conductivity x temperature). A bend occurred near 600°C resulting in a higher activation energy for the low temperature region.

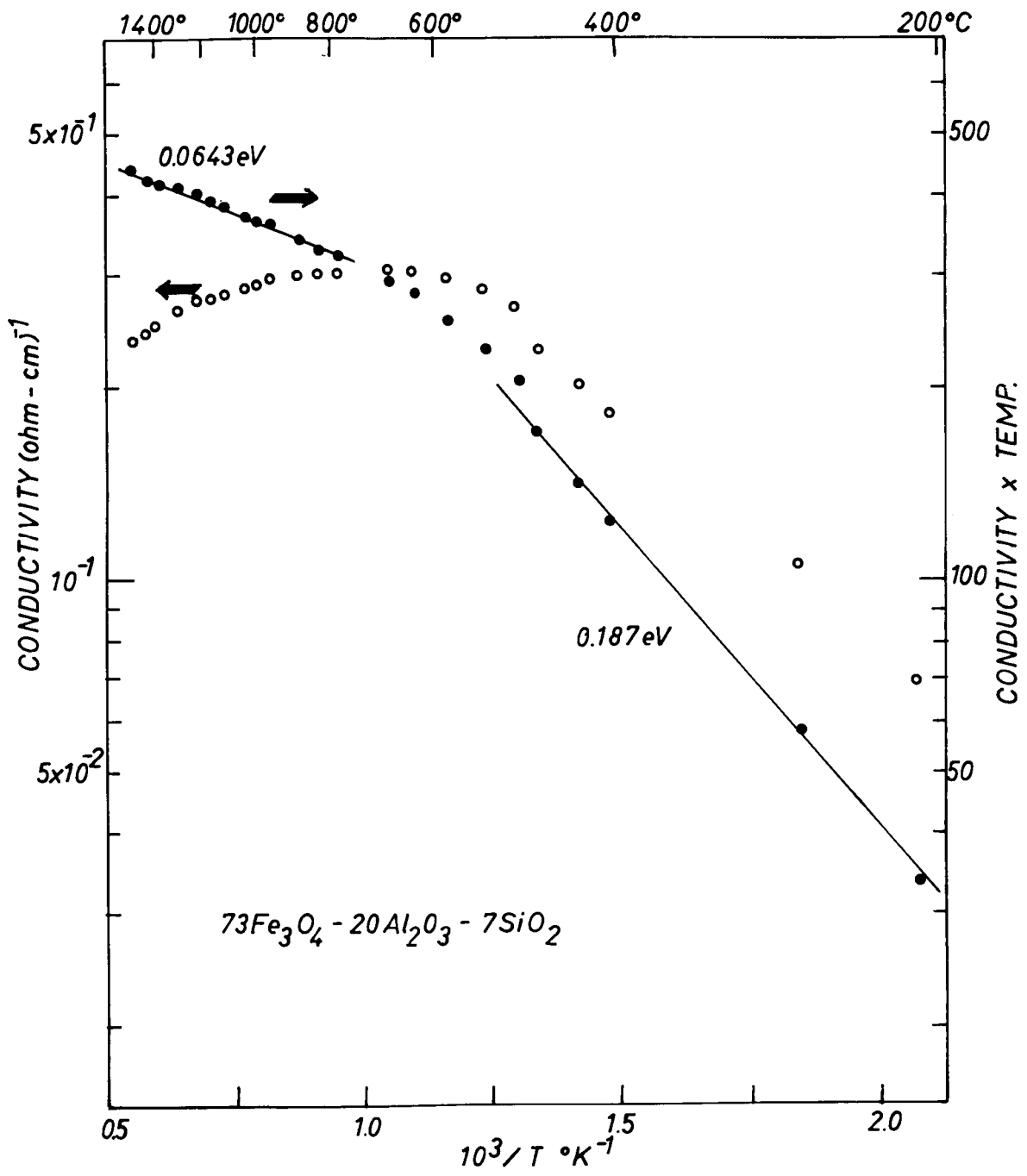


Figure 27. Electrical conductivity as a function of temperature for composition $73\text{Fe}_3\text{O}_4-20\text{Al}_2\text{O}_3-7\text{SiO}_2$.

Figure 28 is a micrograph of a sample quenched from 1526°C. It illustrates that the equilibrium phases at 1526°C in air are spinel and melt. The spinel composition was determined as 55.97Fe₃O₄-43.76FeAl₂O₄ (in wt%). The dendritic structure was the spinel crystallites formed during quenching.

It was predicted that such a composition would give a crystalline mixture of spinel, tridymite and mullite as it solidified. However, a careful study of a sample melted at 1550°C, slowly cooled until 1250°C where it was held for 24 hours showed that the situation was not that unambiguous.

Figure 29 shows the final microstructure. Grain growth has occurred for the spinel phase during the annealing at 1250°C. The optical micrograph indicated that the large spinel grains were separated by interconnecting regions. X-ray fluorescence study confirmed that these areas were rich in silica. The electron microanalysis results were 58.74Fe₃O₄-39.92FeAl₂O₄ for spinel and 7.05FeO 21.56Al₂O₃ 69.13SiO₂ for the matrix with the SiO₂ content ranging from 53.54 to 76.27 wt%. The huge variation in the analysis of the silica-rich region reflected its homogeneity.

The volume fraction occupied by this silica-rich region was 26.1%, calculated by point counting. The Debye-Scherrer diffraction pattern failed to show any trace of mullite and silica (Table IV). The only diffraction peaks obtained were those from spinel. Electron microprobe data gave 58.74Fe₃O₄-39.92FeAl₂O₄ as the only spinel composition. However, x-ray diffraction results provided additional information. At least three

Spinel grain

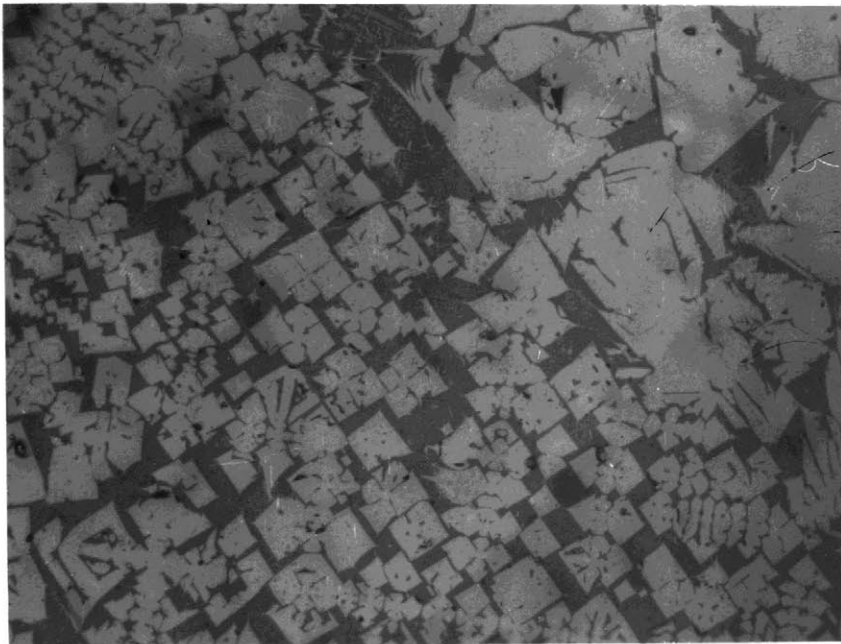
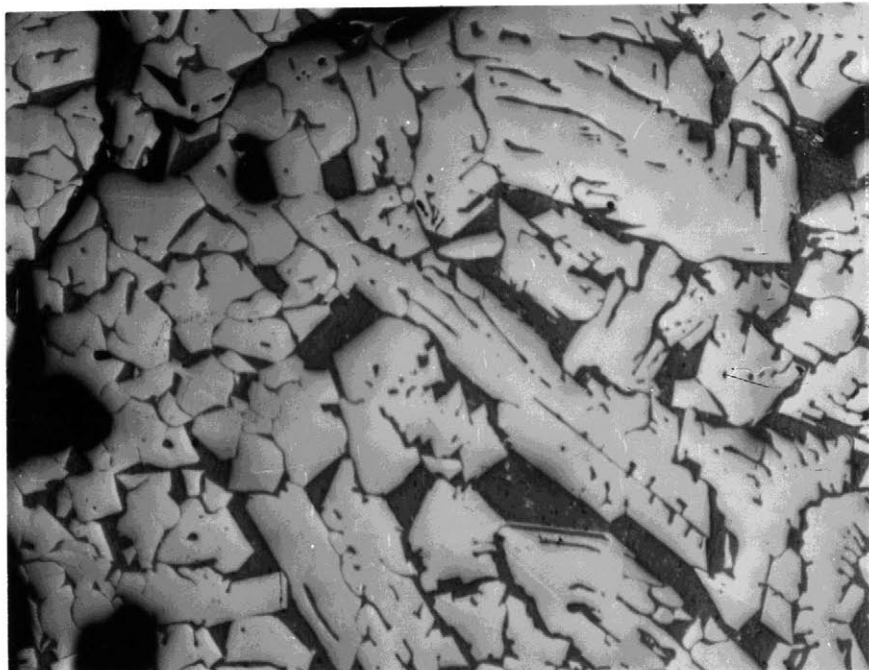


Figure 28. Microstructure of a sample of composition $73 \text{Fe}_3\text{O}_4-20\text{Al}_2\text{O}_3-7\text{SiO}_2$ quenched from 1526°C . (Magnification 200X)

Spinel



Glassy matrix

Figure 29. The microstructure of a sample of composition $73\text{Fe}_3\text{O}_4-20\text{Al}_2\text{O}_3-7\text{SiO}_2$ annealed in air at 1250°C for 24 hours. (Magnification 50x)

TABLE IV

X-ray diffraction pattern for $73\text{Fe}_3\text{O}_4-20\text{Al}_2\text{O}_3-7\text{SiO}_2$
 melted and held at 1250°C for 24 hours, with Fe x-ray,
 MnO filter.

$2\theta^\circ$	d (\AA)	Intensity	Assignment (spinel) (hkl)
39.22°	2.884	MW	220
43.56°	2.609	VVW	
46.24°	2.465	S	311
48.46°	2.359	VVW	
56.58°	2.042	MW	400
70.67°	1.674	VW	422
75.46°	1.582	M	511
82.02°	1.475	S	440
99.25°	1.271	VW	533, 622
126.7°	1.083	VW	642
137.25°	1.039	VW	553, 731

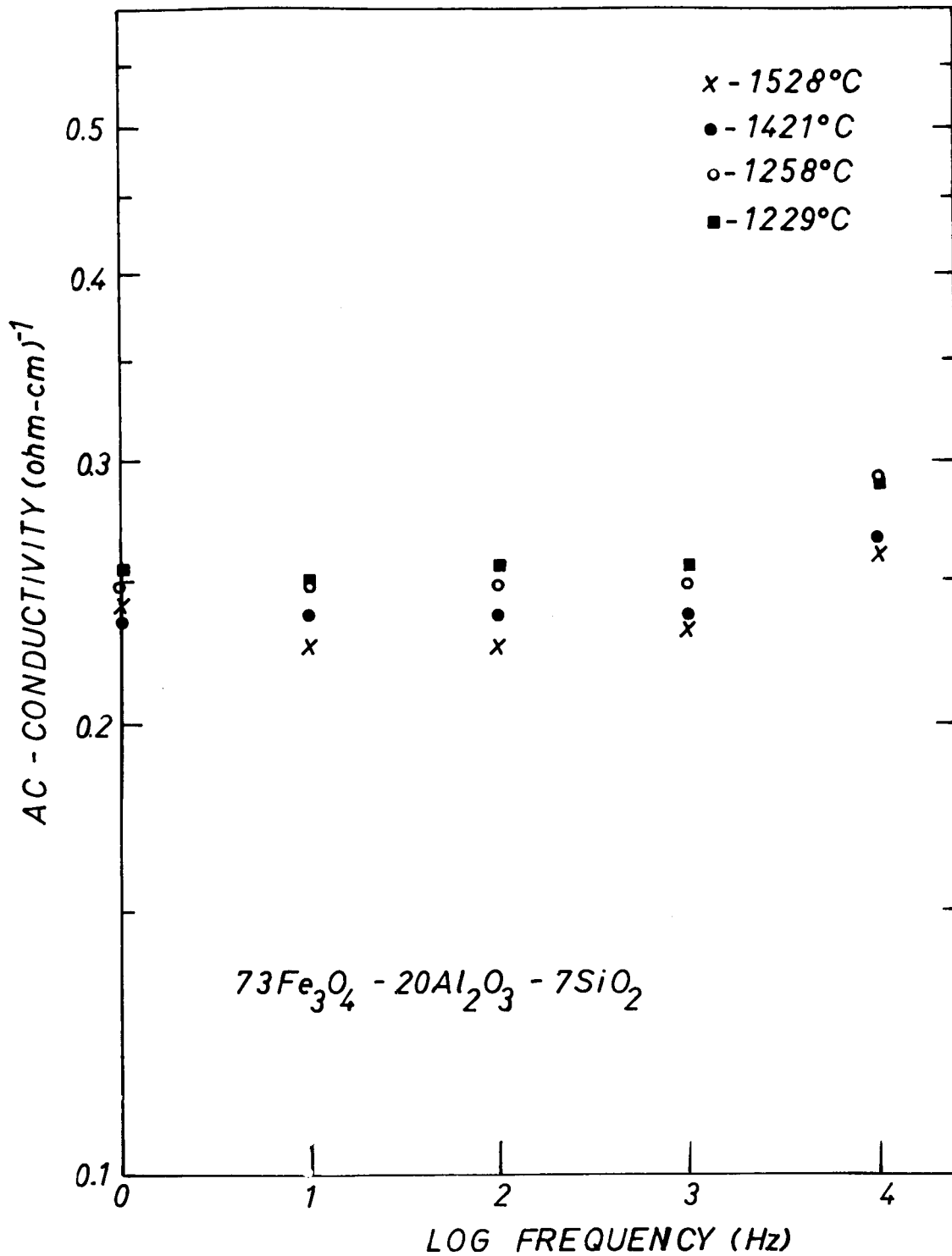


Figure 30. Isothermal ac-conductivity as a function of frequency for composition $73\text{Fe}_3\text{O}_4 - 20\text{Al}_2\text{O}_3 - 7\text{SiO}_2$.

different compositions of spinel were measured: $48.14\text{Fe}_3\text{O}_4$ - $51.86\text{FeAl}_2\text{O}_4$, $63.8\text{Fe}_3\text{O}_4$ - $36.2\text{FeAl}_2\text{O}_4$ and $93.99\text{Fe}_3\text{O}_4$ - $5.01\text{FeAl}_2\text{O}_4$.

The ac-conductivities in the range of 1-10 KHz were equivalent to the dc data, within experimental limits. Figure 30 compares the results at 1528°C , 1421°C , 1258°C and 1229°C of composition 73F-20A-7S. The ac-conductivities for compositions 63F-20A-17S and 53F-30A-17S were also independent of frequency in the above frequency range.

VI.2.2. Compositions with Mullite as the Matrix Phase of the Multi-Phased Crystallization Product.

Most of the compositions studied fell into this category. The compositions were $63\text{Fe}_3\text{O}_4$ - $30\text{Al}_2\text{O}_3$ - 7SiO_2 , $58\text{Fe}_3\text{O}_4$ - $35\text{Al}_2\text{O}_3$ - 7SiO_2 , $53\text{Fe}_3\text{O}_4$ - $40\text{Al}_2\text{O}_3$ - 7SiO_2 , $48\text{Fe}_3\text{O}_4$ - $45\text{Al}_2\text{O}_3$ - 7SiO_2 , $46\text{Fe}_3\text{O}_4$ - $47\text{Al}_2\text{O}_3$ - 7SiO_2 , $43\text{Fe}_3\text{O}_4$ - $50\text{Al}_2\text{O}_3$ - 7SiO_2 , $33\text{Fe}_3\text{O}_4$ - $60\text{Al}_2\text{O}_3$ - 7SiO_2 , $43\text{Fe}_3\text{O}_4$ - $40\text{Al}_2\text{O}_3$ - 17SiO_2 , and $33\text{Fe}_3\text{O}_4$ - $50\text{Al}_2\text{O}_3$ - 17SiO_2 . These can be further split into two groups according to the microstructure of their crystallization products. The first group was those of the compositions inside the quadrilateral $s_1s_2m_2m_1$ in Figure 23. For them, the corundum phase began to be resorbed at 1460°C . The microstructure then showed spinel grains in a mullite matrix together with amounts of the remnant corundum phase. The second consisted of those of the above compositions that lie inside the triangle $s_1m_1c_1$ in Figure 23. Their crystallization product formed from the molten state was

a three phase mixture of spinel and corundum grains in a mullite matrix.

Typically, the conductivity dependence on temperature for these compositions displayed a three-stage behavior. At high temperature (region I) where the equilibrium phases were the melt with a suspension of crystalline phase(s), the conductivity had a slight dependence on temperature. The third region (region III) was the conduction through the mullite matrix at low temperature. The conductivity measured was an effective one which depended on the volume fractions of the spinel, corundum and mullite present. The thermal activation energy varied according to the composition of the mullite phase. An intermediate transition region, where the conductivity underwent a sharp discontinuous change, separated regions I and III.

These two groups will now be treated separately.

a) Compositions within the area $s_1s_2m_2m_1$.

The compositions included under this heading were

$63\text{Fe}_3\text{O}_4-30\text{Al}_2\text{O}_3-7\text{SiO}_2$, $58\text{Fe}_3\text{O}_4-35\text{Al}_2\text{O}_3-7\text{SiO}_2$, $53\text{Fe}_3\text{O}_4-40\text{Al}_2\text{O}_3-7\text{SiO}_2$, $48\text{Fe}_3\text{O}_4-45\text{Al}_2\text{O}_3-7\text{SiO}_2$, $43\text{Fe}_3\text{O}_4-40\text{Al}_2\text{O}_3-17\text{SiO}_2$, and $33\text{Fe}_3\text{O}_4-50\text{Al}_2\text{O}_3-17\text{SiO}_2$.

Figure 31 is a conductivity versus reciprocal temperature plot for $63\text{Fe}_3\text{O}_4-30\text{Al}_2\text{O}_3-7\text{SiO}_2$ (63F-30A-7S). The sample was first melted, with the initial data point taken at 1560°C. As the temperature was lowered to about 1400°C, region II took over. It should be noted that the apparent activation energy

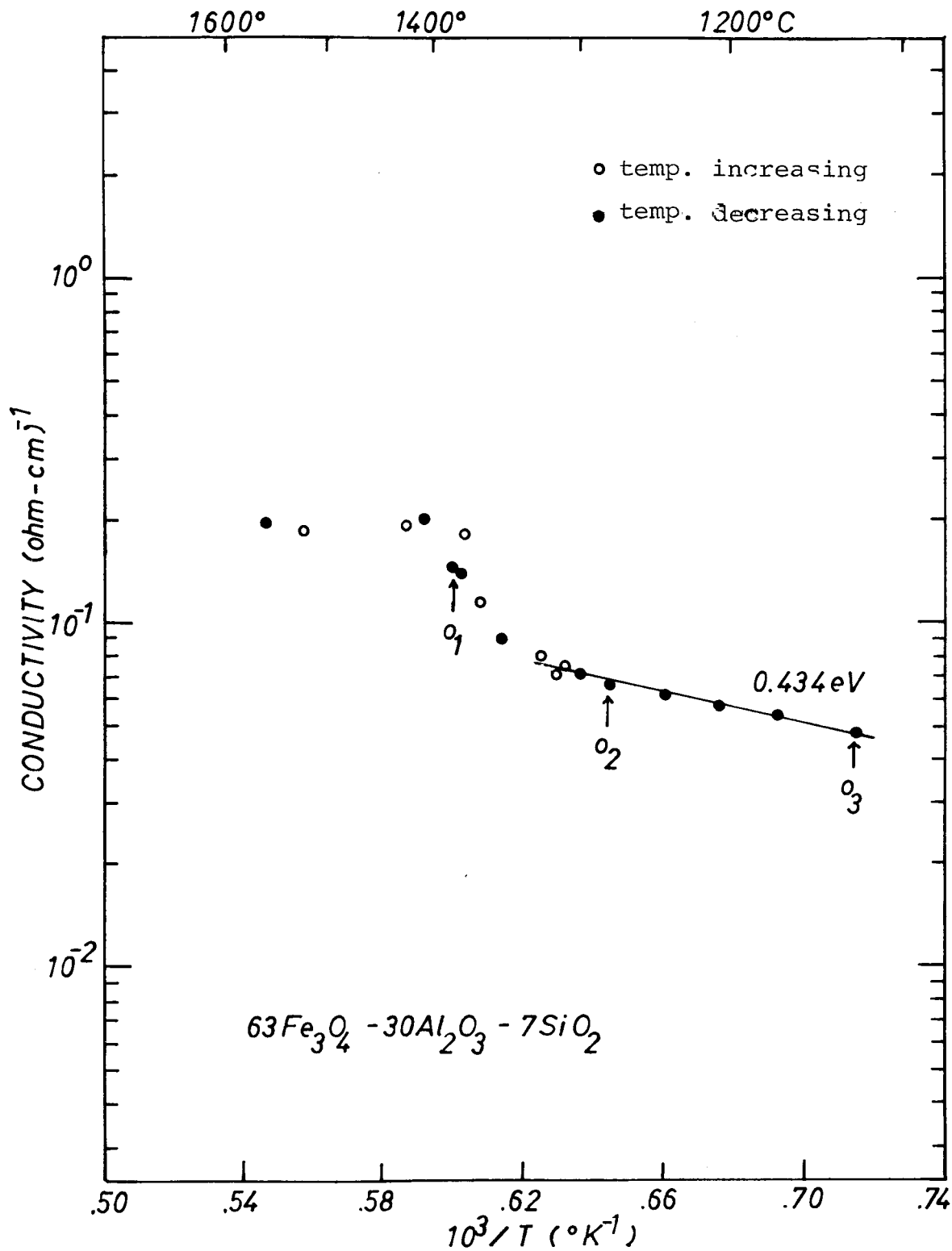


Figure 31. Electrical conductivity as a function of temperature for composition $63Fe_3O_4-30Al_2O_3-7SiO_2$.

of region II has no actual physical significance. Region II was simply a transitory situation between regions I and III. When 1128°C was reached, the sample was reheated. The data taken during this upswing in temperature indicated that the conductivity results were reproducible. σ_1 (1388°C), σ_2 (1277°C) and σ_3 (1128°C) were the temperatures at which the sample was held overnight. The conduction in the multiphased solid aggregate had an activation energy of 0.434eV.

In the above, the significance of the slope in region II was alluded to. The conductivity plot of sample 58F-35A-7S helps illustrate this point (Figure 32). A hysteresis loop existed between the data taken with decreasing temperature and those with increasing temperature. The conductivity taken while the sample was solidifying was higher. Again the conductivity increased slightly with decreasing temperature in region I where the sample was a melt saturated with spinel and corundum. The junction between regions I and II was at 1390°C. At σ_1 (1230°C) the sample was held overnight. The low temperature range had an activation energy of 0.447eV.

The data for samples of 58F-35A-7S, 48F-45A-7S, 43F-40A-17S and 33F-50A-17S were compared in Figure 33. One important point is that region II became predominant at or just above 1380°C for every sample. Also, the conductivities of 43F-40A-17S and 33F-50A-17S decreased with decreasing temperature in region I. This was due in part to the increasing corundum and mullite volume fractions in the melt, which were much less

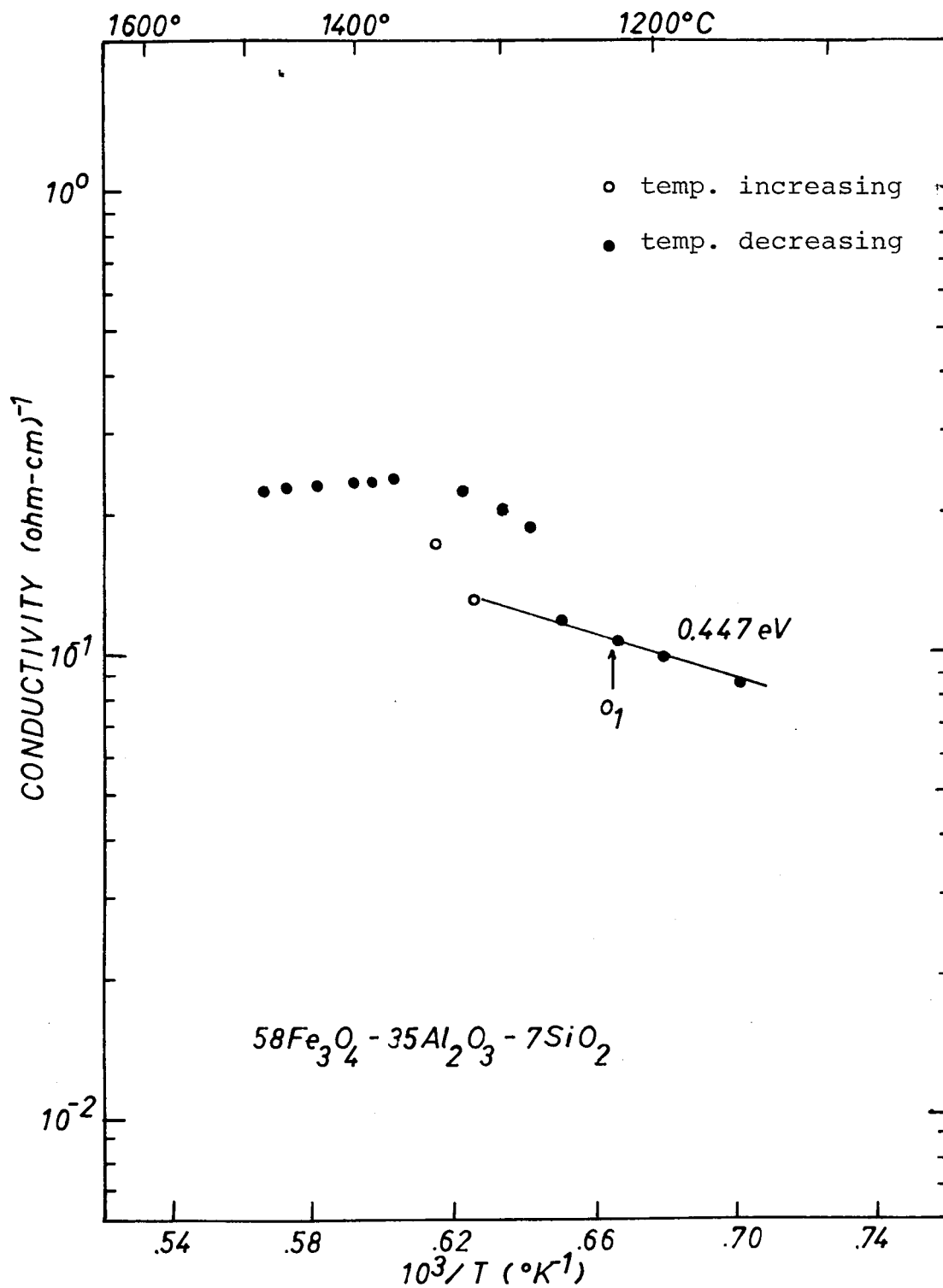


Figure 32. Electrical conductivity as a function of temperature for composition $58\text{Fe}_3\text{O}_4-35\text{Al}_2\text{O}_3-7\text{SiO}_2$.

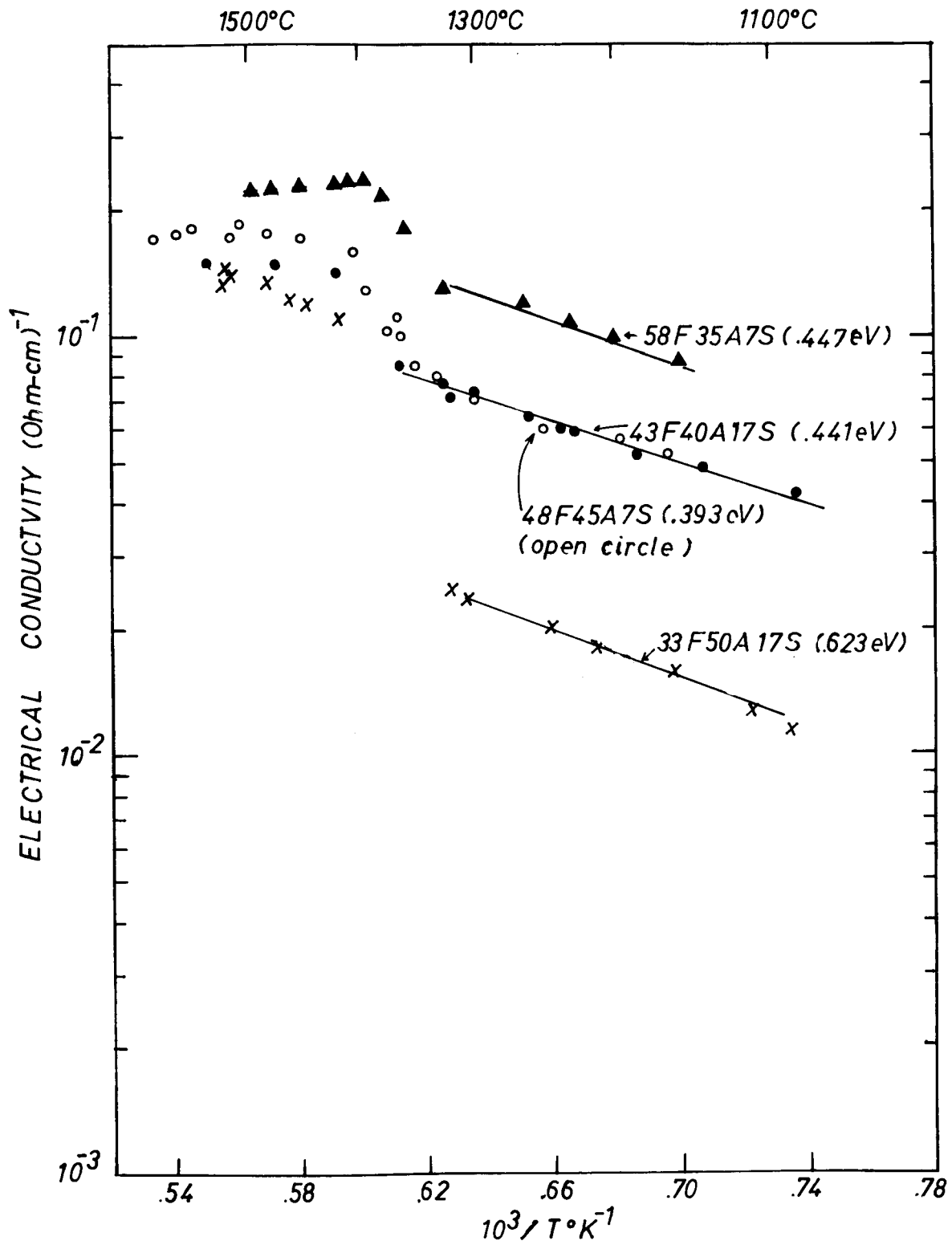


Figure 33. Electrical conductivities of four compositions within the $s_1s_2m_2m_1$ quadrilateral.

conductive than the melt itself. In addition, the $\text{Fe}^{3+}/\text{Fe}^{2+}$ ratio in the melt was increasing and deviating further away from unity as the temperature dropped. The activation energies for conduction via the mullite matrices varied from .393 - .623eV.

The composition 63F-30A-7S is just off to the spinel side of the spinel-corundum-melt three phase boundary. Table V is the x-ray diffraction data for a sample quenched from 1520°C. Spinel was the only crystalline phase detected. Figure 34 is the microstructure of a 63F-30A-7S sample melted at 1550°C, slowly cooled and annealed at 1250°C for 24 hours. It showed 75.17 Fe_3O_4 -24.68 FeAl_2O_4 spinel grains and remnant corundum particles (20.50mol % Fe- Al_2O_3) in a mullite matrix (19.37 w/o Fe_2O_3 , 60.6 w/o Al_2O_3 , 25.03 w/o SiO_2). The compositions were obtained from electron microprobe analysis.

The ac-conductivities of these samples were also independent of frequency in the range of 1 - 10KHz. This applied for samples both in the molten and the solid state. Figures 35 , 36 and 37 are ac-conductivity versus log frequency plots at various temperatures for compositions 63F-30A-7S, 48F-45A-7S and 33F-50A-17S respectively.

b) Compositions Within the Compatible Triangle $s_1m_1c_1$.

Of the four compositions in this triangle that were investigated, three had mullite as the matrix phase in the final crystallization product. They were 47 Fe_3O_4 -46 Al_2O_3 -

TABLE V

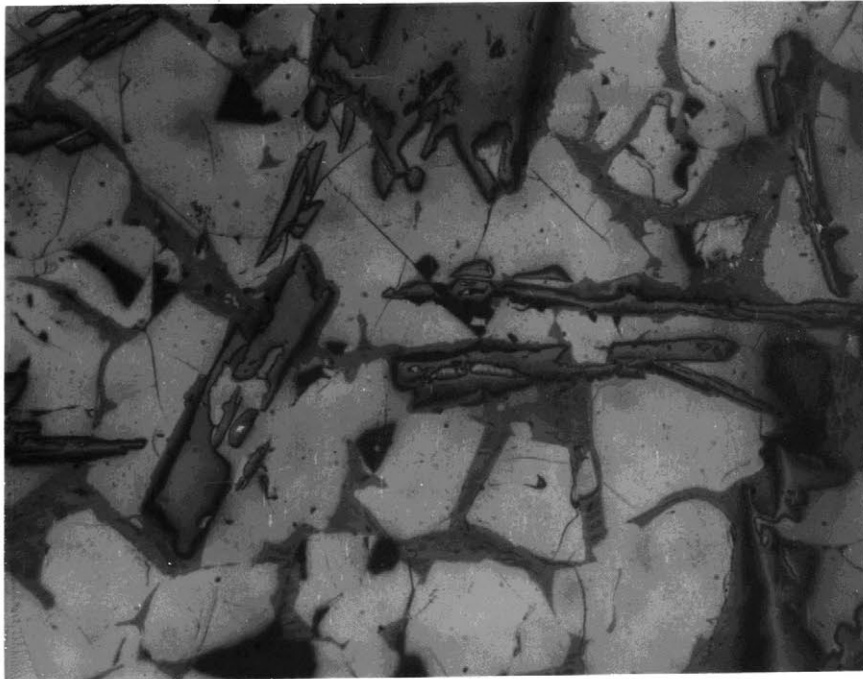
X-ray diffraction pattern for $63\text{Fe}_3\text{O}_4-30\text{Al}_2\text{O}_3-7\text{SiO}_2$
 melted and held at 1250°C for 24 hours, without filter.

$2\theta^\circ$	d (Å)	Intensity	Assignment (Spinel)
23.824	4.689	6	111
35.53	3.172	6	
39.487	2.865	2	220
42.02	2.699	5	
46.61	2.447	1	311
56.82	2.0344	3	400
68.28	1.725	5	422
71.42	1.658	5	422
76.49	1.5637	4	511
82.78	1.464	3	440
95.45	1.308	6	620
100.21	1.262	6	533,622
108.78	1.191	6	444
115.32	1.146	6	444
123	1.101	6	642
129.0	1.072	5	553,731
140.4	1.029	5	800

1 is the strongest, intensity decreases with number.

Corundum

Mullite matrix



Spinel grain

Figure 34. Microstructure of a sample of $63\text{Fe}_3\text{O}_4-30\text{Al}_2\text{O}_3-7\text{SiO}_2$ annealed in air at 1250°C for 24 hours. (Magnification 200x).

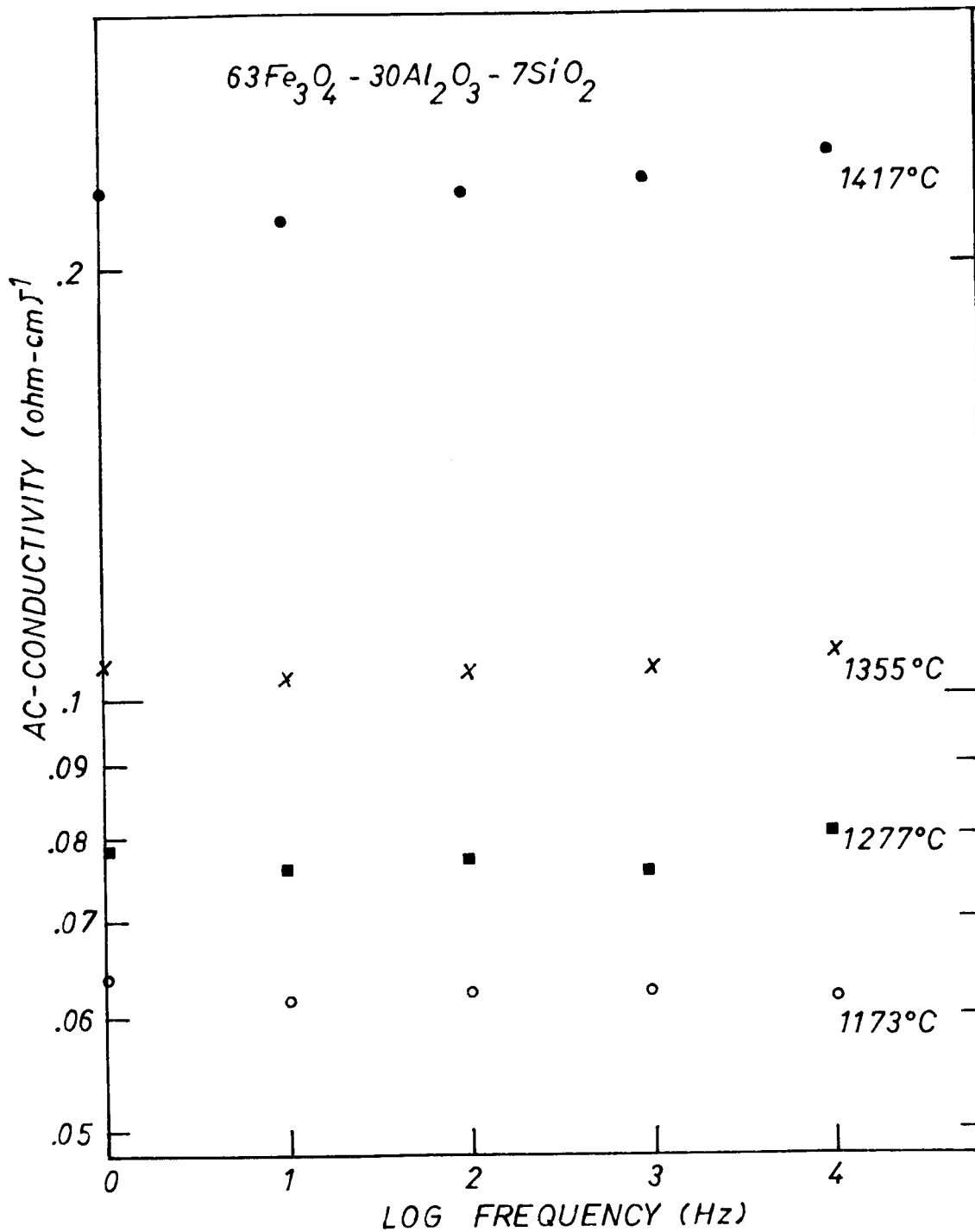


Figure 35. Isothermal ac-conductivity as a function of frequency for composition $63\text{Fe}_3\text{O}_4 - 30\text{Al}_2\text{O}_3 - 7\text{SiO}_2$.

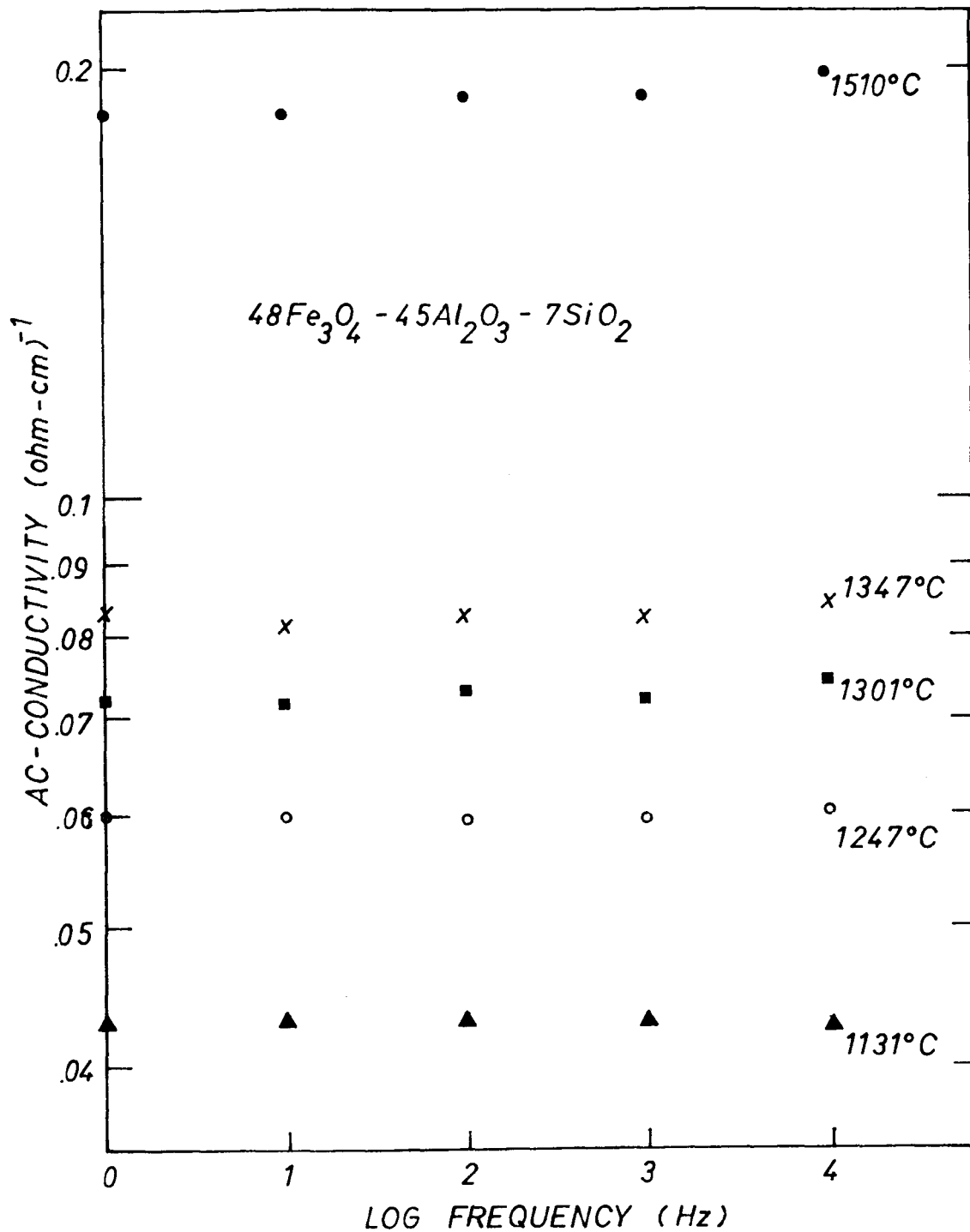


Figure 36. Isothermal ac-conductivity as a function of frequency for composition $48\text{Fe}_3\text{O}_4 - 45\text{Al}_2\text{O}_3 - 7\text{SiO}_2$.

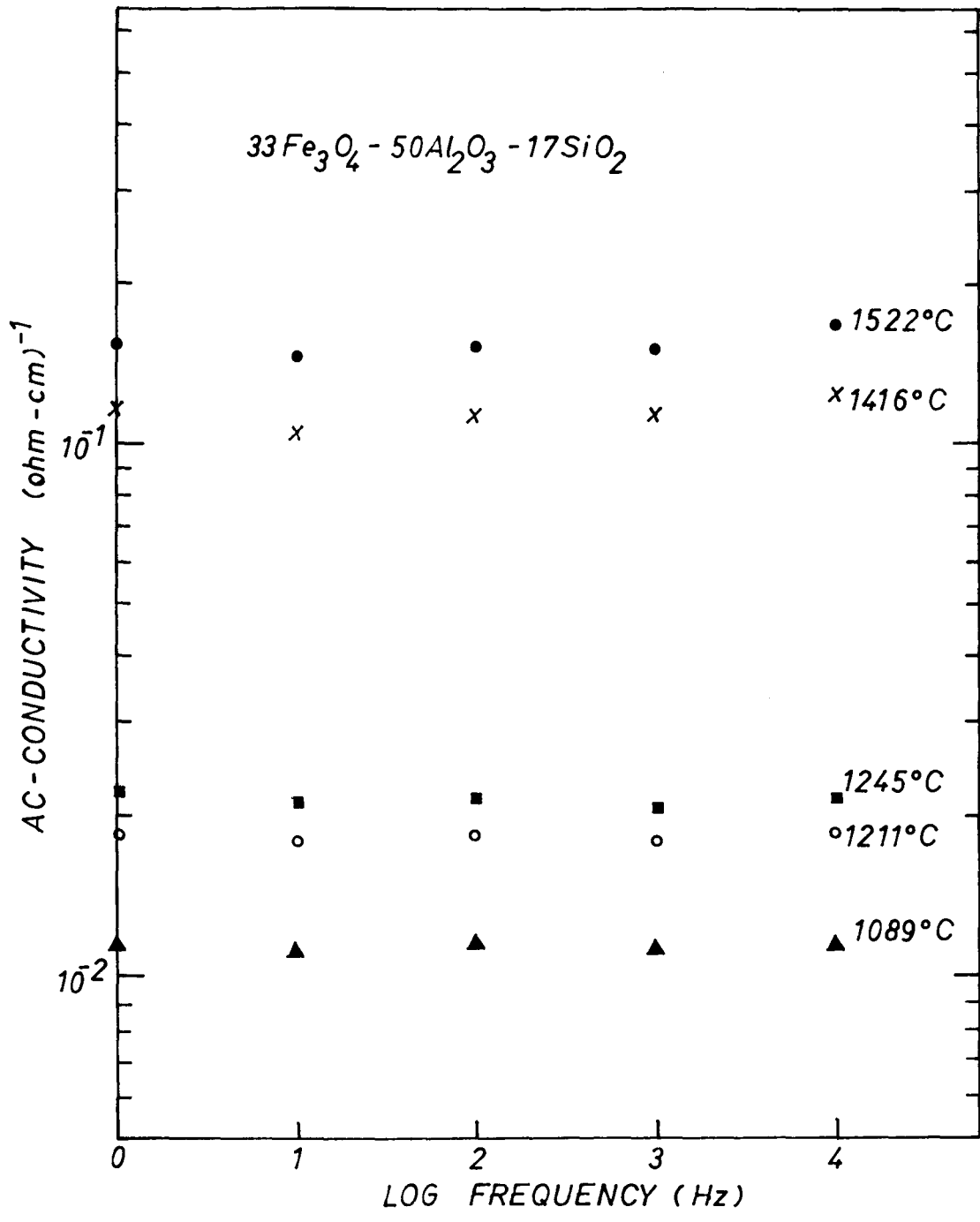


Figure 37. Isothermal ac-conductivity as a function of frequency for composition $33\text{Fe}_3\text{O}_4 - 50\text{Al}_2\text{O}_3 - 17\text{SiO}_2$.

7SiO₂, 43Fe₃O₄-50Al₂O₃-7SiO₂ and 33Fe₃O₄-60Al₂O₃-7SiO₂. The conductivities still displayed the similar three stage dependence on temperature, but with two major distinctions from that described in the previous section.

Figure 38 shows the conductivities of the three samples as a function of temperature. It should be noted that region II established itself at a higher temperature, near 1460°C. Also the activation energies for conduction in the low temperature range (region III) were higher, about 1.2eV.

Also included in Figure 38 was the conductivity result of a rectangular specimen (43F-50A-7S) by a four-point probe technique with a geometric factor of 8.889 cm⁻¹ (dotted line). This was carried out to test the reproducibility of the data from the conductivity cell.

Figure 39 is the microstructure of composition 47F-46A-7S melted and annealed at 1250°C for 24 hours. The morphology is similar to that of composition 63F-30A-7S. It shows spinel grains and corundum platelets in a crystalline mullite matrix. The ac-conductivity of composition 43F-50A-7S at different temperatures was again independent of frequency.

Using Maxwell's model for multiphase conduction, the actual conductivity of the mullite matrix was calculated from each of the compositions and is presented in Figure 40 .

VI.2.3. Conduction via a Corundum Matrix in the Crystalline Composite.

One of the compositions in the triangle s₁m₁c₁ had a high

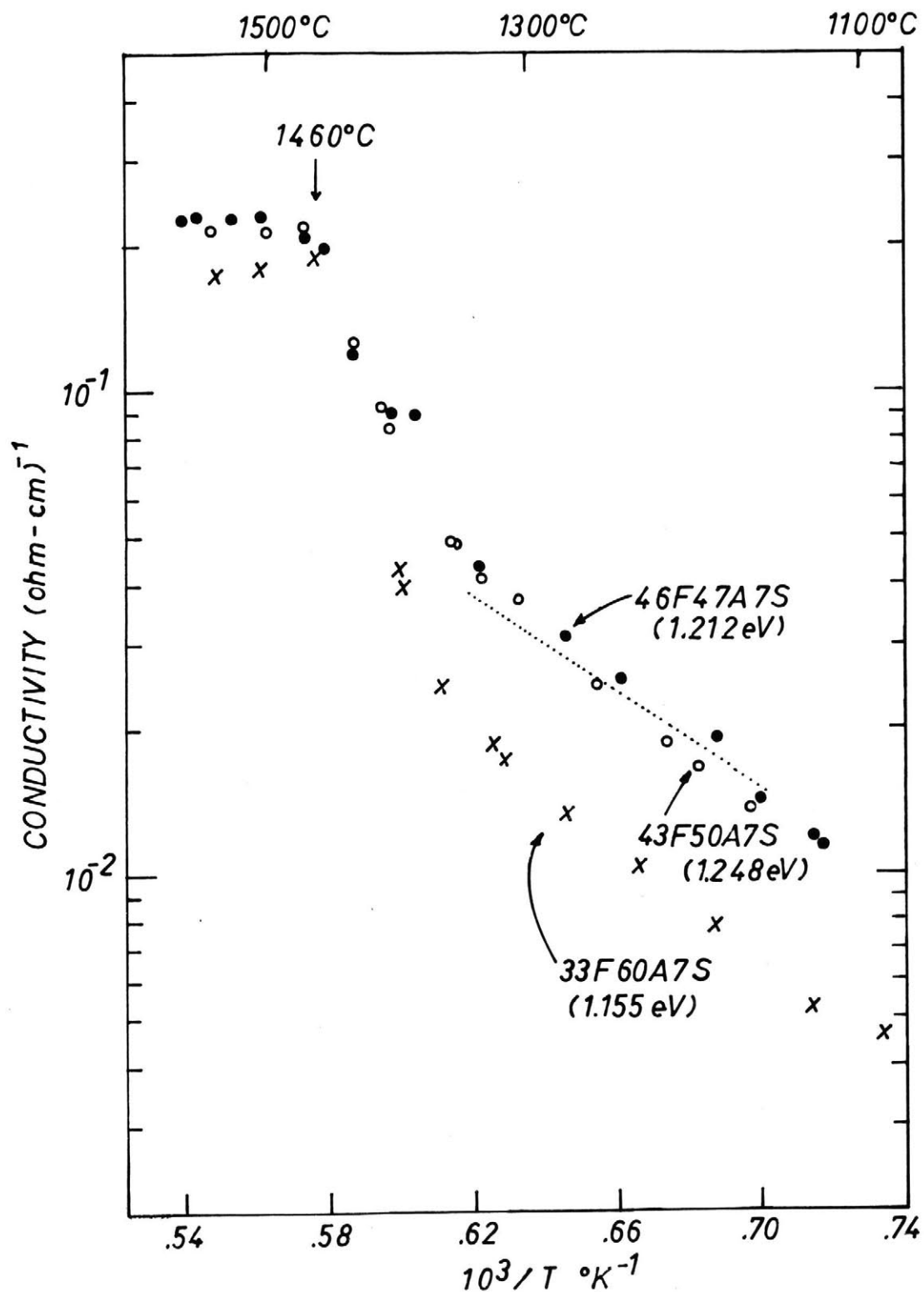
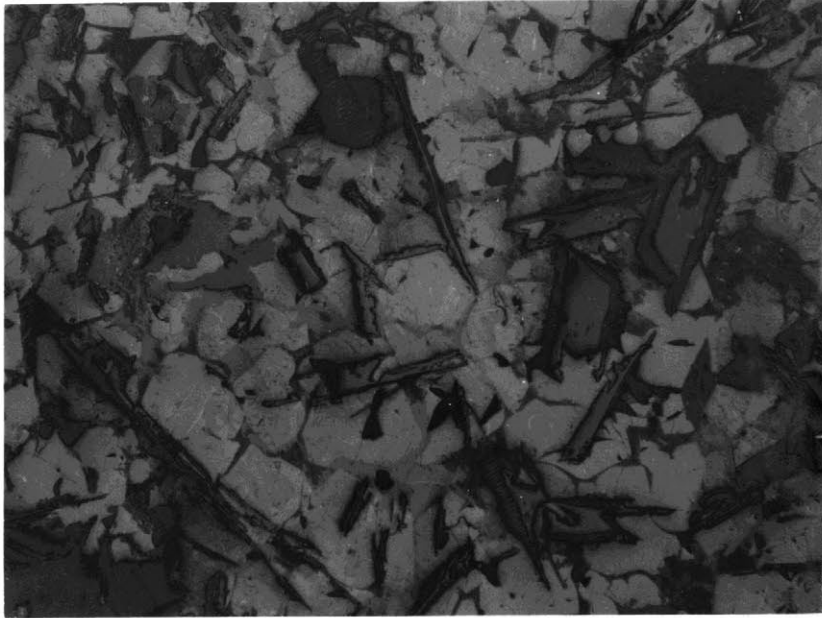


Figure 38. Electrical conductivities as a function of temperature for compositions within the compatible triangle $s_1m_1c_1$.

Spinel grain



Mullite matrix

Corundum
particle

Figure 39. Microstructure of a sample of composition 47F - 46A - 7S annealed in air at 1250°C for 24 hours. (Magnification 100x)

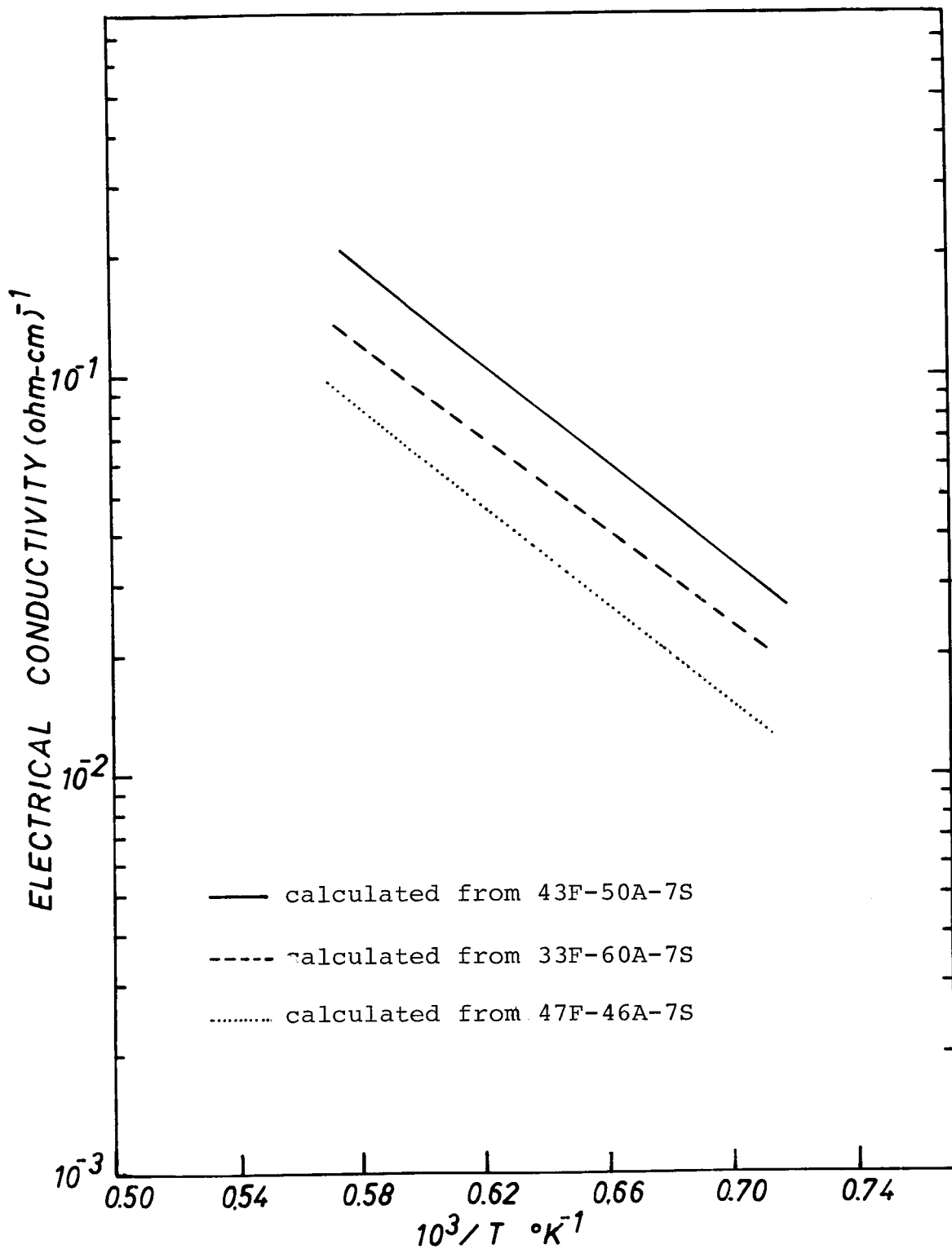


Figure 40. The calculated electrical conductivity of mullite of composition 13.09 w/o Fe_2O_3 , 61.4 w/o Al_2O_3 , 25.5 w/o SiO_2 .

enough alumina content that the corundum phase became the matrix of the solid aggregate. This difference in the microstructure led to a unique conductivity-temperature dependence.

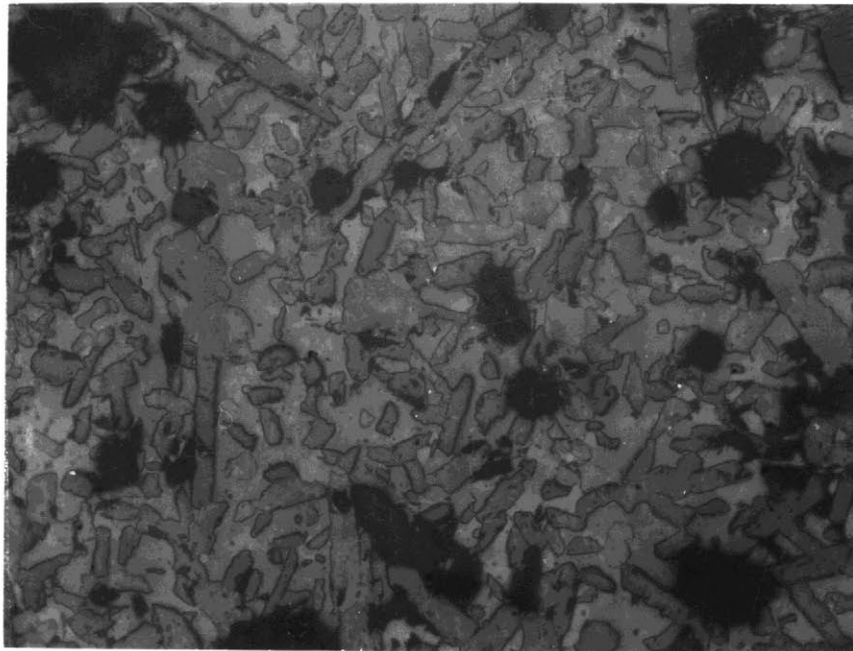
Figure 41 is the microstructure of a sample of this composition, $23\text{Fe}_3\text{O}_4-70\text{Al}_2\text{O}_3-7\text{SiO}_2$ partially melted at 1550°C and annealed at 1250°C for a day. The acicular shaped grain was mullite (11.63 w/o Fe_3O_4 62.79w/o Al_2O_3 25.57w/o SiO_2) in a matrix of corundum containing 7.37w/o Fe. Because of the high alumina content, the corundum grains formed an interconnecting network before the last melt solidified. As the sample was only partially melted, empty voids occupied a fair volume fraction.

The dc-conductivity data in Figure 42 revealed a drop of over two orders of magnitude upon solidification. Between 1550°C and 1460°C the conduction was through an iron aluminosilicate melt saturated with corundum and mullite. The conductivity decreased with temperature as corundum and mullite shared a greater portion of the melt. The activation energy for conduction via the corundum phase below 1460°C was 2.97eV.

Polarization effects were observed during the dc-conductivity measurements on the solid sample. When the current was first applied to the sample, it sustained a higher instantaneous conductivity. This then levelled off to the steady state dc-value in a time span of 45-60 min.

Mullite grain

void



Corundum matrix

Figure 41. Microstructure of a sample of composition 23F-70A-7S annealed in air at 1250°C for 24 hours. (Magnification 200x)

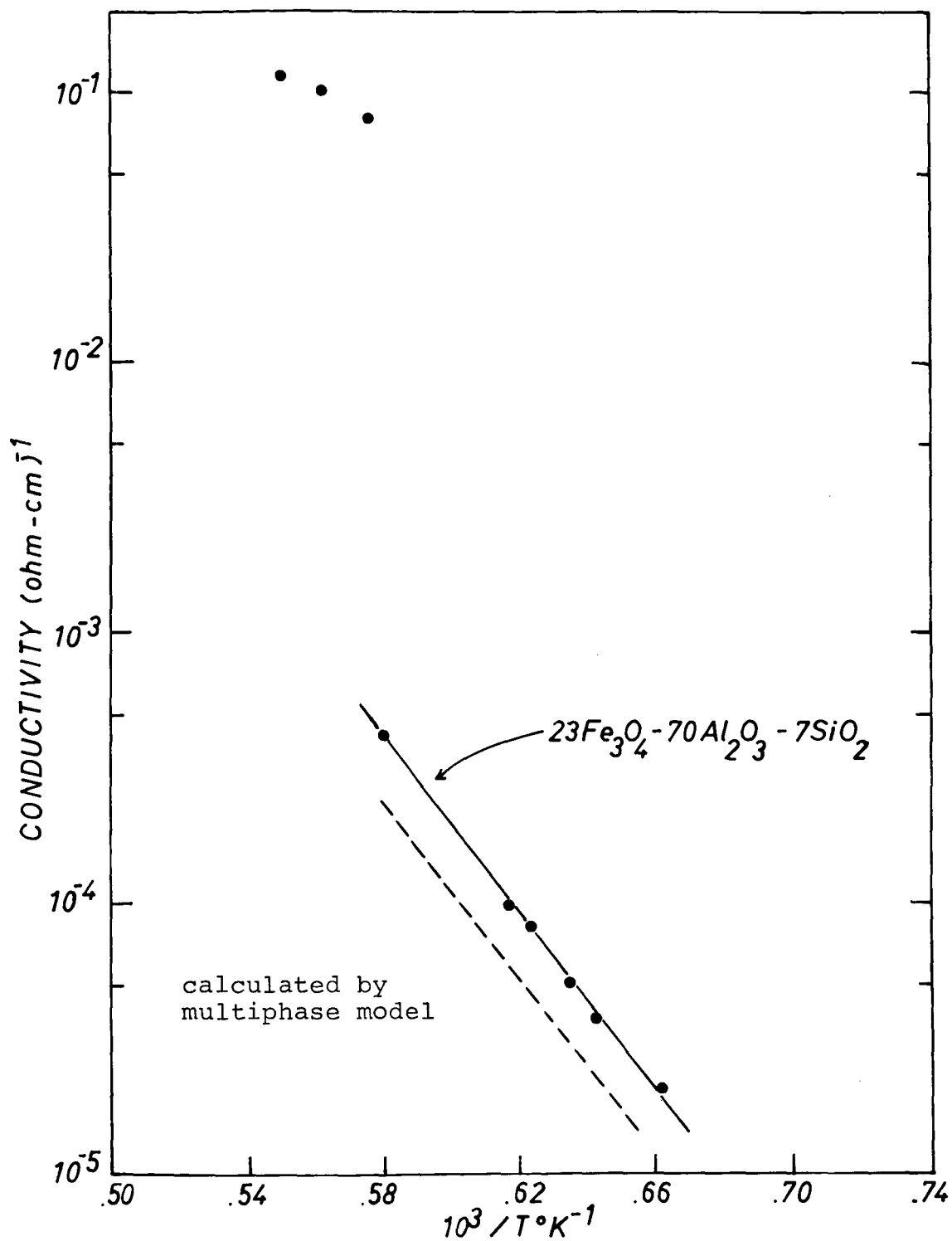


Figure 42. Electrical conductivity as a function of temperature for composition 23Fe₃O₄-70Al₂O₃-7SiO₂.

Using the point counting technique, the volume fractions of corundum, mullite and void were obtained. Applying Maxwell's equation for the matrix conductivity, the conductivity of the iron-doped alumina phase (7.37w/o Fe) was

$$\sigma_{\text{corundum}} = 0.541 \sigma_{\text{sample}}$$

The calculated conductivity was included in Figure 42 (dashed line).

It has been documented that for all compositions with a high iron oxide content, the ac-conductivity was equivalent to the dc-value within the temperature range studied. However, such was not the case for 23F-70A-7S (Figure 43). The ac-data at 1544°C, where the conduction was through the melt, only showed slight enhancement with increasing frequency. But the data in the solid state were dependent on the measuring frequency. The increase in total conductivity over the dc-value was attributed to the contribution from ionic species.

VI.2.4. Electrical Conductivity of Iron Aluminosilicate Melts.

The conductivity of the iron aluminosilicate melts (region I) presently studied did not conform to the Arrhenius equation. It has a complicated dependence on temperature.

In region I of the conductivity results, the equilibrium phases present were a melt coexisting with spinel, corundum, and/or mullite. The relative volume fraction and composition of each depended on the temperature and the location of the

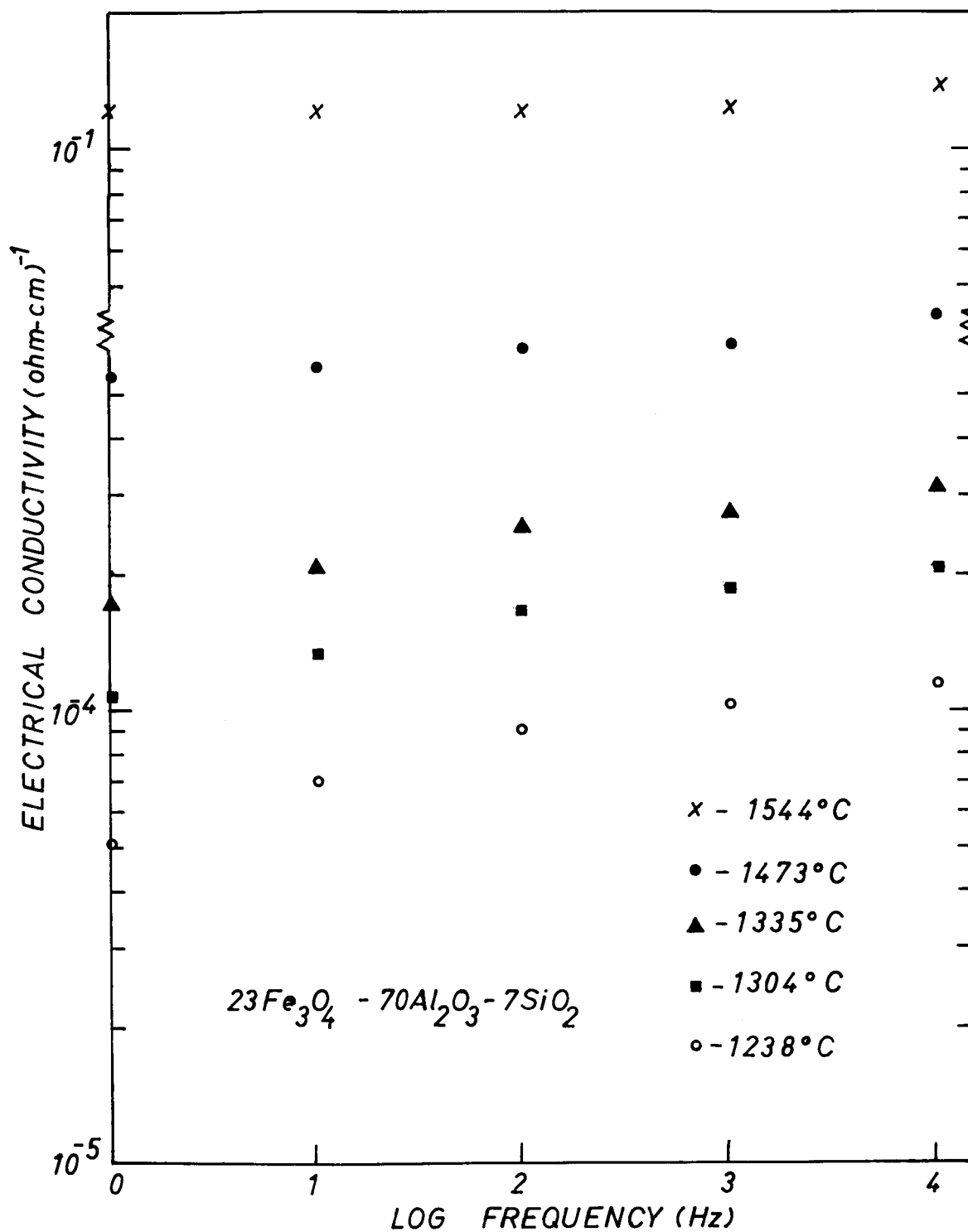


Figure 43. Isothermal ac-conductivity as a function of frequency for composition $23\text{Fe}_3\text{O}_4 - 70\text{Al}_2\text{O}_3 - 7\text{SiO}_2$.

overall composition in the $\text{FeO}\cdot\text{Fe}_2\text{O}_3\text{-Al}_2\text{O}_3\text{-SiO}_2$ system. Figure 44 is a micrograph of a sample of composition 63F-30A-7S quenched from 1495°C where the melt was saturated with spinel and corundum. The sample was sectioned vertically to see if there was any phase segregation. The micrograph showed that the spinel grains formed a layer at the top of the melt. A layer of corundum particles rested underneath it. The melt, of approximate composition 38w/o Fe_2O_3 19w/o FeO 27w/o Al_2O_3 16w/o SiO_2 , was at the bottom of the crucible. Again the fine dendritic structure was a result of spinel-formation during quenching.

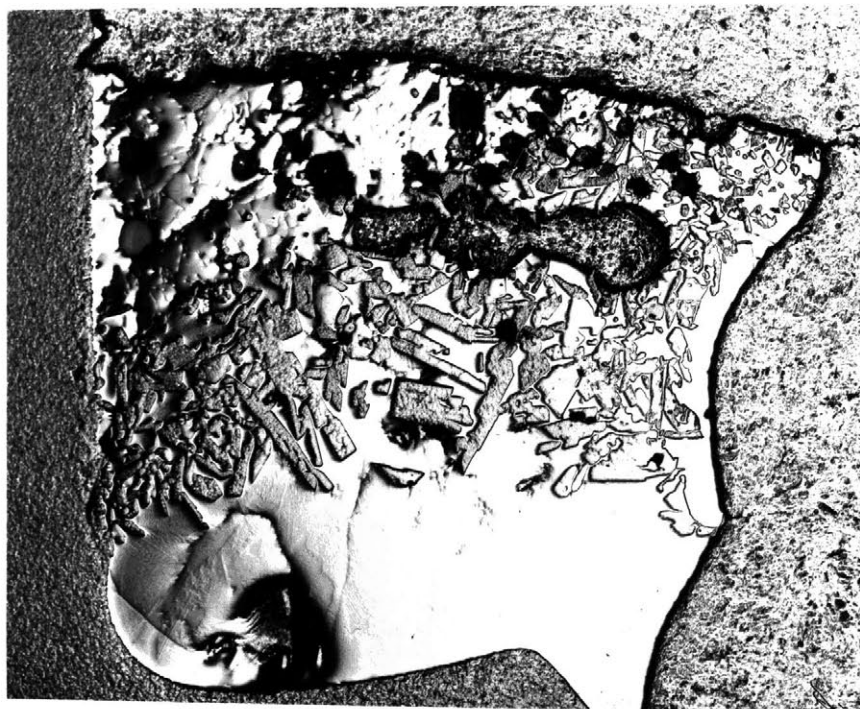
The conductivity cell was designed such that the platinum electrodes were about 3 mm above the bottom of the alumina crucible. The melt in the crucible was filled to a depth of at least 20 mm. So it would be safe to conclude that at sufficiently high temperatures when the solid phases occupied a small volume fraction, the conductivity measured would be that of the melt itself.

Figure 45 is a plot of the dc-conductivity at 1550°C as a function of the overall sample composition. It should be noted that even though the conductivity increased with the iron content, the change was not large. Points c_1 , c_2 , and c_3 actually represented the same melt on the spinel-corundum-melt phase boundary. This meant that the conductivities those of melts of the same composition but each with different volume fractions of corundum and spinel. The fact that the

Spinel grain

Corundum particle

Crucible



Quenched Melt

Figure 44. The microstructure of a sample of composition $63\text{Fe}_3\text{O}_4-30\text{Al}_2\text{O}_3-7\text{SiO}_2$ quenched from 1495°C in air, showing the segregation of phases.

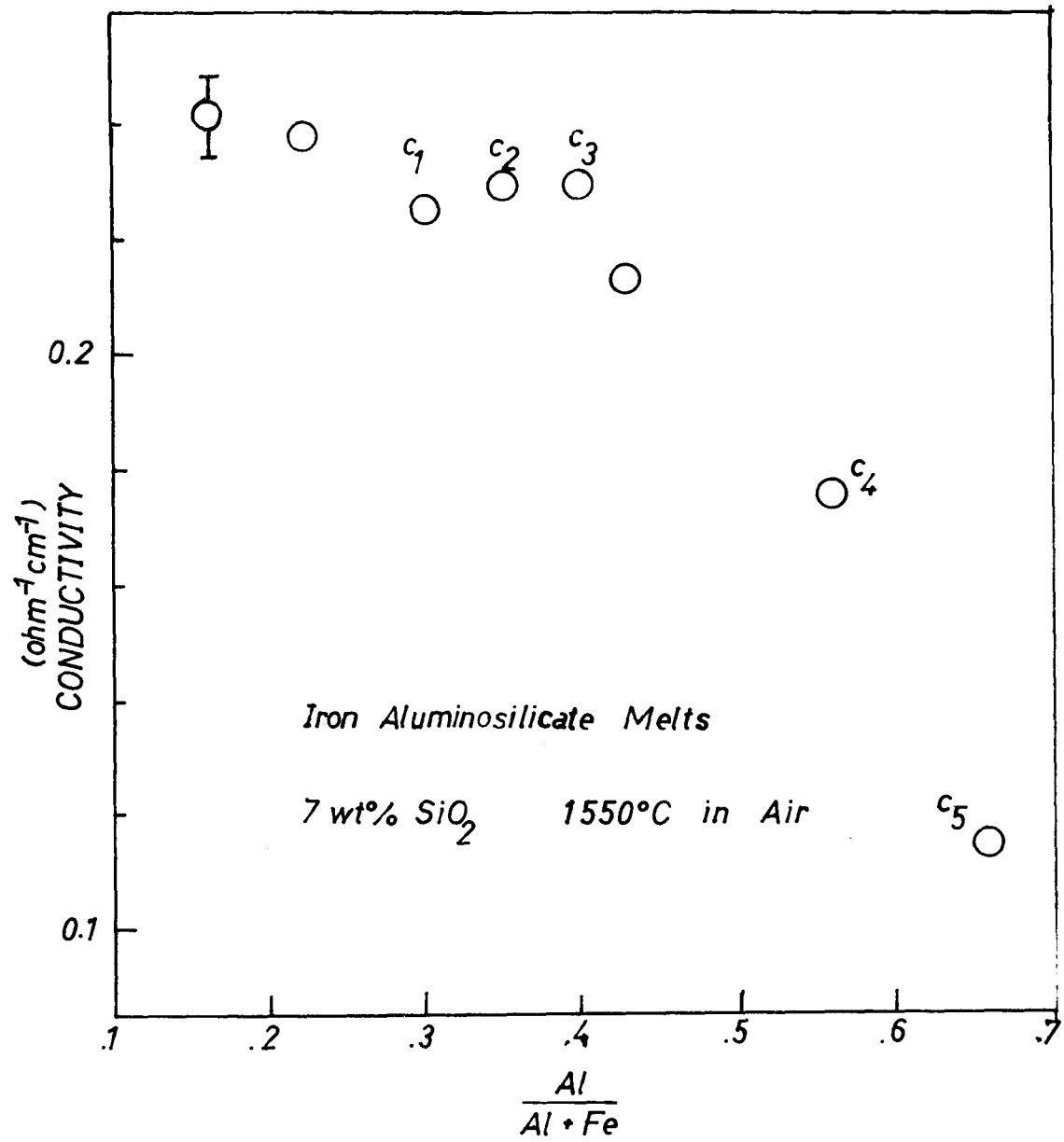


Figure 45. Isothermal electrical conductivity in air at 1550°C as a function of composition.

conductivities were identical within experimental error supports the argument mentioned in the last paragraph.

However, such was not the case for points c_4 and c_5 . Here, the volume fraction of corundum was over 60%. Hence the conductivities measured were an effective value for corundum particles suspended in an iron aluminosilicate melt.

Figure 46 is a plot of $\log \sigma T/c(1-c)$ versus reciprocal temperature for five compositions, where c is the $\text{Fe}^{3+}/\text{Fe}_{\text{total}}$ ratio.

VI.3. Isothermal Electrical Conductivity of Iron Aluminosilicate Melts as a Function of Oxygen Partial Pressure.

The isothermal conductivity of melts was measured as a function of oxygen partial pressure. For the curves presented in Figure 47 the equilibrium phases in air consisted of spinel or corundum particles in the melt. As the oxygen partial pressure was lowered, the compositions and volume fractions of the solid and molten phases changed according to the phase equilibria of the system. The partial pressure dependence was very similar to that of other silicate melts (Figure 9). The electrical conductivity decreased with decreasing oxygen partial pressure at the low P_{O_2} range while for intermediate P_{O_2} , the conductivity was insensitive to any change in P_{O_2} .

A study of the isothermal conductivity of melts at a temperature above the liquidus surface could eliminate any problem posed by the presence of the solid phase. The melt

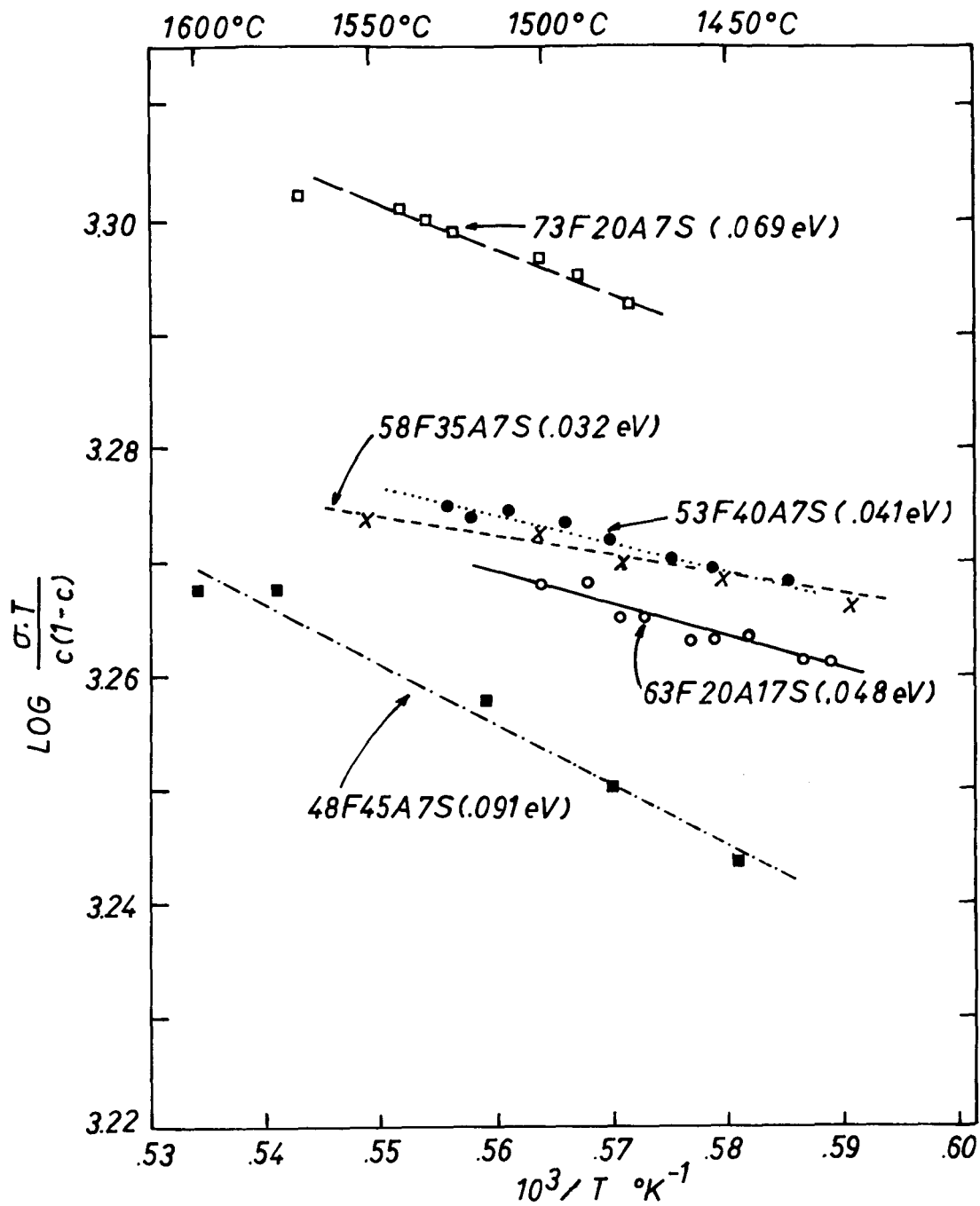


Figure 46. Plot of $\log \frac{\sigma \cdot T}{c(1-c)}$ versus reciprocal temperature for iron aluminosilicate melts.

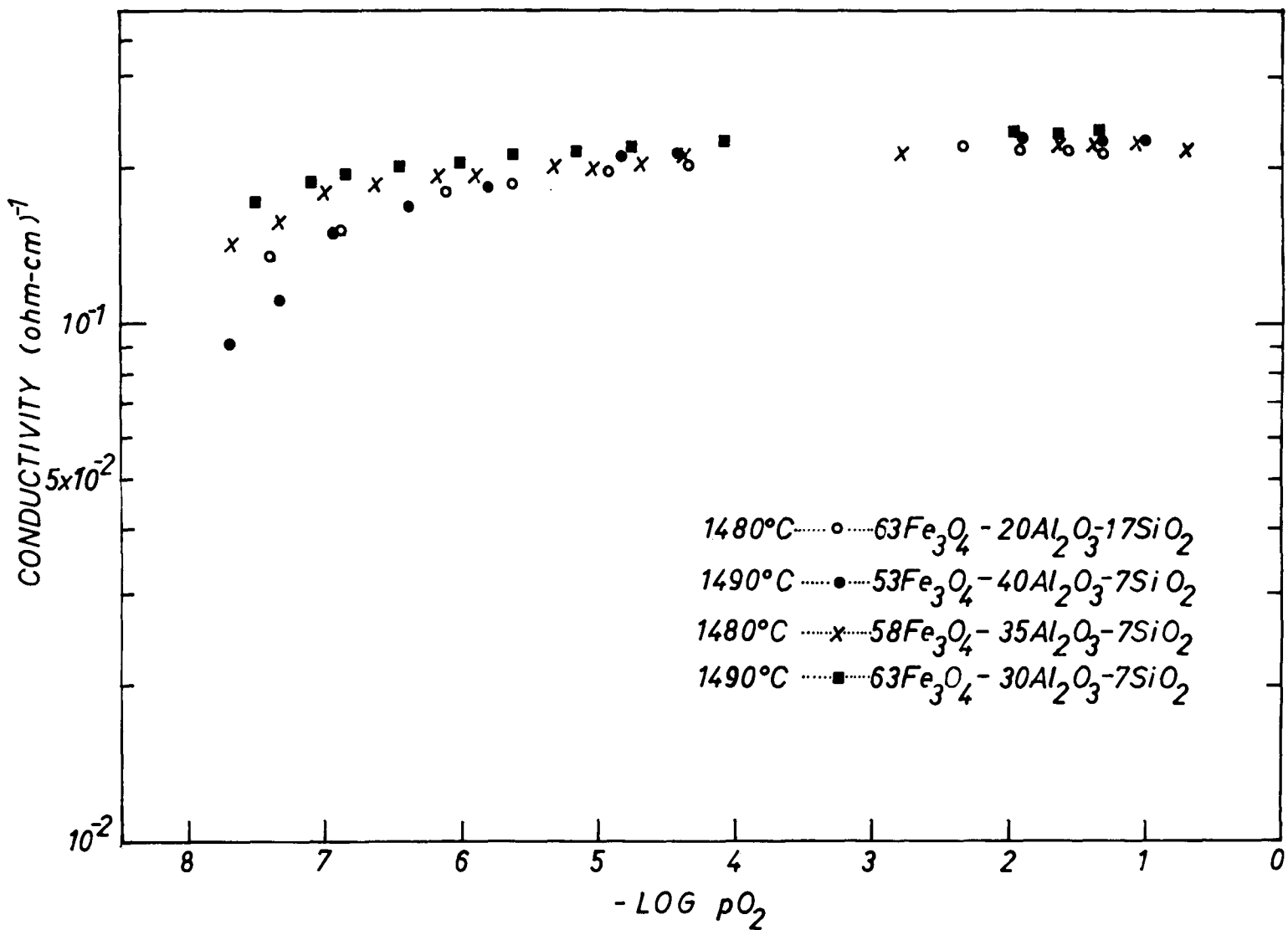


Figure 47. Isothermal dc-conductivity as a function of oxygen partial pressure for iron aluminosilicate melts.

would remain single-phase over a range of oxygen partial pressure. Bringing the melt to equilibrium with oxygen at a given P_{O_2} meant that the Fe^{3+}/Fe^{2+} ratio, hence the $c(1-c)$ term, was adjusted without any accompanying change in the total iron, alumina and silica content. Figure 48 presents the isothermal results above the liquidus temperature.

Figure 49 shows the conductivities plotted against Fe^{3+}/Fe_{total} ratio. For the compositions with 7 wt% SiO_2 , the conductivities peaked at $c = 0.67$. For the composition 63F-20A-17S the maximum was at $c = 0.55$.

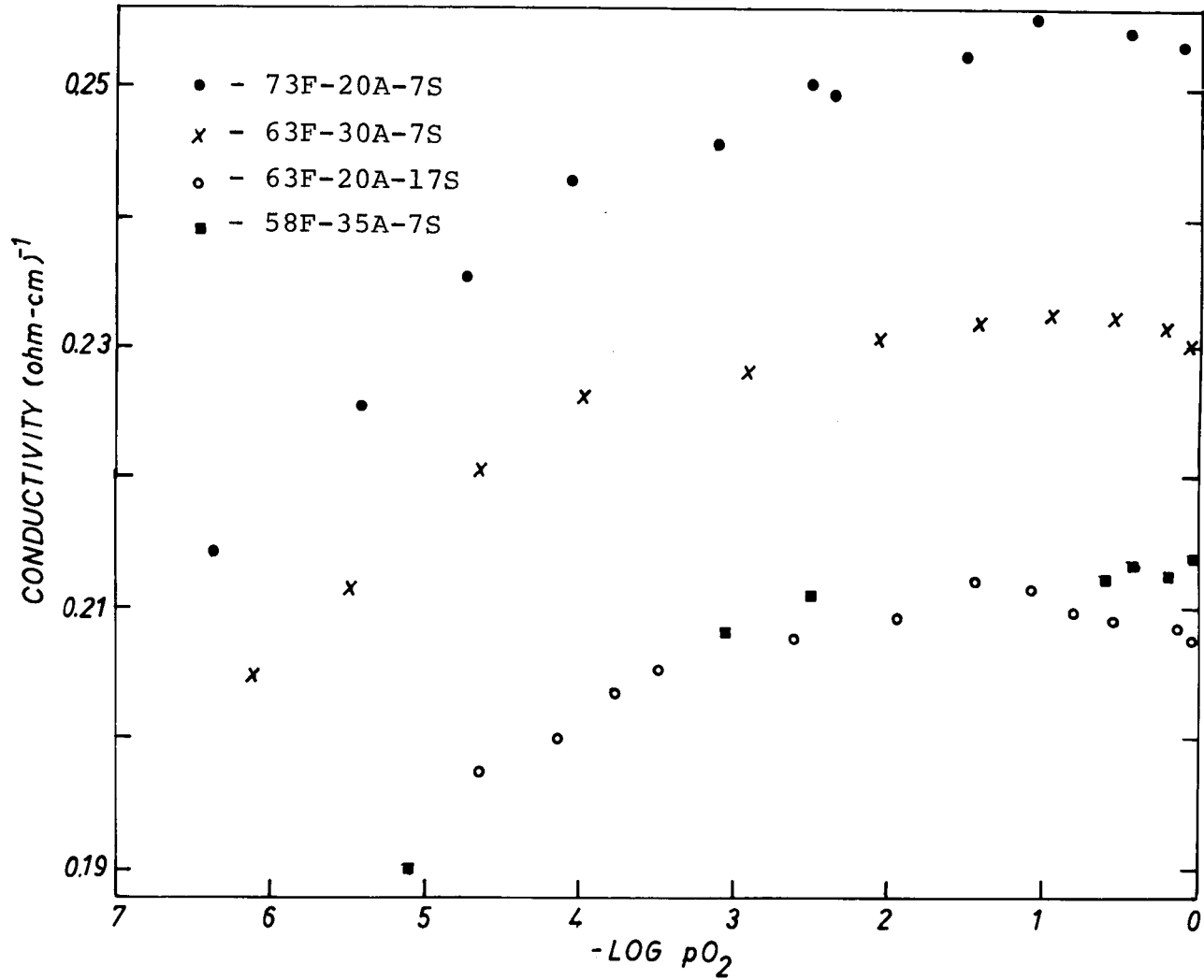


Figure 48. Isothermal dc-conductivity as a function of oxygen partial pressure for iron aluminosilicate melts above the liquidus temperature.

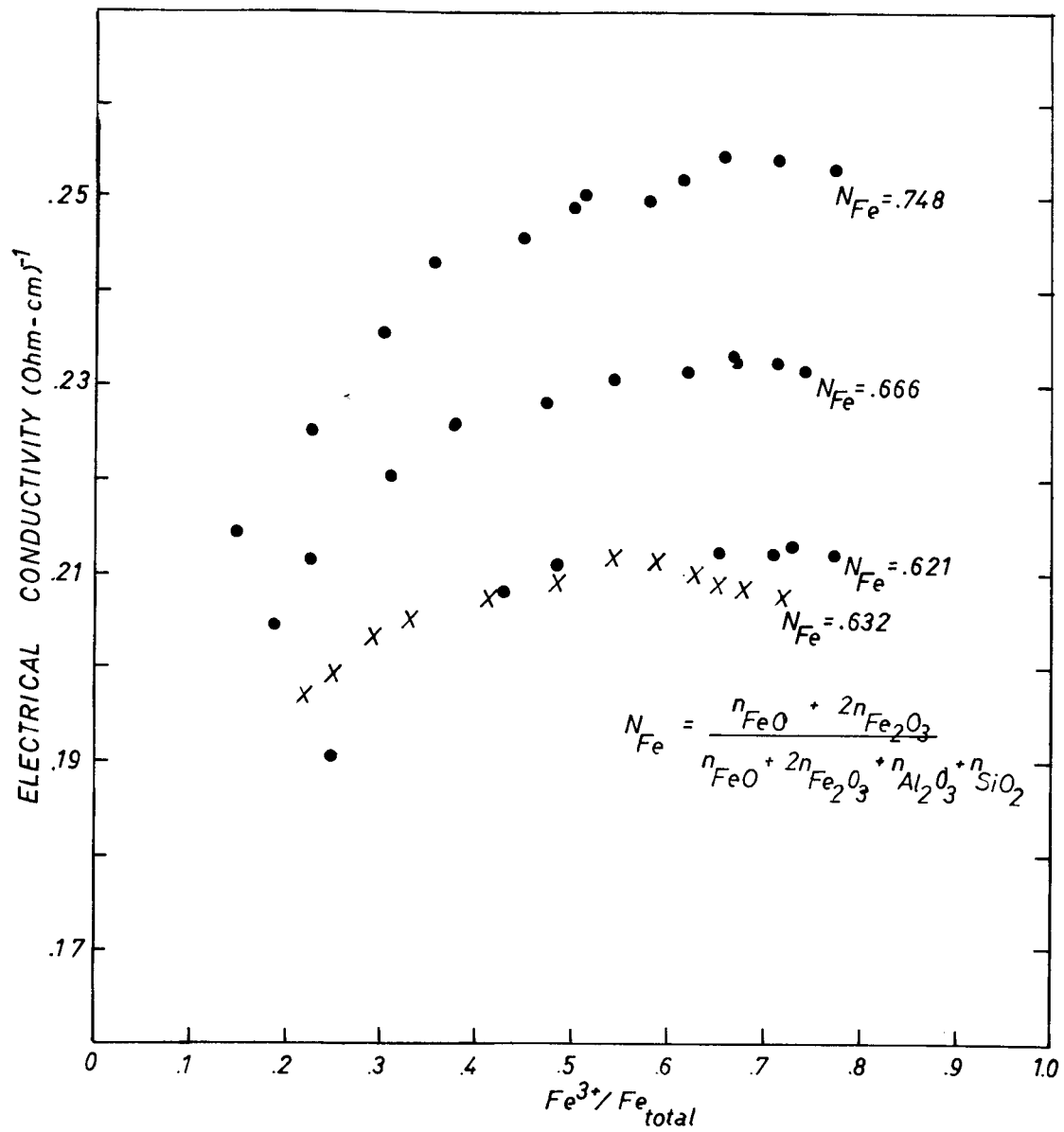


Figure 49. Isothermal dc-conductivity as a function of Fe^{3+}/Fe_{total} ratio in iron aluminosilicate melts.

Chapter VII . Discussion

The primary thrust of this research effort has been to understand the electrical conductivity in the $\text{FeO}\cdot\text{Fe}_2\text{O}_3\text{-Al}_2\text{O}_3\text{-SiO}_2$ system as a function of composition, temperature and oxygen partial pressure. In this chapter, the results will first be related to the phase chemistry of the system. The possible conduction mechanisms in the solid and molten states will also be discussed.

The compositions studied showed four basic types of conductivity-temperature dependence in air. These four classes of conductivity behavior can conveniently be differentiated according to where the composition is located in the ternary system. The conductivity of the three compositions inside the compatibility triangle $\text{SiO}_2\text{-s}_2\text{-m}_2$ of Figure 50 increased with decreasing temperature without any observable discontinuity upon solidification. The rest of the compositions investigated were within the $\text{s}_1\text{s}_2\text{m}_2\text{m}_1$ quadrilateral and the $\text{s}_1\text{m}_1\text{c}_1$ compatibility triangle. The temperature dependence of their electrical conductivity typically had three stages. At high temperatures, where an iron aluminosilicate melt was in equilibrium with spinel, corundum and/or mullite, the conductivity was rather insensitive to temperature. Upon solidification with further cooling, there was a sharp discontinuity in electrical conductivity. For the composition with 23 w/o Fe_2O_3 , the drop in conductivity at 1460°C was over two orders of magnitude. The thermal activation energies for

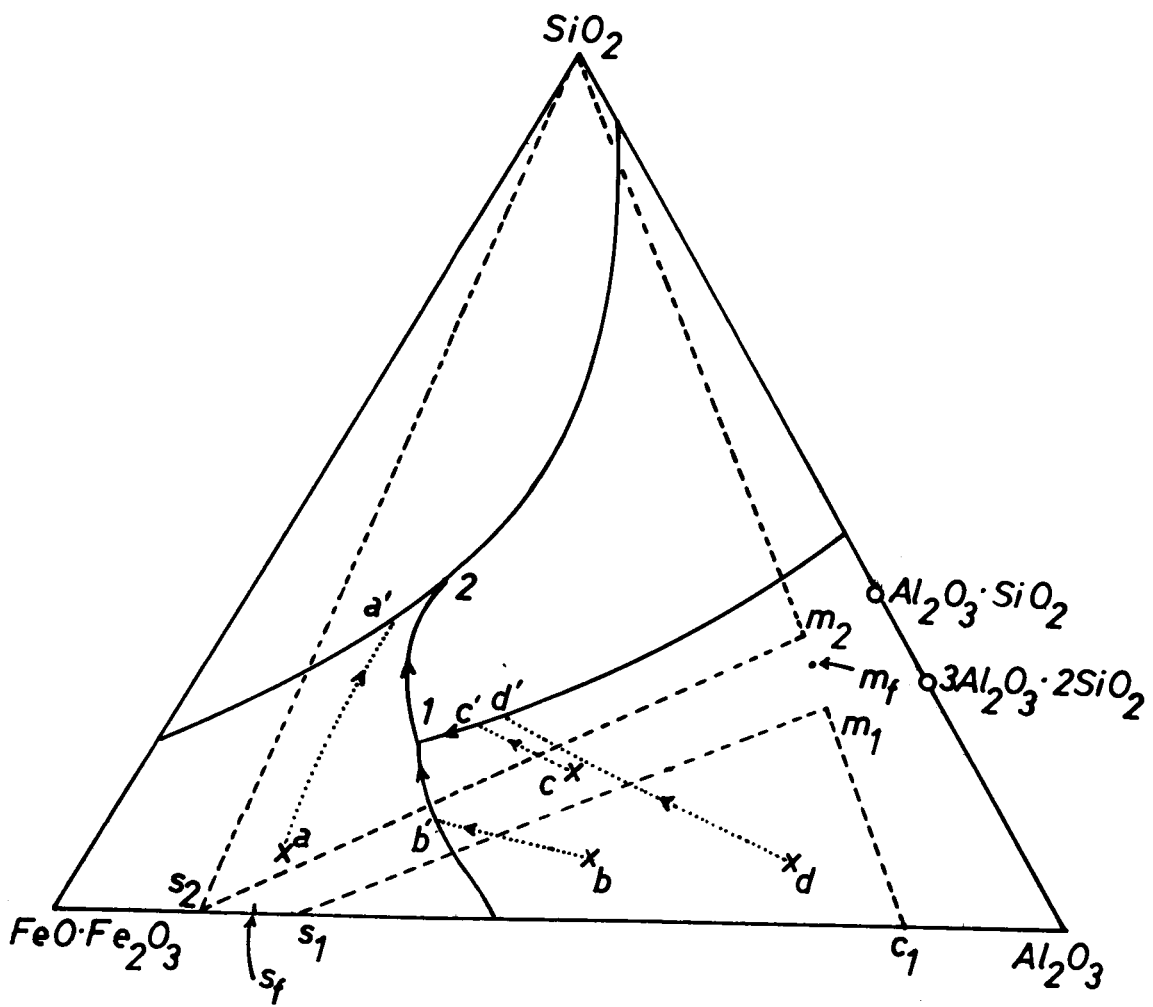


Figure 50. Illustration of several crystallization sequences in the $\text{FeO}\cdot\text{Fe}_2\text{O}_3$ - Al_2O_3 - SiO_2 system.

conduction in the final crystallization products of the compositions within the $s_1s_2m_2m_1$ area varied from 0.393 to 0.623eV. The conductivity of three compositions inside $s_1m_1c_1$ have thermal activation energies of 1.155, 1.212 and 1.248eV while an activation energy of 2.97eV was measured for the composition in the same compatibility area that contained 23w/oFe₃O₄.

The properties of a multicomponent system such as FeO·Fe₂O₃-Al₂O₃-SiO₂ are controlled by the phases in equilibrium. Therefore one must revert to a detailed understanding of the phase chemistry in order to comprehend the complicated conductivity-temperature dependence. In the following, the association between the electrical conductivity and crystallization sequence of different compositions is discussed, using Figure 50 as an illustration.

The composition 73Fe₃O₄-20Al₂O₃-7SiO₂ (point "a" in Figure 50) is representative of compositions in the SiO₂-s₂-m₂ compatibility triangle. Below 1600°C, spinel starts to crystallize out of the melt. As the temperature is lowered, the equilibrium spinel composition continues to be enriched in magnetite and the crystallization proceeds along the dotted line aa'. The volume fraction of spinel of composition 63Fe₃O₄-38FeAl₂O₄ is about one-third at 1550°C. At about 1390°C, the crystallization path reaches a' on the liquid-spinel-tridymite boundary. Here the last liquid disappears.

While phase equilibria predicts that the final crystallization product should be a mixture of spinel, mullite and

tridymite, Debye-Scherrer diffraction patterns failed to reveal any peaks characteristic of mullite or tridymite. Optical micrographs showed that the solid state aggregate was composed of large spinel grains imbedded in a matrix. The large spinel grains were found to be of the same composition. However, further x-ray diffraction studies revealed that at least two more different spinel compositions were present. The electron microprobe analysis also indicated that the matrix was inhomogeneous. The average matrix composition was 70.5w/o FeO, 21.5w/o Al₂O₃, 69.13w/o SiO₂, with the silica content varying from 53.54 to 76.27w/o. This was not representative of any stoichiometric composition. Judging from the broadening of the diffraction peaks, there were submicron spinel crystallites present. Given this evidence, it was concluded that the matrix of the 73Fe₃O₄-20Al₂O₃-7SiO₂ sample was made up of residual iron aluminosilicate glass with fine spinel crystallites.

The conductivity of this composition increased with decreasing temperature between 1380° and 1100°C. The magnitude of the conductivity ruled out the possibility that the conduction was through interconnected large spinel grains. If it were so, the electrical conductivity would be of the order of 10-100 ohm⁻¹.cm⁻¹, i.e., at least two to three orders of magnitude higher. The results were reproducible by different means as described in Chapter VI. The plausible explanation is multi-phase conduction in a microstructure with large spinel grains

imbedded in a matrix of glass with fine crystallites.

The effect of iron oxide content on the conductivity and thermal activation energy of a glass has been reported by others. Trap and Stevels⁴⁵ added 15 m/o Fe_3O_4 to a batch of glass with composition 24 m/o Na_2O , 12 m/o Al_2O_3 , 3 m/o CaO , 3 m/o SrO , 40 m/o SiO_2 . The conductivity of the resulting glass was $1.09 \times 10^{-3} \text{ ohm}^{-1} \cdot \text{cm}^{-1}$ with a thermal activation energy of 0.075eV. If 18 m/o Fe_3O_4 was added, the conductivity increased to $2.75 \times 10^{-3} \text{ ohm}^{-1} \cdot \text{cm}^{-1}$ and the activation energy became 0.061eV. The conductivity was drastically reduced to $6.6 \times 10^{-6} \text{ ohm}^{-1} \cdot \text{cm}^{-1}$ while the activation energy increased slightly, to 0.103eV, if only 12 m/o Fe_3O_4 was added.

Since the conductivity measured in this study for composition $73\text{Fe}_3\text{O}_4-20\text{Al}_2\text{O}_3-7\text{SiO}_2$ remained between 0.2 and 0.3 $\text{ohm}^{-1} \cdot \text{cm}^{-1}$ between 1380° and 1100°C, using an average value for the iron content in the matrix, the charge carrier mobility could be estimated. Assuming that the free charge carrier is ionized from the iron present in the glass, taking the iron content to be the maximum possible value (5.7 w/o) and using a density of 3.0 gm/cm^3 for the glass, the calculated minimum mobility is of the order of $7.5 \times 10^{-4} \text{ cm}^2/\text{v} \cdot \text{sec}$. Such a low carrier mobility suggests that a conduction mechanism other than the band model is in operation. However, this speculation relies on the validity of the assumption that all iron ions are involved in the conduction process.

Even though plots of $\log_{10} \sigma \cdot T$ versus reciprocal temperature are linear for the compositions $73\text{Fe}_3\text{O}_4-20\text{Al}_2\text{O}_3-7\text{SiO}_2$ and $53\text{Fe}_3\text{O}_4-30\text{Al}_2\text{O}_3-7\text{SiO}_2$ (Figures 24 and 25), with activation energies of 0.0643 and 0.0547eV, respectively, the exact conduction mechanism cannot be identified unambiguously. Additional information on the precise variation of the free charge carrier concentration with temperature is essential in concluding whether the conduction is best represented by the conduction band model or by a thermally activated hopping process. Because of the small conductivity-temperature dependence, a plot of $\log \sigma T^{3/2}$ versus reciprocal temperature also has a linear relationship.

The composition $43\text{Fe}_3\text{O}_4-40\text{Al}_2\text{O}_3-17\text{SiO}_2$ (point "c" in Figure 50) is chosen as an illustration for the compositions inside the $s_1s_2m_2m_1$ region. This composition is a liquid above 1675°C. Corundum (ss) is the first crystalline phase to precipitate as the temperature is lowered. The crystallization proceeds along the locus cc'. At about 1500°C, the liquid-mullite-corundum boundary is reached (point c'). The crystallization now follows the boundary to point "1" at 1460°C where the liquid is in equilibrium with spinel, mullite and corundum. At "1", corundum is resorbed and the crystallization continues, progressing along the liquid-spinel-mullite boundary towards point "2". As this occurs the spinel composition in equilibrium with the melt and mullite changes from s_1 towards s_2 . The mullite composition simultaneously alters from m_1 towards m_2 .

At about 1400°C, the spinel and mullite compositions in equilibrium with the melt are s_f and m_f , respectively. The points s_f , m_f and c lie on a straight line. The last liquid disappears at this temperature, leaving behind a crystallization product of spinel and remnant corundum grains in a mullite matrix.

The last liquids disappear in the vicinity of 1390-1400°C for all the compositions studied in the $s_1s_2m_2m_1$ region. This is, in all cases, accompanied by the succession of region II in the conductivity-temperature data.

The measured electrical conductivity for the composite structure was the conductivity through the mullite matrix with small contributions from the spinel grains present. But in as much as the silicate wets the corundum and spinel grains, few of the spinel grains would form enough contact area to allow a major fraction of the current just through spinel (or corundum). As the mullite composition (m_f) in the final crystallization composite varies according to each overall composition, the change in the thermal activation energy (0.393 to 0.623eV) is consistent with decreasing iron content. This evidence strongly indicates a direct correlation between the conductivity-temperature dependence and the phase chemistry of the $FeO \cdot Fe_2O_3 - Al_2O_3 - SiO_2$ system.

The composition $43Fe_3O_4 - 50Al_2O_3 - 7SiO_2$ (point "b" in Figure 50) inside the $s_1m_1c_1$ compatibility triangle follows the crystallization curve bb' . Spinel of approximate composi-

tion $53\text{Fe}_3\text{O}_4-47\text{FeAl}_2\text{O}_4$ appears at 1500°C (point b'). The liquid-spinel-mullite boundary is followed until point "1" is reached. Unlike the compositions inside the $s_1s_2m_2m_1$ region, the last liquid vanishes here. The crystallized composite contains spinel(s_1) and corundum(c_1) grains in a mullite(m_1) matrix.

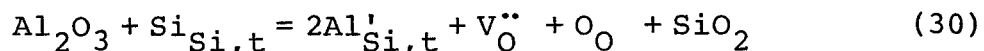
The junction between regions I and II of the conductivity-temperature data was at 1460°C for compositions within the $s_1c_1m_1$ triangle. This was in contrast to a temperature of about 1390°C observed for the compositions inside $s_1s_2m_2m_1$.

The conductivity in the solid state was again through the mullite matrix of the multiphased aggregate. However, the mullite composition(m_1) is fixed, regardless of the overall composition. Only the relative volume fraction of each phase was affected. Thus, the observed thermal activation energies do not vary as much and were 1.155, 1.212 and 1.248eV for iron-mullite of composition m_1 .

Because mullite has a disordered structure intermediate between sillimanite and andalusite, it is difficult to interpret the conductivity results and indentify the defects responsible for the conduction mechanism. The probelm is further compounded by the variations in the $\text{Fe}/(\text{Fe}+\text{Al})$ and $\text{Si}/(\text{Fe}+\text{Al})$ ratios. Besides the defects inherent in the mullite structure, the partial replacement of Al by Fe ions create those extrinsic in nature. Iron is present mainly in the trivalent state. Mossbauer spectroscopy^{37,38} indicates a preference for

the octahedral coordination.

The mullite compositions in the present study have (Fe+Al)/Si ratios of 3.28 and above, as compared to a normal ratio of 3 for stoichiometric mullite. In view of this excess of Al and Fe ions and the randomness on the Al and Si tetrahedra, point defects such as $Al'_{Si,t}$, $Al'''_{i,t}$, $V'''_{Al,t}$, $Si_{Al,t}$, $Si'''_{i,t}$, $V'''_{Si,t}$, $Al'''_{i,o}$, $V'''_{Al,o}$, $Fe_{Al,o}$ and $Fe'_{Al,o}$ can be visualized.* If the mullite structure is regarded as one with a fixed cation to oxygen ratio, any excess in Al at the expense of Si leads to the creation of oxygen vacancies, V''_O , in order to satisfy the charge and mass balance.



For the iron-mullite composition (m_1): 13.09w/o Fe_2O_3 61.37w/o Al_2O_3 25.53w/o SiO_2 , the calculated oxygen vacancy fraction is of the order of 6×10^{-3} . Since one-third of the Al cations are involved in the tetrahedral network and if one considers that the Fe ions prefer the octahedral coordination, the fraction of Al octahedral sites replaced by Fe is 0.179. This means that almost one out of five octahedral cations is Fe. Obviously this is a limiting case of maxima occupancy for Fe ions in octahedral coordination. However, it demonstrates that the substitution of Al by Fe constitutes the major defect in the mullite lattice. The orthorhombic crystal structure of mullite may also allow conductivity anisotropy.

* i,t refers to interstitial tetrahedral site; Al,o refers to octahedral site normally occupied by Al, etc.

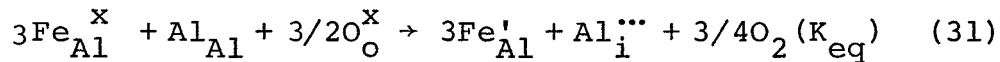
Using Maxwell's multiphase conduction model, the electrical conductivity for the iron-mullite composition (m_1) was about $2 \times 10^{-2} \text{ ohm}^{-1} \cdot \text{cm}^{-1}$ at 1200°C (Figure 40). The average activation energy for conduction was 1.205eV. On the other hand, the activation energies for compositions within the area $s_1s_2m_2m_1$ are lower and vary from 0.393 to 0.623eV because of the difference in the final mullite composition. These mullite phases have a higher silica content and a lower (Fe+Al)/Si ratio than m_1 . With a similar Fe_2O_3 content (10.32 - 14.37w/o) a larger fraction of Al cations are replaced by Fe ions.

Unfortunately, the conduction mechanism in mullite cannot be determined without additional information on the temperature dependence of the mobility term and the P_{O_2} dependence of the conductivity.

A different conductivity-temperature dependence was displayed by the composition $23\text{Fe}_3\text{O}_4-70\text{Al}_2\text{O}_3-7\text{SiO}_2$ (point "d" in Figure 50, within the $s_1m_1c_1$ compatibility triangle). This composition follows a crystallization path that leads to a product with a corundum(ss) phase as the matrix. The conductivity in air up to 1460°C has an activation energy of 2.97eV. This is comparable to values for Al_2O_3 of 2.97eV^{31} (undoped), 2.90eV^{32} (Co, Mg, Ti, Si-doped and undoped) and 2.47eV^{33} (undoped) from previous works. The impurity levels in the undoped crystals used by the other workers were less than 10 ppm. In a sample of compositions $23\text{Fe}_3\text{O}_4-70\text{Al}_2\text{O}_3-7\text{SiO}_2$

annealed at 1250°C in air, 13 m/o of iron was dissolved in the corundum phase. Comparing the results for the doped and undoped crystals, there is a similarity in the activation energies yet an enormous difference in the magnitude of the electrical conductivity. All these measurements probably are extrinsic even for the nominally "pure" crystals.

Of the Schottky and Frenkel type of intrinsic defects in alumina, it has now been suggested^{33,34,35,106} that Frenkel defects on the cation sublattice are the predominant type. Fe ions are incorporated substitutionally and the following defect reaction can be written,



Assuming charge neutrality

$$[\text{Al}_{\text{i}}^{\text{'''}}] = 1/3 [\text{Fe}_{\text{Al}}^{\text{'}}]$$

Dutt and Kroger³⁵ have suggested that $K_{\text{eq}} = 8.621 \times 10^3 \exp(-\frac{7.32\text{eV}}{RT})$. However, this enthalpy value of 7.32eV seems unrealistically large. Also, the $[\text{Fe}_{\text{Al}}^{\text{'}}]$ would then be a very strong function of temperature. Pollak³⁴ used a simple model and calculated the $\text{Fe}^{2+}/\text{Fe}^{3+}$ equilibrium ratio in iron-doped alumina. At 1600°C and $P_{\text{O}_2} = 10^{-2}$ atm, the $[\text{Fe}_{\text{Al}}^{\text{'}}]/[\text{Fe}_{\text{Al}}^{\text{x}}]$ ratio is 3×10^{-3} . Previous work¹⁰⁶ on the color centers in alumina has also indicated that the Fe ion is primarily present in the trivalent state.

In the high P_{O_2} region (above 5×10^{-3} atm), Pollak reported that the 4.4 m/o $\text{Fe-Al}_2\text{O}_3$ sample behaved like an

n-type conductor: $\sigma \propto P_{O_2}^{-0.18}$. Assuming Fe'_{Al} ionizes to give an electron in the conduction band,



he suggested that this ionizing reaction might be responsible for the electronic conduction. Assuming this defect model, the conductivity is,

$$\sigma \propto [Fe'_{Al}] = 3^{1/4} K_{eq}^{3/4} [Fe_{total}]^{3/4} P_{O_2}^{-3/16} \quad (33)$$

The predicted conductivity dependence of $P_{O_2}^{-3/16}$ is very close to Pollak's observed dependence of $P_{O_2}^{-0.18}$.

This model also predicts that at constant temperature and P_{O_2} , the electrical conductivity is dependent on $[Fe_{total}]^{3/4}$. Figure 51 is a plot of electrical conductivity at 1250°C in air as a function of $[Fe_{total}]$. The slope is 0.535, lower than as predicted by the model. Point A is obtained from this study.

In the preceding paragraphs, the emphasis has been focused on the correlation between the electrical conductivity results and the phase chemistry of the $FeO \cdot Fe_2O_3 - Al_2O_3 - SiO_2$ system. The conduction mechanism in the solid state was also discussed. Now, in the following, the conduction mechanism in iron aluminosilicate melt is considered in terms of the band conduction and thermally activated hopping models.

Systems such as $FeO - SiO_2$, $FeO - MnO - SiO_2$ and $FeO - CaO - SiO_2$ show appreciable non-ionic conductivity.⁷¹⁻⁷³ Electronic conductivity comprises 50% of the total conductivity at 20 w/o

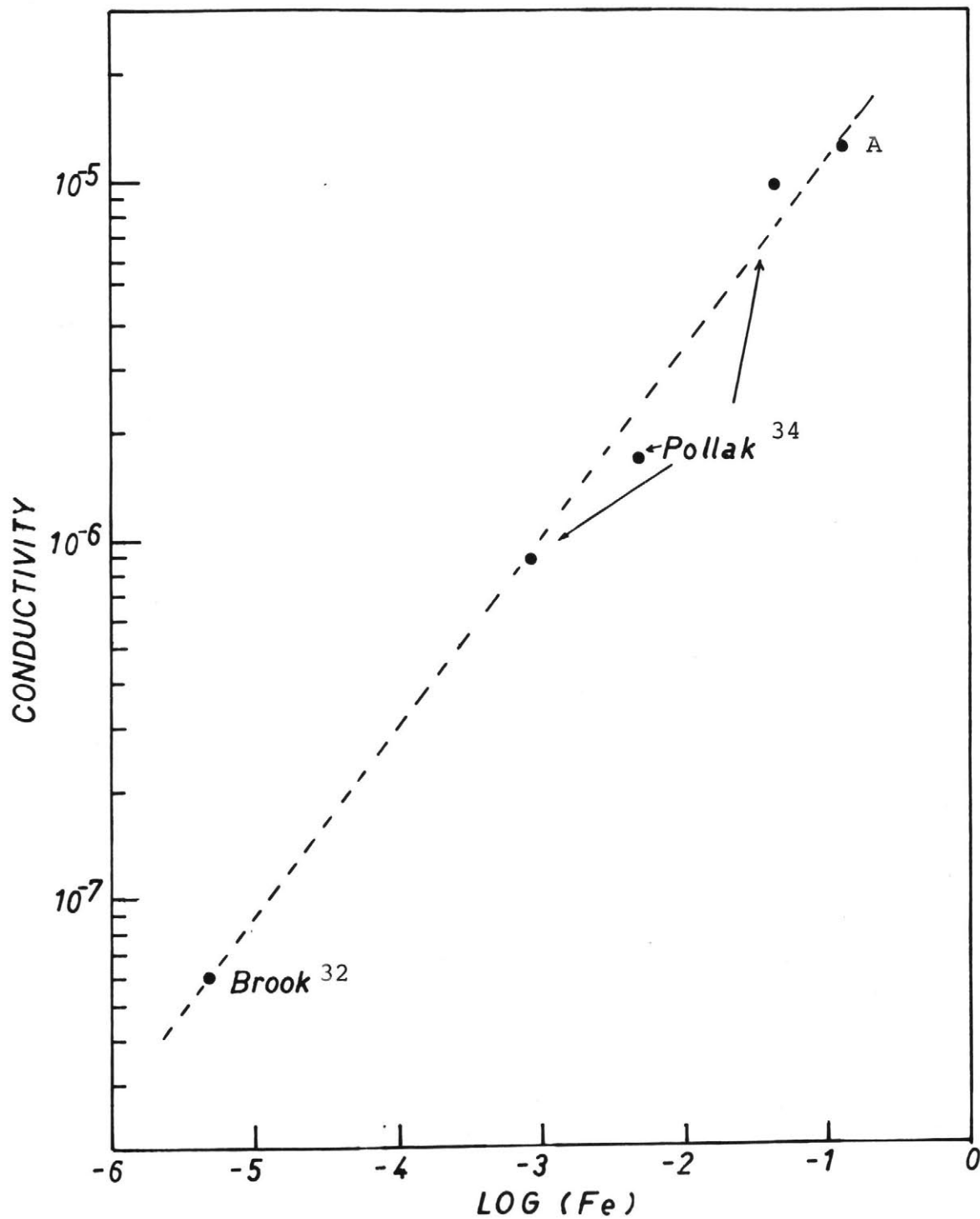


Figure 51. Electrical conductivity of Al_2O_3 as a function of iron content at 1250°C in air.

SiO_2 in FeO-SiO_2 and FeO-MnO-SiO_2 at 1400°C . For FeO-CaO-SiO_2 , this happens at a range of iron content (60-80%) depending on the $\text{CaO}/(\text{CaO}+\text{SiO}_2)$ ratio.⁽⁷³⁾ In liquid wustite, the ionic conductivity at 1400°C constitutes only 7-8% of the total conductivity.⁽⁷¹⁾ In measuring the dc-conductivity of iron aluminosilicate melt in this study, no time-dependent polarization was observed, indicating that the electrical conduction is primarily electronic. This is supported by the fact that the ac-conductivity of the melt up to 10 KHz is equivalent to the dc-conductivity.

Since the conductivity of the binary $\text{Al}_2\text{O}_3\text{-SiO}_2$ system is ionic and is only $6 \times 10^{-4} \text{ohm}^{-1}\cdot\text{cm}^{-1}$ at 1750°C , the value of $0.12 - 0.3 \text{ohm}^{-1}\cdot\text{cm}^{-1}$ for iron aluminosilicate melt suggests that the electronic behavior is due to the presence of iron ions.

Engell and Vygen⁷⁷ have considered two limiting models for electronic conduction in $\text{FeO-Fe}_2\text{O}_3\text{-CaO-SiO}_2$ melts. The conductivity was measured at 50 KHz and therefore had ionic and electronic contributions. The polaron hopping model and a collision dependent bimolecular reaction model were used to interpret the electronic conductivity results. However, their model was based on the time dependent collision of Fe^{2+} and Fe^{3+} ions to form an activated dipole prior to charge transfer. It also required ionic rearrangement after charge transfer was completed. Consequently, the odd feature of their approach lies in the fact that the electronic conduction is

actually dependent on the mobility of the Fe^{2+} ion.

The electrical conductivity data for the liquids in this study have been analyzed to distinguish between the band and polaron hopping model in an effort to identify the conduction mechanism in iron aluminosilicate melt. The most conclusive test in distinguishing between the two models is the temperature dependence of the charge carrier mobility. This temperature dependence is obtained only if the free charge carrier concentration is known at all temperatures.

Calculation of the iron ion concentration, N , in iron aluminosilicate requires a knowledge of the density of the melt. Henderson et al¹⁰⁷ reported that the positive deviation of the computed "ideal density", for mechanical mixtures of the pure components, FeO and SiO_2 , from the actual density of FeO-SiO_2 melt was less than 2.5% below 10 w/o SiO_2 . It is assumed that the density of iron aluminosilicate melt can be estimated by the value computed from the densities of the pure components. The densities of pure liquid iron oxide¹⁰⁸, alumina¹⁰⁹ and silica¹¹⁰ used are 4.0, 2.97 and 2.22 gm/cm^3 , respectively. The calculated values of N range from 8.475 x $10^{21}/\text{cm}^3$ (for a $36\text{Fe}_3\text{O}_4-37\text{Al}_2\text{O}_3-27\text{SiO}_2$ melt) to $1.924 \times 10^{22}/\text{cm}^3$ (for $71\text{Fe}_3\text{O}_4-19\text{Al}_2\text{O}_3-10\text{SiO}_2$).

To obtain the free carrier mobility using the band model, several assumptions are made. The conductivity increases with decreasing oxygen partial pressure in the P_{O_2} region above 10^{-1} atm, suggesting that the conduction may be n-typed. It

is also assumed that all ferrous ions can be ionized to give electrons in the conduction band. The free carrier concentration, n , at a given melt composition is then approximated by

$$n = (1-c) N \quad (34)$$

where $(1-c)$ is the fraction of iron ions in the divalent state. The carrier mobility is therefore,

$$\mu = \frac{\sigma}{e(1-c) N} \quad (35)$$

For the composition $73\text{Fe}_3\text{O}_4-20\text{Al}_2\text{O}_3-7\text{SiO}_2$, the term N in Equations 34 and 35 is replaced by $N_0 \exp(-0.216\text{eV}/RT)$ where the activation energy, 0.216eV , is obtained from the slope a plot of $\log(\sigma T^{3/2})$ versus reciprocal temperature and is taken to be the ionization energy for free charge carrier.

The mobility term, μ , is calculated for series of melts formed along the crystallization pathes of five compositions. $\log \mu$ is plotted against $\log T$ in Figure 52. A line with a slope of $-3/2$ is also drawn in the figure.

The decrease in mobility with increasing temperature supports the argument in favor of the conduction band model as the mechanism responsible for conduction in iron aluminosilicate melt. However, the calculated mobilities are of the order of $10^{-4} \text{cm}^2/\text{v}\cdot\text{sec}$, simply too small for the band model to be valid. Since the accuracy of the mobility term depends on the ability to predict the free carrier concentration, any erroneous assumption made in estimating the concentration would easily result in the underestimation of the mobility.

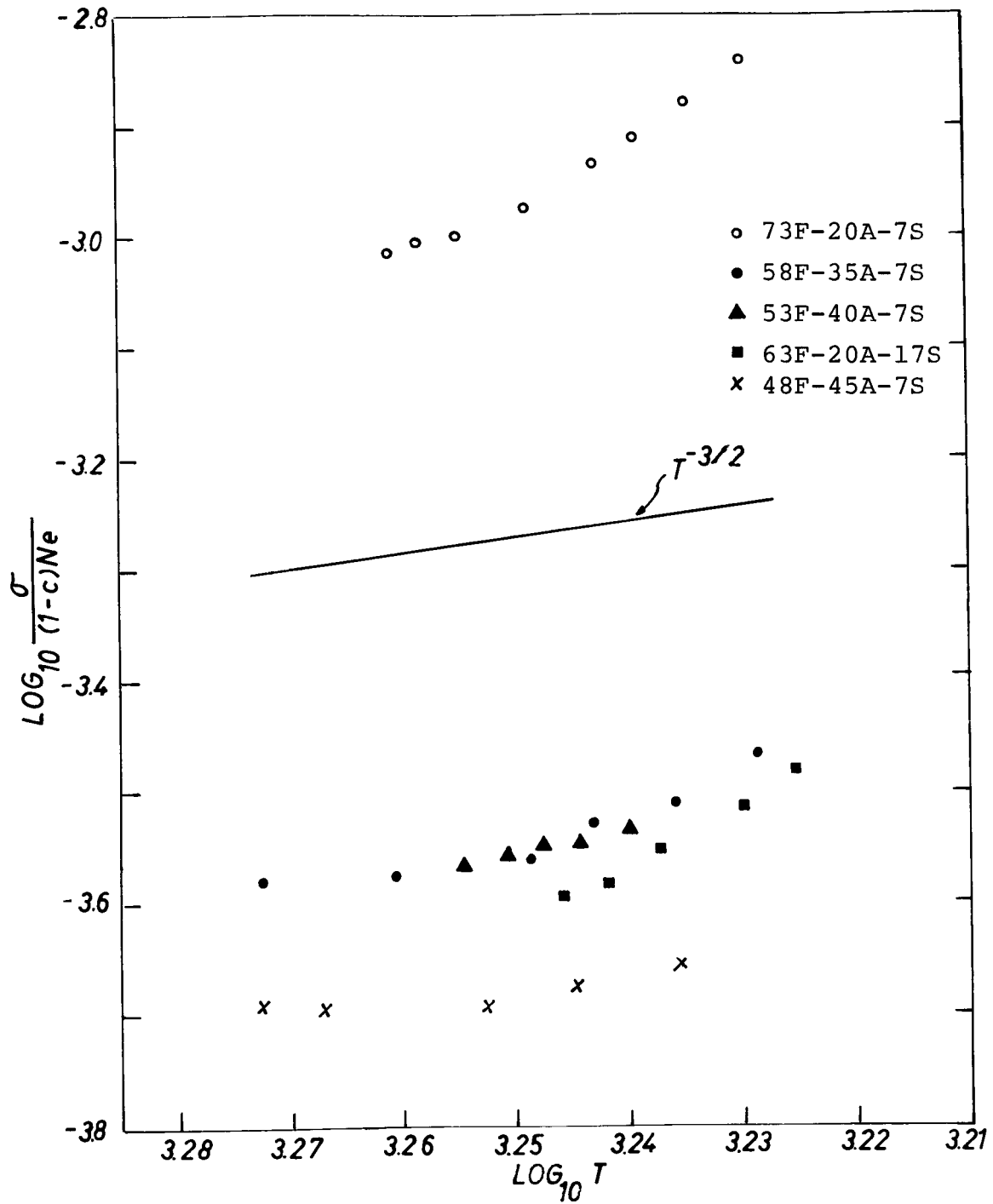


Figure 52. Free carrier mobility as a function of temperature, based on the conduction band model.

A critical assumption is that all ferrous ions are ionized. Despite the large variation in the melt composition: 36-73 w/o Fe_3O_4 , 17-37 w/o Al_2O_3 , 7-30 w/o SiO_2 , the electrical conductivity of the melt does not change significantly. The conductivity in air at 1550°C for a melt of composition 71 Fe_3O_4 -19 Al_2O_3 -10 SiO_2 ($N = 1.92 \times 10^{22}/\text{cm}^3$) is $2.37 \times 10^{-1} \text{ohm}^{-1} \cdot \text{cm}^{-1}$ and that for composition 36 Fe_3O_4 -37 Al_2O_3 -27 SiO_2 ($N = 8.475 \times 10^{21}/\text{cm}^3$) is $1.138 \times 10^{-1} \text{ohm}^{-1} \cdot \text{cm}^{-1}$. One would expect that if all ferrous ions contribute to the free carrier concentration, any variation in the melt composition and change in $(1-c)N$ will affect the conductivity correspondingly. Figure 53 is a plot of electrical conductivity at 1550°C in air plotted as a function of $(1-c)N$ in the melt. The proportionality between the conductivity and $(1-c)N$ lends additional support to the validity of the above assumption.

The low value of the mobility term ($10^{-4} \text{cm}^2/\text{v} \cdot \text{sec}$) suggests that the charge carriers are localized and thus the conductivity should be analyzed for dependencies as in the polaron hopping model.

Using Equation 7, a plot of $\log \sigma T/N c(1-c)a^2$ versus reciprocal temperature should give the activation energy of the mobility, with ν and R_{Fe} (the $\text{Fe}_{\text{oct}}^{3+}/\text{Fe}_{\text{total}}$ ratio) assumed to be constant. This plot (Figure 54) shows no activation energy for four of the five cases. Even though this seems to suggest that polaron hopping is not the conduction mechanism in the melt, the evidence is by no means conclusive.

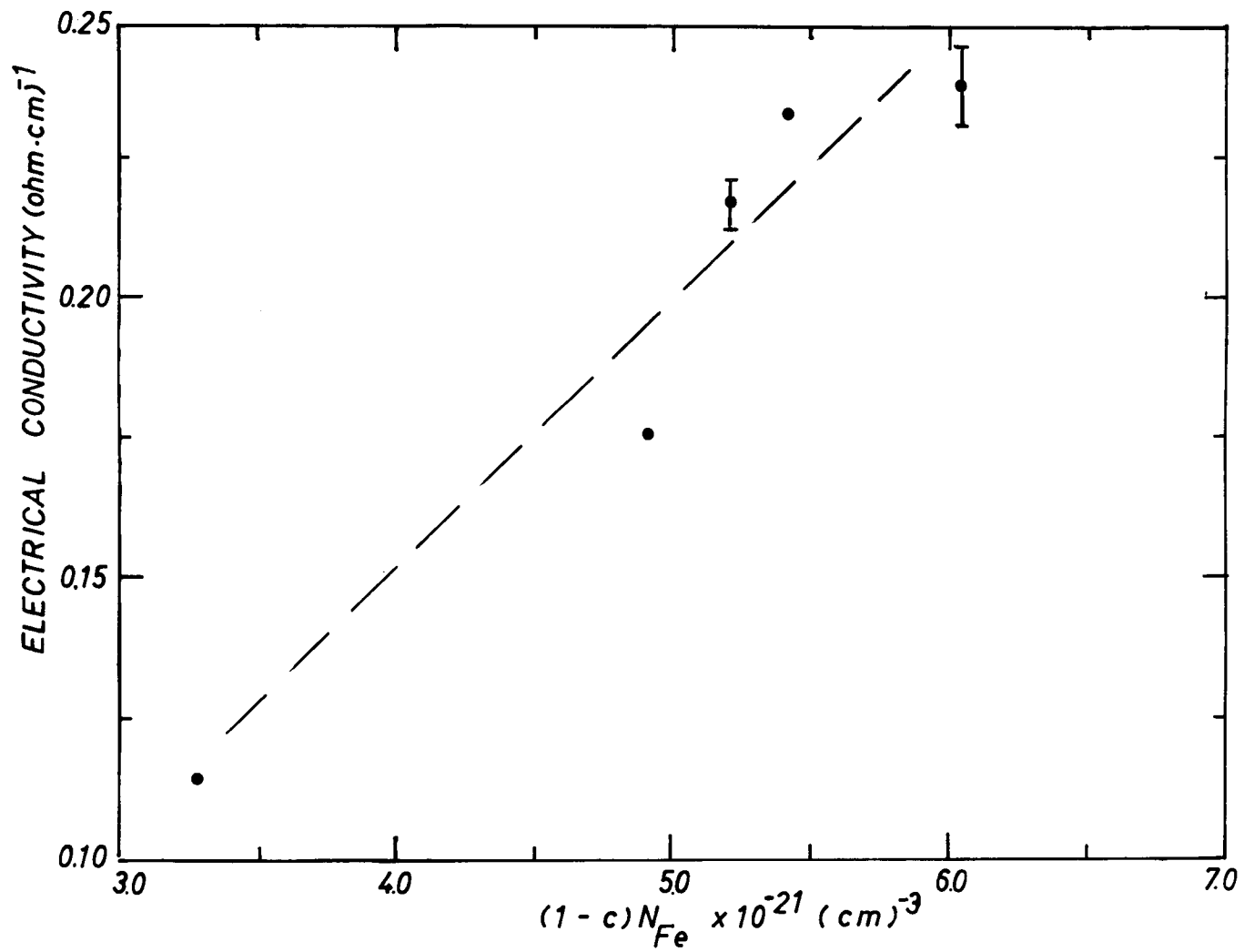


Figure 53. Electrical conductivity in iron aluminosilicate melt as a function of ferrous ion concentration

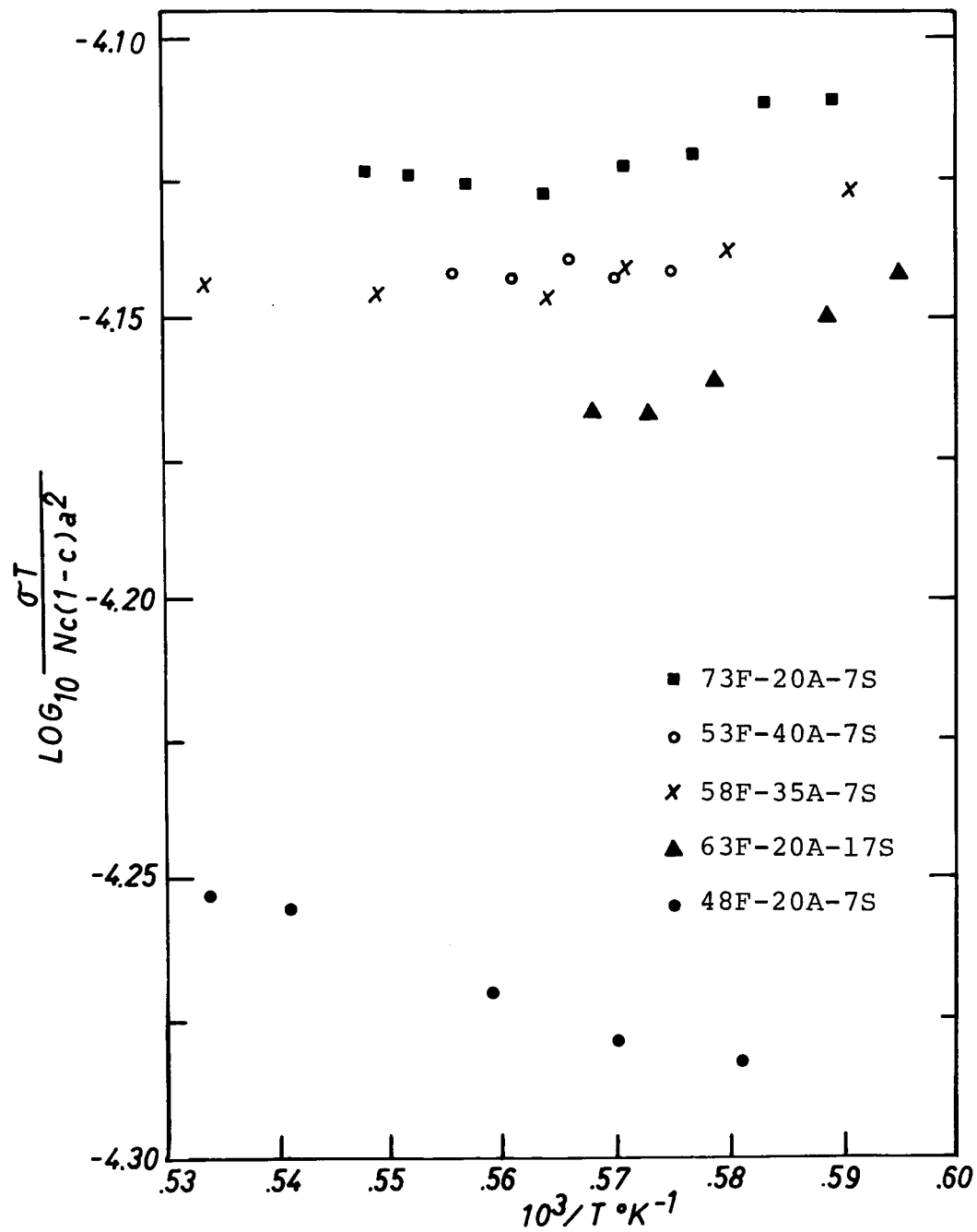


Figure 54. Effective mobility as a function of temperature, based on the polaron hopping model (R_{Fe} assumed to be constant).

This apparent disagreement with hopping conduction is based on the premise that R_{Fe} remains constant even for different melt compositions. For the overall composition $73Fe_3O_4-20Al_2O_3-7SiO_2$, the liquid composition is about $71Fe_3O_4-19Al_2O_3-10SiO_2$ at $1550^\circ C$ and as the temperature is lowered to $1477^\circ C$, the approximate liquid composition becomes $65Fe_3O_4-17Al_2O_3-18SiO_2$. The above analysis assumes R_{Fe} to be the same for the two melts.

The R_{Fe} term is actually a function of composition and the Fe^{3+}/Fe^{2+} ratio. The conductivity of iron aluminosilicates depends on the oxygen partial pressure in the following manner. At high P_{O_2} , the conductivity increases with decreasing P_{O_2} . In the intermediate range the conductivity is insensitive to any change in P_{O_2} , and finally at very low P_{O_2} , it decreases upon further reduction. Since the $c(1-c)$ term is sensitive to the oxygen partial pressure over the melt, the following expression holds for a single-phase melt under isothermal conditions:

$$\sigma \propto R_{Fe} \cdot c(1-c)$$

Results show that the conductivity maxima are located at $c > 0.5$ (Figure 49), suggesting that some of the Fe^{3+} ions are in tetrahedral coordination and are not involved in the conduction process as they are covalently bonded to the silicate anions. Figure 55 depicts the Fe^{3+} distribution factor R_{Fe} as a function of composition. The distribution is very similar to the results of Pargamin¹⁸ for $FeO-Fe_2O_3-Al_2O_3-SiO_2$ melts (Figure 1).

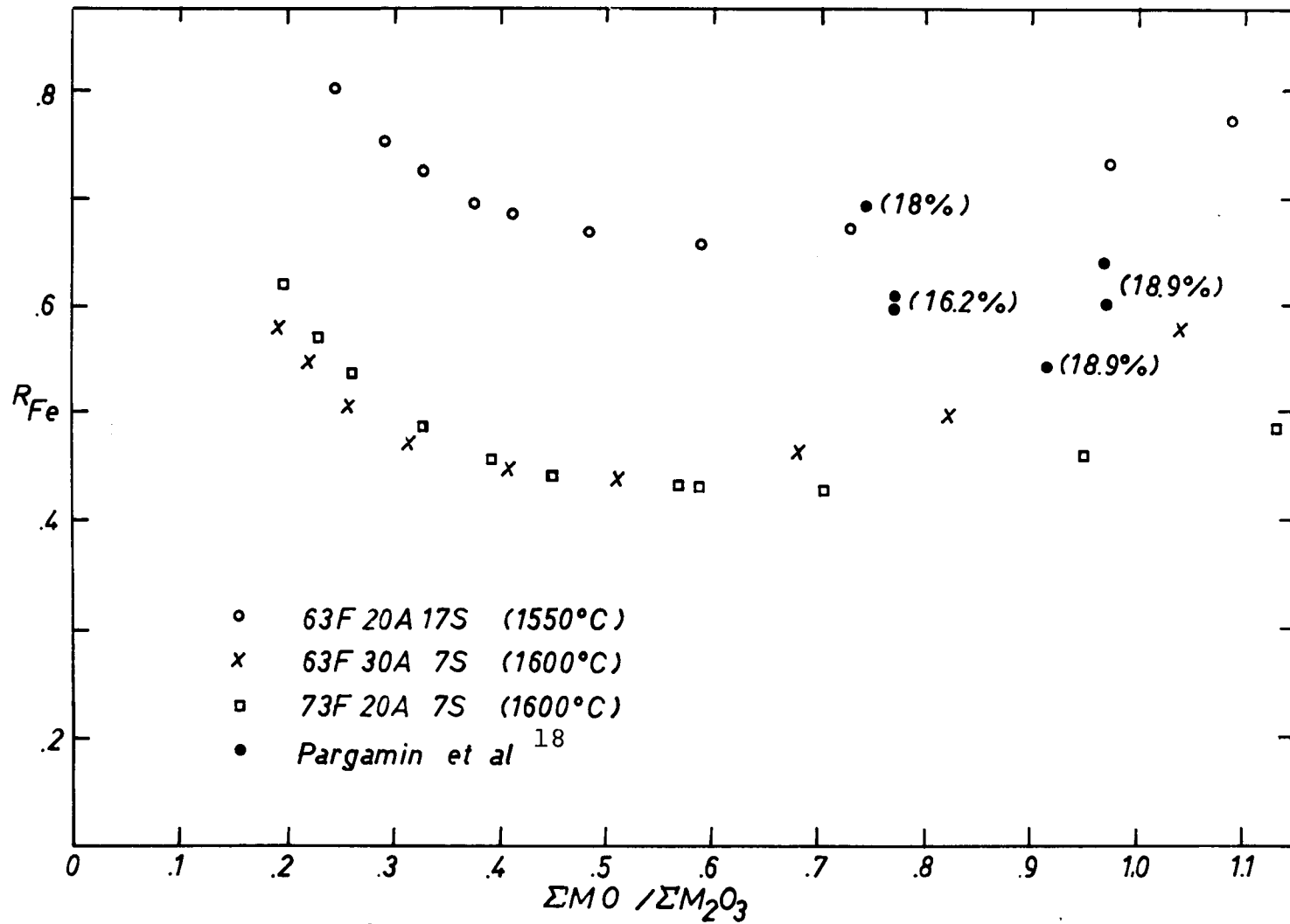


Figure 55. Fe^{3+} distribution factor, R_{Fe} , as a function of composition in iron aluminosilicate melts.

The Fe^{3+} ions allocate themselves in octahedral and tetrahedral sites such that at the particular value of c and melt composition, the free energy of the system is a minimum. In a FeO-SiO_2 melt of low SiO_2 content, Masson⁸⁶ suggested that the anions are mostly SiO_4^{4-} with a small concentration of $\text{Si}_2\text{O}_7^{6-}$. Addition of Al_2O_3 to the iron silicate increases the fraction of complex anions in the liquid. The Al ions in the liquid can occupy both tetrahedral and octahedral coordinations.^{111,112} It is therefore probable that some of the Al and Fe^{3+} ions are part of the network-forming unit in iron aluminosilicate melts. Complex anions such as SiO_4^{4-} , AlO_4^{5-} , $\text{Si}_2\text{O}_7^{6-}$, SiAlO_7^{7-} , SiFeO_7^{7-} , etc. would be present.

It is also interesting to note the effect of SiO_2 content on R_{Fe} (Figure 55). Higher SiO_2 content increases R_{Fe} . This suggests that if more network-forming Si ions become available, a greater portion of the Fe^{3+} ions are relieved from the polymeric anions and go into octahedral coordination. This may be related to the higher activities of Fe_2O_3 at higher SiO_2 content. Consequently it is very unlikely for R_{Fe} to be the same for the two melts: (a) $71\text{Fe}_3\text{O}_4-19\text{Al}_2\text{O}_3-10\text{SiO}_2$ ($\Sigma\text{MO}/\Sigma\text{M}_2\text{O}_3 = 0.638$), (b) $65\text{Fe}_3\text{O}_4-17\text{Al}_2\text{O}_3-18\text{SiO}_2$ ($\Sigma\text{MO}/\Sigma\text{M}_2\text{O}_3 = 0.676$), discussed above. The concave upward contour of the $\log_{10} \sigma T/N c(1-c)a^2$ versus reciprocal temperature plot (Figure 54) can be due to the variation in R_{Fe} . Taking R_{Fe} to be 0.45 and 0.65 for melts (a) and (b) respectively (obtained from Figure 55), $\log_{10} \sigma T/N c(1-c)a^2 R_{\text{Fe}}$ is $1.666 \times 10^{-4} \text{ohm}^{-1} \cdot \text{K}$ for melt (a) at

1552°C and is $1.159 \times 10^{-4} \text{ohm}^{-1} \cdot \text{K}$ for melt(b) at 1477°C. Hence, taking the R_{Fe} term into consideration, a lower mobility at lower temperature is likely.

It is then quite possible that the apparent disagreement between Figure 54 and the polaron hopping model is due to the variation in the R_{Fe} term with the liquid composition. For the specific instance that the R_{Fe} term is considered, the mobility shows indication of a thermally activated behavior.

In summation, the electrical conductivity data of the $\text{FeO} \cdot \text{Fe}_2\text{O}_3 - \text{Al}_2\text{O}_3 - \text{SiO}_2$ system have been directly correlated to its phase chemistry and crystallization sequence. The electrical conductivity of the solid composites can be interpreted with a multiphase conduction model. The conduction mechanisms in the composite matrices, iron aluminosilicate glasses, iron-mullite and $\text{Fe} - \text{Al}_2\text{O}_3$ have been discussed. As regards iron aluminosilicate melts, basing on the available evidence, one cannot determine unambiguously the conduction mechanism. Analysis of the results according to a band conduction model gives a decreasing mobility with increasing temperature. Yet the mobility ($10^{-4} \text{cm}^2/\text{v} \cdot \text{sec}$ between 1450° and 1550°C) is too low for the band model to be valid. Initial analysis of the data based on the polaron hopping model, with R_{Fe} assumed to be constant for all melt compositions, does not lead to a thermally activated mobility term. Further consideration with the variation in R_{Fe} taken into account

seem to suggest that the conduction process is thermally activated.

Confirmation of either model as the conduction mechanism will require exact information on the charge carrier concentration, the precise dependence of R_{Fe} on melt composition and the temperature dependence of the mobility term.

Chapter VIII. Conclusions

The dc- and ac-conductivity results of the compositions (7 or 17 w/o SiO_2) in the $\text{FeO}\cdot\text{Fe}_2\text{O}_3\text{-Al}_2\text{O}_3\text{-SiO}_2$ system, which are investigated, suggest that the conduction is predominantly electronic for compositions with more than 33 w/o Fe_3O_4 .

Four basic types of conductivity-temperature dependence are observed in air and are explained in terms of the phase chemistry of the system. Comparison of the conductivity-temperature dependence with the phase equilibria strongly indicates a direct correlation between the result and the crystallization sequence followed by each composition. The conductivity in the crystallized composites of spinel, mullite, cordierite or iron aluminosilicate glasses has to be interpreted in terms of multiphase conduction. The four types of conductivity-temperature dependence are summarized as follows:

1. The electrical conductivity increases with decreasing temperature with no distinct discontinuity upon solidification in the first kind of behavior. This is the case for all three compositions studied, which are in the compatibility region $\text{SiO}_2\text{-s}_2\text{-m}_2$ (Figure 23). These compositions crystallize to form an aggregate with iron aluminosilicate glasses as the matrix. Unfortunately, the conduction mechanism in the glass remains unidentified due to the inability in measuring its iron content.

2. The dependence of electrical conductivity on temperature is of three stages in the second type of behavior. A sharp discontinuity is observed at about 1390°C in the conductivity

of compositions in the area $s_1s_2m_2m_1$ (Figure 23). The conduction in the crystallized composites is through the iron-mullite matrices and shows activation energies varying from 0.292 to 0.623eV, depending on the iron content and the (Fe+Al)/Si ratio.

3. The discontinuity occurs at 1460°C for compositions within the compatibility triangle $s_1m_1c_1$ (Figure 23). The thermal activation energies for conduction in crystallized composites with an iron-mullite (13.09 w/o Fe_2O_3 , 61.37 w/o Al_2O_3 , 25.53 w/o SiO_2) matrix are 1.155, 1.212 and 1.248eV. The conductivity of this iron-mullite is calculated using Maxwell's multiphase conduction model. Due to its disordered crystal structure and varying composition, the conduction mechanism in iron-mullite is not determined unambiguously.

4. For the composition $23Fe_3O_4-70Al_2O_3-7SiO_2$, the drop in conductivity at 1460°C is over two orders of magnitude. The thermal activation energy is 2.97eV and is attributed to conduction in the crystallized composite through a corundum matrix containing 13 m/o Fe. It is tentatively suggested that the ionization of Fe_{Al}^{\cdot} is responsible for the electrical conduction.

The conductivity of iron aluminosilicate melts at 1550°C and 1600°C decreases with increasing oxygen partial pressure at $P_{O_2} > 10^{-1}$ atm. It remains essentially constant over the intermediate range of $10^{-5} < P_{O_2} < 10^{-1}$ atm. Upon subsequent reduction at still lower P_{O_2} , the electrical conductivity

decreases, indicating that it may be p-typed.

Based on the available evidence, the conduction mechanism in iron aluminosilicate melts cannot be determined unambiguously. Analysis of the results according to a band conduction model gives a decreasing mobility with increasing temperature. However, the mobility is 10^{-4} cm²/v·sec between 1450° and 1550°C and is too low for the band model. Using the polaron hopping model, the fraction of Fe³⁺ ions in octahedral coordination, R_{Fe} , is calculated. Analysis of the data with the variation in R_{Fe} taken into account suggests that the conduction process is thermally activated.

Chapter IX. Suggestions for Future Work

Several experiments are suggested which would be helpful in elucidating the areas that are not yet resolved by the present study.

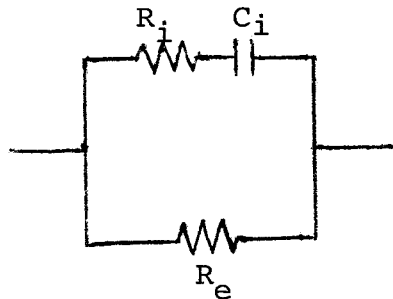
1. A direct measurement of the Hall coefficients of mullite and iron aluminosilicate glasses to determine the charge carrier mobility at different temperatures, this would help identify the conduction mechanisms.
2. A study of the electrical conductivity of a simple system such as iron silicate as a function of temperature, composition and oxygen partial pressure, this would provide valuable information on the conduction mechanism in more complex silicate melts containing iron oxide.
3. Very little is known about mullite, especially the substitution of Al by Fe ions. It should be exciting to carry out equilibrium thermogravimetric and conductivity measurements on mullites with different Al/Si and (Fe+Al)/Si ratios as a function of oxygen partial pressure. This will provide important understanding on the defects in mullite.
4. To study the effect of addition of Al_2O_3 on the density of iron silicate melt. This can give further information on the structural constitution of the melt.

Appendix: Equivalent Circuit for Ionic and Electronic Conductivity.

An interesting problem has been the capability to discern the electronic and ionic contribution to the total conductivity of a material. The ionic transference number can be obtained by electrochemical cell measurements, while the dc conductivity at "infinite" time gives the electronic conductivity. Any ionic component would be observed as a time-dependent polarization process in a dc measurement, if blocking electrodes are used.

A simple equivalent circuit can be used to model as the electronic and ionic conductivity.

The electronic path is represented by the resistor R_e , whereas the ionic path is indicated by the capacitor C_i in series with resistor R_i .



The impedance of this network is

$$Z_i = \frac{1}{\frac{1}{R_e} + \frac{1}{R_i - j\omega C_i}}$$

$$= \frac{(R_e R_i (R_e + R_i) \omega^2 C_i^2 + R_e) - j \omega C_i R_e^2}{(R_e + R_i)^2 \omega^2 C_i^2 + 1}$$

The measured impedance $|Z_i|$ is

$$|Z_i| = \sqrt{\frac{R_e^2 R_i^2 (R_e + R_i)^2 \omega^4 C_i^4 + 2 R_e^2 R_i (R_e + R_i) \omega^2 C_i^2 + R_e^2 + \omega^2 C_i^2 R_e^2}{(R_e + R_i)^2 \omega^2 C_i^2 + 1}}$$

$$= \sqrt{\left(\frac{R_e R_i (R_e + R_i) \omega^2 C_i^2 + R_e}{(R_e + R_i)^2 \omega^2 C_i^2}\right)^2 + \left(\frac{\omega C_i R_e^2}{(R_e + R_i)^2 \omega^2 C_i^2}\right)^2}$$

at sufficiently high frequency, $\omega \gg \omega_c$ with $\omega_c \approx \frac{1}{R_i C_i}$

$$|Z_i| = \frac{R_e R_i}{R_e + R_i}$$

and considering $\sigma_e \propto \frac{1}{R_e}$ and $\sigma_i \propto \frac{1}{R_i}$ then at $\omega \gg \omega_c$

$$\sigma(\omega) = \sigma_i + \sigma_e$$

Consequently, at $\omega = 0$, the dc conductivity represents the electronic contribution. The conductivity increases with frequency, in the range $0 < \omega < \omega_c$, due to the increasing contribution of the ionic component. At a frequency, $\omega \gg \omega_c$, the total conductivity is independent of frequency as the presence of C_i is insignificant. It is the summation of contributions from ionic and electronic parts. This frequency-independent conductivity together with the dc-value give the ionic and electronic transference numbers.

At much higher frequencies such as 10^7 Hz and above, electron polarization and other ionic processes become important. The conductivity is no longer a simple function of frequency.

References

1. The M.I.T.-OCR (ERDA) Patent disclosures include several fabrication methods including flame spraying, hot-pressing, the oxidation of a graded Fe-Al alloy, etc.
2. D. Adler, "Insulating and Metallic States in Transition Metal Oxides" in Solid State Physics, V.21, 1-113 Academic Press, New York, (1968).
3. T. Holstein, "Studies of Polaron Motion", Ann. Phys., 8, 343-389 (1959).
4. R. R. Heikes and W. D. Johnston, "Mechanism of Conduction in Lithium-Substituted Transitional Metal Oxides", J. Chem. Phys. 26, 583-587 (1957).
5. I. G. Austin and N. F. Mott, "Polarons in Crystalline and Non-crystalline Materials", Adv. Phys., 18 (71), 41-102, (1969).
6. I. G. Austin, "Polaron Conduction in Disordered 3d Oxides", J. Non-crystalline Solids, 2, 474-483 (1970).
7. N. F. Mott and E. A. Davis, Electronic Processes in Non-Crystalline Materials. Clarendon Press, Oxford, (1971).
8. D. Adler, "Amorphous Semiconductors", C.R.C. Press, Cleveland, Ohio 44128.
9. N. F. Mott, "Introductory Talk; Conduction in Non-crystalline Materials", J. Non-Crystalline Solids, 8-10, 1, (1972).
10. N. F. Mott, "Electrons in Disordered Structures", Advan. Phys., 16 (61) 49-144, (1967).
11. N. F. Mott, "Conduction in Glasses Containing Transition Metal Ions", J. Non-Crystalline Solids, 1, 1-17 (1968).
12. M. Sayer and A. Mansingh, "Transport Properties of Semiconducting Phosphate Glasses", Phys. Rev., 6B (12), 4629-4642 (1972).
13. J. A. Boon and W. S. Fyfe, "The Coordination Number of Ferrous Ions in Silicate Glasses", Chem. Geol., 10(10), 287-298 (1972).
14. C. R. Kurkjian and E. A. Sigety, "Coordination of Fe³⁺ in Glass", Phys. Chem. Glasses, 9 (3), 73-83 (1968).

15. R. J. Edwards, A. Paul and R. W. Douglas, "Spectroscopy and Oxidation-Reduction of Iron in $MO \cdot P_2O_5$ Glasses", *Phys. Chem. Glasses*, 13 (5) 137-143 (1972).
16. M. F. Taragin, J. C. Eisenstein and W. Haller, "Mossbauer Study of Fe^{57} in an Aluminophosphate Glass", *Phys. Chem. Glasses.*, 13 (5) 149-152 (1972).
17. D. Loveridge and S. Parke, "Electron Spin Resonance of Fe^{3+} , Mn^{2+} , and Cr^{3+} in Glasses", *Phys. Chem. Glasses*, 12 (1), 19-27, (1971).
18. L. Pargamin, C. H. P. Lupis and P. A. Flinn, "Mossbauer Analysis of the Distribution of Iron Cations in Silicate Slags", *Met. Trans.*, 3 (8), 2093-2105 (1972).
19. R. E. Meredith and C. W. Tobias, "Conduction in Heterogeneous Systems", *Adv. Electrochem. Electrochemic. Engng.*, 2, 15 (1962).
20. V. G. Ondracek and B. Schulz, "Zur Leitfähigkeit von Cermets und Anderen Mehrphasigen Werkstoffen", *Deu. Keram. Gesell.*, 48 (10), 427-434 (1971).
21. R. C. Progelhof, J. L. Throne and R. R. Ruetsch, "Methods for Predicting the Thermal Conductivity of Composite Systems: A Review", *Polym. Eng. Sc.* 16 (9), 615-625 (1976).
22. J. C. Maxwell, A Treatise on Electrical and Magnetism, 2nd Ed., Vol. I, p. 435. Clarendon Press, Oxford, (1881).
23. R. B. Grekila and T. Y. Tien, "Conductivity Discontinuity in a Two-Phase System", *J. Am. Ceram. Soc.*, 48 (1), 22-25 (1965).
24. D. A. G. Bruggeman, "Dielectric Constant and Conductivity of Mixtures of Isotropic Substances", *Ann. Physik*, 24, 636-664 (1935).
25. A. Muan, "Phase Equilibria at Liquidus Temperatures in the System Iron Oxide- Al_2O_3 - SiO_2 in Air Atmosphere", *J. Am. Ceram. Soc.*, 40 (4), 121-133 (1957).
26. A. Muan, "Phase Equilibrium Relationships at Liquidus Temperatures in the System FeO - Fe_2O_3 - Al_2O_3 - SiO_2 ", *J. Am. Ceram. Soc.*, 40 (12), 420-431 (1957).
27. A. Navrotsky and O. J. Kleppa, "The Thermodynamics of Cation Distributions in Simple Spinel", *J. of Inorg. Nucl. Chem.*, 29 (11), 2701-2714 (1967).

28. P. A. Miles, W. B. Westphal and A. von Hippel, "Dielectric Spectroscopy of Ferromagnetic Semiconductors", *Rev. Mod. Phys.*, 29, 279-307 (1957).
29. D. S. Tannhauser, "Conductivity in Iron Oxides", *Phys. Chem. Solids*, 23, 25-34 (1962).
30. T. O. Mason, private communication.
31. J. Pappis and W. D. Kingery, "Electrical Properties of Single-Crystal and Polycrystalline Alumina at High Temperatures", *J. Am. Ceram. Soc.*, 44, 459-464 (1961).
32. R. J. Brook, J. Yee and F. A. Kroger, "Electrochemical Cells and Electrical Conduction of Pure and Doped Al₂O₃", *J. Am. Ceram. Soc.*, 54 (9), 444-451 (1971).
33. K. Kitazawa and R. L. Coble, "Electrical Conduction in Single-Crystal and Polycrystalline Al₂O₃ at High Temperature", *J. Am. Ceram. Soc.*, 57 (6), 245-250 (1974).
34. T. M. Pollak, "High Temperature Electrical Conductivity and Defect Chemistry of Iron-Doped Alumina", S.M. Thesis, Dept. of Materials Science and Eng., M.I.T., 1976.
35. B. V. Dutt and F. A. Kroger, "High Temperature Defect Structure of Iron-Doped α -Alumina", *J. Am. Ceram. Soc.* 58 (11-12), 474-476 (1975).
36. W.A. Deer, R.A. Howie and J. Zussman, An Introduction to the Rock Forming Materials, Halsted Press.
37. R. Sadanaga, M. Tokonami and Y. Takeuchi, "The Structure of Mullite, 2Al₂O₃·SiO₂, and Relationship with the Structures of Sillimanite and Andalusite", *Acta. Cryst.* 15 (5), 65-68 (1962).
38. D. N. Sitharamarao, J. F. Duncan and M. F. Coleman, "Recrystallization of Kaolinite and Iron-Doped Kaolinite Glasses", *Rev. Chim. Minerale*, 9, 549-556 (1972).
39. J. F. Duncan, K. J. D. McKenzie and D. J. Stewart, "Migration of Cations in Two Solid-State Reactions", *Symp. Farad. Soc.* 1, 103-118 (1967).
40. H. G. Sockel, "Defect Structure and Electrical Conductivity of Crystalline Ferrous Silicate" in Defects and Transport in Oxides, ed. by M. S. Seltzer and R. I. Jaffee, Plenum Press, New York, (1973).

41. E. J. W. Verwey, P. W. Haaijuan, F. C. Romeijn and G. W. Van Oosterhont, "Controlled Valency Semiconductor", Philips Res. Rep. 5, 173-187 (1950).
42. J. D. MacKenzie, Modern Aspects of Vitreous State, 3, Butterworths, (1964).
43. J. D. MacKenzie, "Semiconducting Oxide Glasses: General Principle for Preparation", J. of Am. Ceram. Soc. 47 (5), 211-214 (1964).
44. P. L. Baynton, H. Rawson and J. E. Stanworth, "Semi-Conducting Properties of Some Vanadate Glasses", J. Electrochem. Soc., 104 (4), 237-240 (1957).
45. H. J. L. Trap and J. M. Stevels, "Ionic and Electronic Conductivity of Some New Types of Glass-Like Materials", Phys. Chem. Glasses. 4 (5), 193-205 (1963).
46. P. S. Roger and J. Williamson, "The Nucleation of Crystalline Phases in Silicate Glasses Containing Iron Oxide", Glass Tech. 10 (5), 128-133 (1969).
47. J. Williamson, A. J. Tipple and P. S. Rogers, "Influence of Iron Oxides on Kinetics of Crystal Growth in CaO-MgO-Al₂O₃-SiO₂ Glasses", JISI, 206 (9), 898-903 (1968).
48. J. Williamson, "Kinetics of Crystal Growth in an Aluminosilicate Glass Containing Small Amounts of Transition-Metal Ions", Mineral Mag. 37(291), 759-770 (1970).
49. M. O'Horo and R. Steinitz, "Characterization of Devitrification of an Iron-Containing Glass by Electrical and Magnetic Properties", Mat. Res. Bull., 3, 117-126 (1968).
50. Bh.V. Janakirama-Rao, "Structure and Mechanism of Conduction of Semiconductor Glasses", J. Am. Ceram. Soc. 48 (6), 311-319 (1965).
51. Bh.V. Janakirama-Rao, "Infrared Spectra of GeO₂-P₄O₁₀-V₂O₅ Glasses and Their Relation to Structure and Electronic Conduction", J. Am. Ceram. Soc. 49 (11), 605-609 (1966).
52. T. N. Kennedy and J. D. MacKenzie, "Role of the Network Former in Semi-Conductivity Oxide Glasses", Phys. Chem. Glasses, 8 (5), 169-173 (1967).

53. K. W. Hansen, "Semiconduction in Iron Phosphate Glasses", J. Electrochem. Soc., 112 (10), 994-996 (1965).
54. J. G. Vaughan and D. L. Kinser, "Electrical Resistivity Surface for FeO-Fe₂O₃-P₂O₅ Glasses", J. Am. Ceram. Soc. 58 (7-8), 326-329 (1975).
55. K. W. Hansen and M. T. Splann, "Dielectric Properties of Semiconducting Iron Phosphate Glasses", J. of Electrochem. Soc., 113 (9), 895-899 (1966).
56. R. A. Miller and K. W. Hansen, "Mechanical Loss and Conduction Mechanism in Iron-Phosphate Glass", Ibid. 116 (2), 254-257 (1969).
57. D. L. Kinser, "Structure and Electrical Properties of FeO-P₂O₅ Glasses", J. of Electrochem. Soc. 117 (4), 546-548 (1970).
58. A. W. Dozier, L. K. Wilson, E. J. Friebele and D. L. Kinser, "Correlation of Structure and Electrical Properties of 55FeO-45P₂O₅ Glass", J. of Am. Ceram. Soc. 55 (7), 373-377 (1972).
59. A. P. Schmid, "Evidence for the Small Polaron as the Charge Carrier in Glasses Containing Transition Metal Oxides", J. Appl. Phys. 39 (7), 3140-3149 (1968).
60. T. Allersma, R. Hakim, T. N. Kennedy and J. D. MacKenzie, "Structure and Physical Properties of Solid and Liquid Pentoxide", J. Chem. Phys. 46 (1), 154-160 (1967).
61. G. S. Linsley, A. E. Owen and F. M. Hayatee, "Electronic Conduction in Vanadium Phosphate Glasses", J. of Non-Crystalline Solids, 4, 208-219 (1970).
62. M. Munakata, "Electrical Conductivity of High Vanadium Phosphate Glass", Solid State Electronic, 1, 159-163 (1960).
63. J. O'M. Bockris, J. A. Kitchener, S. Ignatowicz and J. W. Tomlinson, "The Electrical Conductivity of Silicate Melts: Systems Containing Ca, Mn, and Al", Disc. Faraday Soc., 4, 265-281 (1948).
64. J. O'M. Bockris, J. A. Kitchener, S. Ignatowicz and J. W. Tomlinson, "Electric Conductance in Liquid Silicates", Trans. Faraday Soc., 48, 75-91 (1952).

65. J. Taylor, "Diffusion in Liquid Slags", Physical Chemistry of Process Metallurgy; the Richardson Conference, Inst. Mining Met. London, p. 31-34 (1974).
66. S. I. Popel, A. A. Deryabin, L. N. Saburov and M. Tarkhanov, "Surface Properties of High Aluminate Slags", Tr. Ural. Nauch-Issled Inst. Chern. Met., 12, 92-97 (1971).
67. A. E. Martin and G. Derge, "The Electrical Conductivity of Molten Blast-Furnaces Slags", Trans A.I.M.E. 154, 104-115 (1943).
68. J. W. Tomlinson and H. Inouye, "The Electric Conductance of Liquid Iron Oxide", J. of Chem. Phys. 20, 193, (1952).
69. H. Inouye, J. Tomlinson and J. Chipman, "The Electrical Conductivity of Wustite Melts", Trans. Faraday Soc. 49 (7), 796-801 (1953).
70. W. A. Fischer and H. Vom Ende, "Das Elektrische Leitvermogen von Schlackan im Flussigen und Feston Zustand", Arch. Eisenhüttenw, 21, 217-224 (1950).
71. M. T. Simnad, G. Derge and I. George, "Ionic Nature of Liquid Iron-Silicate Slags", Trans. A.I.M.E., 200 (12), 1386-1390 (1954).
72. D. A. Dukelow and G. Derge, "Electrochemical Characteristics of FeO-MnO-SiO₂ Melts", Trans A.I.M.E., 218 (2), 136-141 (1960).
73. W. R. Dickson and E. B. Dismukes, "The Electrolysis of FeO-CaO-SiO₂ Melts", Trans A.I.M.E., 224 (6), 505-511 (1962).
74. A. Wejnarth, "The Current Conducting Properties of Slags in Electric Furnaces", Trans. Electrochem. Soc. 65, 177-187 (1934).
75. E. A. Pastukhov, O. A. Esin and S. K. Chuchmarev, "The Electrical Conductivity of Molten Silicates Containing Iron Oxides", Elektrokimiya, 2 (2), 209-215 (1966).
76. Yu. M. Sizov, O. A. Esin and A. I. Sotuikov, "Nature of Conduction and Polarization in Non-Ferrous Slags", Elektrokimiya, 4 (4), 447-450 (1968).
77. V. H. J. Engell and P. Vygen, "Ionen-und Elektroneuleitung in CaO-FeO-Fe₂O₃-SiO₂ Schmelzen", Ber der Bunsenges ell-Schaft, 72 (1), 5-12 (1968).

78. J. Gotz and C. R. Masson, "Trimethylsilyl Derivatives for the Study of Silicate Structures, Part I. A Direct Method of Trimethylsilylation", J. of Chem. Soc. A, 2683-2686 (1970).
79. J. Gotz and C. R. Masson, "Trimethylsilyl Derivatives for the Study of Silicate Structures, Part II. Orthosilicate, Pyrosilicate, and Ring Structures", J. of Chem. Soc. A, 686-688 (1971).
80. F. F. H. Wu, J. Gotz, W. D. Jamieson and C. R. Masson, "Determination of Silicate Anions by Gas Chromatographic Separation and Mass Spectrometric Identification of Their Trimethylsilyl Derivatives", J. of Chrom. 48, 515-520 (1970).
81. H. Flood, T. Forland and B. Roald, "The Acidic and Basic Properties of Oxides", Acta. Chem. Scand. 1, (9), 790-798 (1947).
82. F. D. Richardson, "The Vitreous State", The Glass Delagacy of University of Sheffield, 63-84 (1955).
83. G. W. Toop and C. S. Samis, "Activities of Ions in Silicate Melts", Trans. A.I.M.E., 224 (10), 878-887 (1962).
84. G. W. Toop and C. S. Samis, "Some New Ionic Concepts of Silicate Slags", Can. Met. Q, 1 (1), 129-152 (1962).
85. C. R. Masson, "An Approach to the Problem of Ionic Distribution in Liquid Silicates", Proc. Royal Soc. A, 287, 201-221 (1961).
86. C. R. Masson, "Ionic Equilibria in Liquid Silicates", J. Am. Ceram. Soc., 51 (3), 134-149 (1968).
87. C. R. Masson, I. B. Smith and S. G. Whiteway, "Activities and Ionic Distributions in Liquid Silicates - Application of Polymer Theory", Can. J. of Chem., 48 (9), 1456-1464 (1970).
88. R. Schuhmann, Jr. and P. J. Ensio, "Thermodynamics of Iron-Silicate Slags: Slags Saturated with Gamma Iron", Trans. A.I.M.E., 191 (7), 401-411 (1951).
89. E. J. Michal and R. Schuhmann, Jr., "Thermodynamics of Iron-Silicate Slags: Slags Saturated with Solid Silica", Trans. A.I.M.E., 192 (7), 723-728 (1952).

90. E. T. Turkdogan, "Activities of Oxides in SiO_2 -FeO- Fe_2O_3 Melts", *Trans. A.I.M.E.*, 224 (4), 294-298 (1962).
91. J. Lumsden, "The Thermodynamics of Liquid Iron Silicates", *Met. Soc. Conf. 7*, 165-205 (1961).
92. L. S. Darken and R. W. Gurry, "The System Iron-Oxygen II. Equilibrium and Thermodynamics of Liquid Oxide and Other Phases", *J. Am. Chem. Soc.* 68 (5), 798-816 (1946).
93. E. T. Turkdogan and P. M. Bills, "Some General Considerations on the State of Oxidation of Iron in Molten Silicates, Phosphates and Silicophosphates", *Met. Soc. Conf. 7*, 207-227 (1961).
94. E. T. Turkdogan and P. M. Bills, "A Thermodynamic Study of FeO - Fe_2O_3 - SiO_2 , FeO - Fe_2O_3 - P_2O_5 and FeO - Fe_2O_3 - SiO_2 - P_2O_5 Molten Systems", *J.I.S.I.*, 186 (7), 329-339 (1957).
95. E. Froese, "The Oxidation of Alanandine and Iron Cordierite", *Can. Miner* 11 (5), 991-1002, (1973).
96. C. B. Alcock, private communication.
97. T. O. Mason, private communication.
98. T. B. Reed, "Free Energy of Formation of Binary Compounds", *M.I.T. Press*, (1971).
99. C. K. Kim and A. McLean, "Hercynite Formation in Molten Iron Alloys", in Metal-Slag-Gas Reactions and Processes, Ed. by Z. A. Foroulis and W. W. Smeltzer, *The Electrochem. Soc.*, pp. 284-295, (1975).
100. H. Larson and J. Chipman, "Oxygen Activity in Iron Oxide Slags", *Trans. A.I.M.E.* 193 (9), 1089-1096 (1953).
101. W. D. Johnston, "Oxidation-Reduction Equilibria in Iron-Containing Glass", *J. Am. Ceram. Soc.* 47 (4), 198-201 (1964).
102. T. Baak and E. J. Hornyak, Jr., "The Iron-Oxygen Equilibrium in Glass: Effect of Platinum on $\text{Fe}^{2+}/\text{Fe}^{3+}$ Equilibrium", *J. Am. Ceram. Soc.* 44 (11), 541-544 (1961).
103. J. White, "Equilibrium at High Temperatures in Systems Containing Iron Oxides", *J. Iron Steel Inst., Carnegie Scholarship Members*, 27, 1-75 (1938).

104. Y. C. Chiu and R. M. Fuoss, "Conductance of the Alkali Halides. XII. Sodium and Potassium Chlorides in Water at 25 °", J. Phys. Chem. 72 (12), 4123-4129 (1968).
105. C. E. Meyers, "Determination of the Spinel Phase Field in Fe-Al-O at 1370°C", unpublished work.
106. C. F. Yen, "Characterization of Point Defects in Annealed Single Crystal Aluminum Oxide by Color Center Study", S.M. Thesis, Department of Metallurgy and Materials Science, February, 1974.
107. J. Henderson, R. G. Hudson, R. G. Ward and G. Deye, "Density of Liquid Iron Silicate", Trans. A.I.M.E. 221, (8), 807-711 (1961).
108. K. Mori and K. Suzuki, "Density of Iron Oxide Melt in Equilibrium with CO₂-CO Gas Mixtures", Trans, I.S.I.J. 8, 382-385 (1968).
109. J. J. Rasmussen and R. P. Nelson, "Surface Tension and Density of Molten Alumina", U. S. Clearinghouse, Fed. Sci. Tech. Inform. A.D. 1970, No. 711964, p.19.
110. L. W. Tilton, "Noncrystal Ionic Model for Silica Glass", J. Research Nat'l. Bur. Standards, 59, 139-154 (1957).
111. E. F. Riebling, "Structure of Magnesium Aluminosilicate Liquids at 1700°C", Can. J. Chem., 42(12), 2811-2821, (1964).
112. E. F. Riebling, "Structure of Sodium Aluminosilicate Melts Containing at Least 50 mole% SiO₂ at 1500°C", J. Chem. Phys. 44(8), 2857-2865, (1966).

Biographical Note.

The author was born in Hong Kong on August 21, 1950. After graduating from St. Louis School, Hong Kong in 1968, he attended McGill University in Montreal, Canada.

He transferred to Massachusetts Institute of Technology in the fall of 1969 and subsequently received a S.B. in Metallurgy and Materials Science and a S.M. in Ceramics in 1974.

The author is currently a member of the American Ceramic Society. Following are the presentations and publications by the author:

1. C. F. Yen and R. L. Coble, "Point Defects in Single Crystal Aluminum Oxide", presented at the Annual Meeting of the American Ceramic Society in Washington, D.C. in May, 1975.
2. C. F. Yen and R. L. Coble, "On the Spheroidization of Tubular Voids in Al_2O_3 at High Temperatures", J. Amer. Ceram. Soc. 55 (10), 507-508 (1972).
3. J. I. Goldstein, A. J. Axon and F. Yen, "Metallic Particles in the Apollo 14 Lunar Soil", Proc. of the Third Lunar Science Conference, Vol. I, 1037, M.I.T. Press, (1972).
4. R. L. Coble, S. C. Samanta and F. Yen, "Kinetics for the Intermediate Stage Sintering of Silver", Proc. of the Second Round Table Meeting of the International Team for the Study of Sintering.